Summer 2011

A Variable Acceleration Calibration System

Thomas H. Johnson
Old Dominion University

A VARIABLE ACCELERATION CALIBRATION SYSTEM

by

Thomas H. Johnson
B.S. Aerospace Engineering, August 2006, Boston University
M.S. Aerospace Engineering, May 2008, Old Dominion University

A Dissertation Submitted to the Faculty of
Old Dominion University in Partial Fulfillment of the
Requirements for the Degree of

DOCTOR OF PHILOSOPHY

AEROSPACE ENGINEERING

OLD DOMINION UNIVERSITY
August 2011

Approved by:

Drew Landman (Director)

Colin P. Britcher (Member)

Peter A. Parker (Member)

Robert L. Ash (Member)

ABSTRACT

A VARIABLE ACCELERATION CALIBRATION SYSTEM

Thomas H. Johnson
Old Dominion University, 2011
Director: Dr. Drew Landman

A variable acceleration calibration system that applies loads using gravitational and centripetal acceleration serves as an alternative, efficient and cost effective method for calibrating internal wind tunnel force balances. Two proof-of-concept variable acceleration calibration systems are designed, fabricated and tested. The NASA UT-36 force balance served as the test balance for the calibration experiments. The variable acceleration calibration systems are shown to be capable of performing three component calibration experiments with an approximate applied load error on the order of 1% of the full scale calibration loads. Sources of error are indentified using experimental design methods and a propagation of uncertainty analysis. Three types of uncertainty are indentified for the systems and are attributed to prediction error, calibration error and pure error. Angular velocity uncertainty is shown to be the largest indentified source of prediction error. The calibration uncertainties using a production variable acceleration based system are shown to be potentially equivalent to current methods. The production quality system can be realized using lighter materials and a more precise instrumentation. Further research is needed to account for balance deflection, forcing effects due to vibration, and large tare loads. A gyroscope measurement technique is shown to be capable of resolving the balance deflection angle calculation. Long term research

objectives include a demonstration of a six degree of freedom calibration, and a large capacity balance calibration.

ACKNOWLEDGMENTS

I would like to thank the NASA Graduate Student Research Program and the NASA co-op program for funding this research. I would also like to thank my family for their continued support.

TABLE OF CONTENTS

LIST OF TABLES

LIST OF FIGURES

1 INTRODUCTION

1.1 Problem Statements and Objectives

A new system is desired that can efficiently and accurately calibrate large-scale multi-component force balances. Large balances present the obstacle that a large force is required to span the entire load range of the balance, necessary for proper calibration. A new calibration system is desired that uses an alternative loading method, thereby circumventing the time and expense of large balance calibrations.

1.2 Approach

The plan is to design and test a new method for calibrating internal wind tunnel force balances. This new approach will employ a statistically rigorous experimental design that supports a high order multivariate regression model with as few runs as possible. The mechanical system will be designed specifically to implement this optimal run schedule, setting it apart from most existing methods. The unique aspect of the proposed system is that instead of applying calibration loads using mechanical actuators or dead weights, as is currently performed, loads will be applied using centrifugal force. There are many advantages to this method. Compared to dead weight loading schemes, less weight will be moved by the technician during the calibration experiment. This will greatly increase efficiency, especially for balances requiring high loads. The second advantage is that the mechanical system will contain fewer degrees of freedom than automated calibration machines, thus less error is propagated into the applied load. The third advantage is that it may require a smaller operating footprint compared to other systems; thus, it could be used for in-tunnel calibrations -- a capability that NASA wind tunnels currently do not possess. Two mechanical systems were fabricated to

demonstrate the feasibility of the proposed method. A spinning rate table, a six degree of freedom force balance and the supporting electronic equipment were procured from NASA LaRC. The objective is to demonstrate the feasibility of the method. More specifically, the physical system must prove to have an applied load error within the tolerances specified by the theoretical design for each run in the calibration experiment. The tolerances will be based on the fidelity of equipment available and, thus, the resources available for this project. A small load proof of concept experiment could serve to validate this method for large capacity use.

2 BALANCE SYSTEM HARDWARE

2.1 Multi-Component Internal Force Transducers

The fundamental instrument used to directly measure aerodynamic loads on a wind tunnel model is known as an internal force transducer or, more simply, a force balance. The underlying purpose of wind tunnel testing is to measure the performance characteristics of an aircraft or spacecraft in an environment that closely simulates true flight conditions. To adequately determine these model performance characteristics, it is crucial that a measurement device be used during the wind tunnel test that is capable of accurately and precisely measuring aerodynamic loads imparted on the test model. A multi-component force balance typically contains six degrees of freedom, capable of measuring normal force (NF), side force (SF), axial force (AF), pitching moment (PM), yawing moment (YM), and rolling moment (RM) by monitoring structural deformation of the balance with strain gages arranged in Wheatstone bridges. The balance is said to be "internal" because the instrument is mounted within the wind tunnel model [1]. The specific balance used in the research is the NASA UT-36 internal wind tunnel force balance, as shown in figure 1. The metric (cylindrical) end of the balance connects to the aircraft model, while the non-metric (tapered) end is attached to the support structure in the wind tunnel, commonly known as the sting.

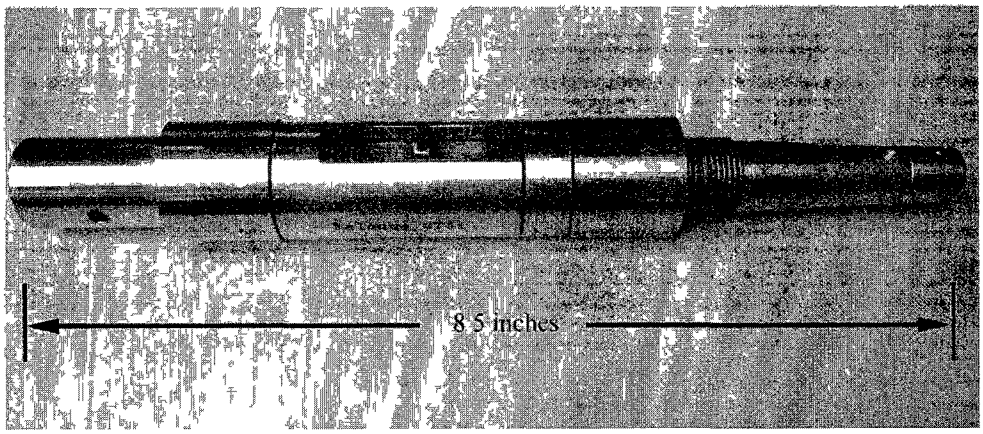

Figure 1. UT-36 Balance

There are typically three measuring sections within an internal force balance: two cage sections and an axial section. The cage sections often measure five degrees of freedom comprised of two forces (normal and side) and three moments (pitch, yaw, roll) The axial section measures one force, axial force

A traditional internal balance uses a Wheatstone bridge configuration of strain gages to monitor the forces and moments. Usually, six primary bridges are used to measure six components of force. Redundant bridging is often employed to prevent bridge failures. In such a case, twelve bridges are used for a single balance, where each force component has a primary and secondary bridge. A balance design usually optimizes the gage placements such that the strain output of a given bridge is maximized for the component of interest and minimized for the other extraneous force components [3]. This is necessary to maximize the primary sensitivities and to minimize interaction coefficients in the calibration model.

Now that the force balance has been introduced, the systems used to calibrate these instruments will be discussed The three most common calibration systems of today

include manual dead weight calibration stands, multi-component calibration machines and the single vector system (SVS). To begin, background on these three systems is provided in context with their operational complexity and associated cost.

2.2 Manual Stand Systems

Manual dead weight calibration stands have been considered the standard method for calibration at NASA Langley Research Center (LaRC) since the 1940s. An example of a manual test stand is shown in figure 2. Properly used, this type of system produces accurate results, but it suffers from operational complexity. Gravity-based loads are applied via a complex system of levers, bell-cranks, cables, knife-edges, moment arms and optical alignment devices. Multiple orthogonal cables are used to apply individual components of loads. After each load is applied, the balance is re-leveled prior to taking data to assure that the applied loads are orthogonal to the balance coordinate system. At NASA LaRC this system is typically used to apply 729 different loading configurations to calculate the calibration mathematical coefficients [4]. Calibrations complete considerably slower on manual stand systems compared to automated calibration machines and the single vector system. The cost of manual test stands is comparable to the single vector system but is less than calibration machines.

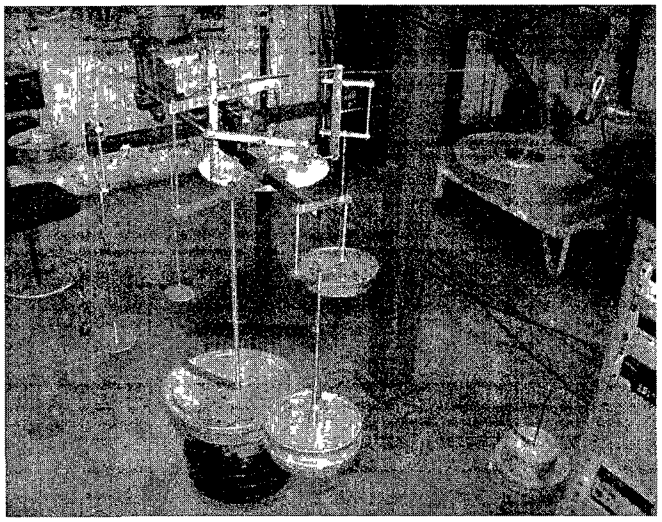

Figure 2. Manual Stand System

2.3 Automated Machine Calibration Systems

Calibration machines are similar to manual test stands in that they both use multiple orthogonal force vectors to apply loads to the transducer [5]. The main difference between these two systems is that manual test stands apply loads via hanging dead weights, while calibration machines apply loads via mechanical actuators [6]. A sequence of mechanically actuated loads can be programmed for the entire calibration, hence making the system automated [7]. Calibration machines can be considered the fastest, most complex, but also the most expensive type of calibration system. Figure 3 is an example of a calibration machine used at the European Transonic Wind Tunnel [8].

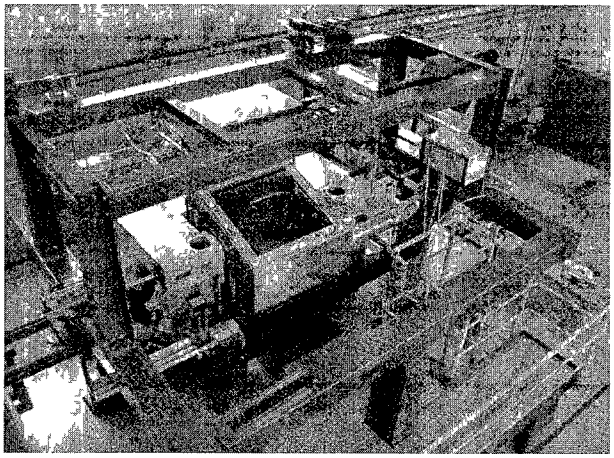

Figure 3. Calibration Machine

2.4 Single Vector System

The current state of the art calibration system used at NASA LaRC is the Single Vector System (SVS) [4]. The SVS is unique because it uses a single applied force vector, created solely by gravity. By pitching and rolling the transducer, and by changing the location of the applied gravitational force relative to the transducer moment center, combinations of all six force components can be achieved. This loading technique, in conjunction with a statistically rigorous loading sequence, makes the SVS the preferred method for calibration at LaRC since 2001 [4]. The statistical approach employed by the SVS is based upon three pillars: replication of calibration runs, blocking of sets of calibration runs and randomizing the order of calibration runs. Replication and randomization allows for a test of internal systemic error and provides a check for set point errors [9]. Blocking helps defend against nuisance errors that are uncontrollable during the experiment [10]. This statistical approach compliments the SVS hardware by allowing for a minimal number of configurations during the calibration. The single

vector system, as shown in figure 4, uses less hardware compared to the other calibration systems. The pitch and roll actuators connected to the non-metric end of the balance are used to rigidly orient the balance. The force positioning system contains a rolling bearing, with an attached pitch arm, connected to a free-hanging weight pan. The load application point is located at the intersection of the pitch arm rotational axis and the roller bearing rotational axis. This load application point can be translated along the surface of the balance fixture, resulting in a highly versatile single vector loading method. Orientation of the balance and applied load vector are monitored using two separate tri-axis accelerometer packages. This passive monitoring strategy allows balance deflection correction to be made in the post-processing of the data; thus, re-leveling is not required. The SVS can be considered the mechanically simplest of the three systems. Since there is only one applied force vector and re-leveling is not required, the SVS is faster than manual test stands but slower than automated machines in terms of load application time. In terms of total calibration time, however, the SVS is comparable to automated machines, since it employs a statistically efficient experiment design. Now that the three major classes of calibration systems have been introduced and compared, problems associated with dead weights will be discussed.

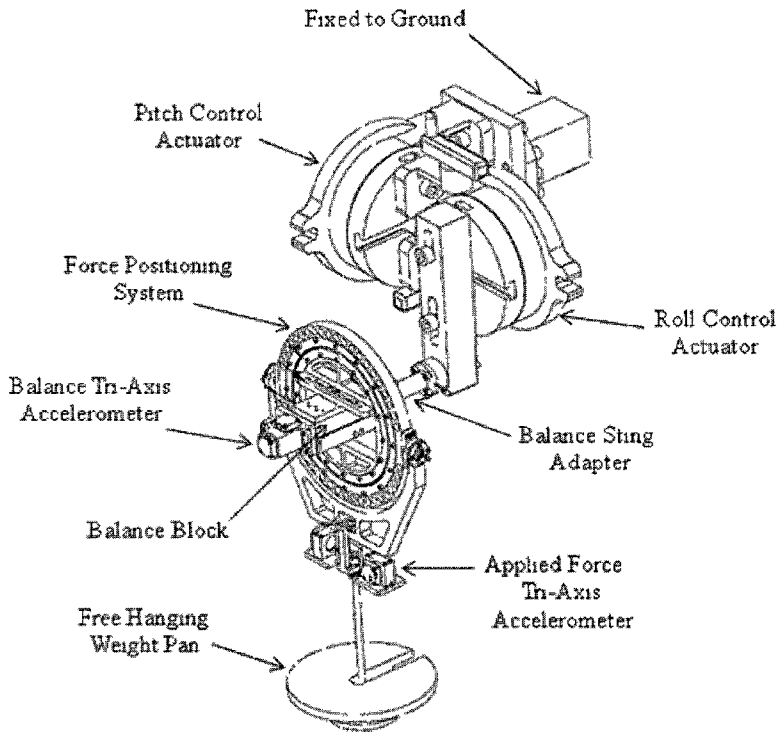

Figure 4. Single Vector System

2.5 Comparison of Techniques

In any industry, there is always a cost associated with moving weight. A large problem with the SVS and manual test stands is that they use dead weight to apply loads on the transducer. Between calibration runs, the weight is manually removed or added by the operator. This process can become slow and tedious when the weight is changed many times throughout the calibration experiment. For large scale transducers, upwards of 2,500 lbs can be added and then later removed, as shown in figure 5. Such a large amount of weight could take approximately twenty minutes to setup before data is taken.

Figure 5. Manual Stand Loading Procedure

The current SVS has a structural limitation of 3,000 lbs. This is due to the mechanical design of the system. The SVS concept can be extended to any load range; however, loading with dead weight becomes less efficient as the load requirement increases.

Minimizing the number of independent variables of a calibration system effectively reduces the error associated with applying a multi-component load. Correspondingly, a single applied force vector has less inherent error than multiple applied force vectors. Furthermore, a single applied force vector can produce a multi-component load using three possible methods: (1) the applied load vector is held stationary while the balance is repositioned, (2) the balance is held stationary while the applied load vector is repositioned, or (3) both the balance and load are free to reposition. Similar to before, applied load error is reduced by minimizing the number of independent variables; therefore, methods (1) and (2) are equally preferred over method (3).

Method (1) is utilized by the single vector system, which orients a balance and uses free-hanging weights to apply gravity-based loads. This application benefits from the fact that gravity is a body-force that acts in a constant direction. Using method (1)

with a mechanically actuated applied load is not strictly possible because it is not a body-force; therefore, the direction of applied force is a function of the balance position and orientation. Method (2) is possible using an automated calibration machine; however, the complexity of the mechanism used to position the actuator and the structural integrity required for that mechanism to apply a large scale load would greatly increase the cost of the system. For this reason, method (3) is commonly used for automated calibration machines.

As demonstrated by the single vector system, method (1) is made possible via the application of a body-force. Similar to gravity-based loads, centrifugal force is considered a pseudo-body force that upholds method (1) as long as the rotation vector is held constant. An advantage of the body-force load application method is that it requires fewer support structures than conventional load application methods. For instance, a manual stand calibration system using a cable and pulley to apply gravity-based loads requires two support structures: one to support the sting-end of the balance and one to support the pulley. Likewise, a calibration machine requires a support structure for the balance and for each mechanical actuator. For large-scale balance calibration systems, support structures have a significant impact on the overall cost of the system.

A final problem is that calibration systems require a large footprint to operate, making them highly immobile. The inventory of weights alone for the manual stand or SVS is enough to fill a small facility. While a calibration machine does not require weights, it does have a bulky external frame. For these reasons, it may not be feasible to create a mobile or in-situ platform using any of these existing systems.

3 CALIBRATION MODELING AND EXPERIMENTAL DESIGN

3.1 Fundamental Concepts

The most critical portion of the balance design process is the characterization of the balance, which is necessary to develop a mathematical model for the performance of the balance. In return, this mathematical model can be used to estimate the aerodynamic loads imparted on the model during the wind tunnel test. As a general procedure, when characterizing a force balance, a set of pre-determined independent variables (applied calibration loads) are applied to the balance, and the resulting dependent variables (electrical output response of each measurement bridge) are recorded. A forward model of the electrical output as a function of the applied loads is constructed for each force component. Then in practice, back-calculated loads are computed from the bridge outputs using an iterative inverse prediction method. The load schedule (which defines the load combinations and the order in which they are to be performed) and the regression model used to characterize a balance are formulated in a statistically rigorous manner. The fundamentals of this approach are reviewed in the following section.

The designed experiment is a critical component of the calibration experiment. Two general experimental design methods for calibration involve the One Factor At a Time approach (OFAT), or the Design Of Experiments approach (DOE) [9]. A general distinction between these two methods is that the OFAT method loads one balance component during each run, while the DOE method loads multiple components simultaneously.

DOE is a process for planning an experiment so that appropriate data can be collected and analyzed by statistical methods, resulting in valid and objective

conclusions. Replication, randomization, and blocking are three major principles that make DOE effective. Randomization requires that both the experimental factor choices and the order of the runs are randomly determined, since the statistical methods employed by DOE require that the regression model residuals are normally and independently distributed. Additionally, randomization assists in averaging out the effects of extraneous factors that may be present. Replication is a fundamental concept used in DOE, and it should not be confused with run repetition. Replication requires resetting the experimental factors for each trial. Using run repetition, the experimental factors are set once, and data is taken multiple times. Related to balance calibration, the difference between performing two repeated runs, and two replicates is described. Using run repetition, first, the balance would be loaded. Next, data would be taken. After an amount of time, another round of data would be taken. Using replication, first, the balance would be loaded and then data would be taken. Next, the balance would be unloaded and then reloaded using the same loading conditions as before. Finally, data is taken again. Both replicates and repeated runs can be used to measure the noise of the system process; however, only replicates provide an estimate of the experimenter's ability to set the experimental factors. In other words, the repeated run noise estimate is smaller than replication noise estimate, and this could lead to greater risk in estimating the significance of effects in the calibration model.

Replication of design points allows the researcher to determine an internal, or model independent, estimate of system noise and uncertainty. This leads to the lack of fit (LOF) test, which determines if variation in the model predictions significantly differs from the variation in the replicated points. Blocking is a technique used to improve the

precision with which comparisons among the factors of interests are made by reducing the variability transmitted through nuisance factors -- that is, factors that may influence the experimental response but that are of no direct interest [11].

One of the greatest benefits in using DOE methods versus the traditional OFAT methods is the ability to include interaction terms in the analysis. The OFAT method only allows for one variable to be changed at a time; therefore, it typically estimates main effects only. The DOE method allows, and partially requires, the change of more than one factor simultaneously, thus allowing for the estimation of interactions between variables. To illustrate, in figure 6 there are two factors (FX, FY) with two level settings for each factor (high, low) with a response. In the OFAT case each factor is set individually. In the DOE case, the FY factor is set high while the FX factor is also high. This interactive setting allows for estimation of the effect between simultaneously engaged factors [9].

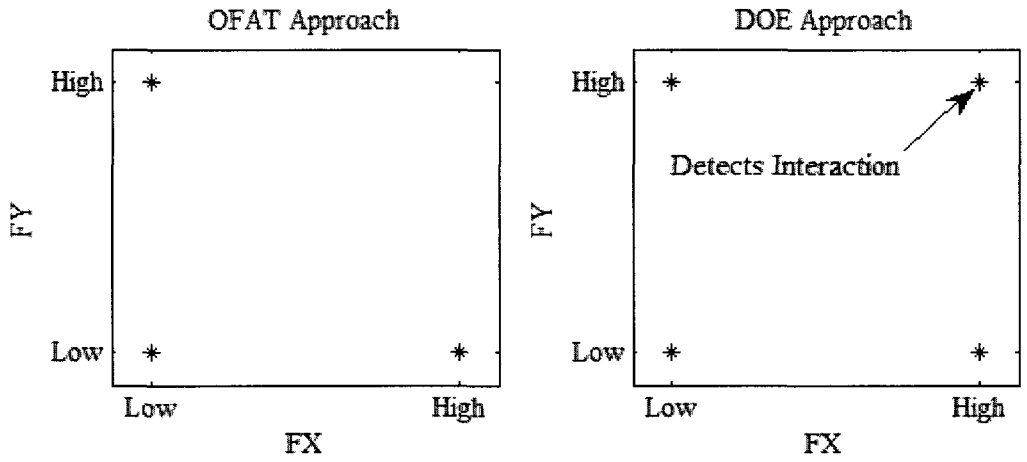

Figure 6. OFAT vs. DOE, Factor Settings

The OFAT approach holds one factor "constant" while varying other factors. The DOE approach varies all factors simultaneously. By omitting the point in the design matrix where FX and FY are high, the interaction cannot be accurately estimated. It is possible that the FX response may vary depending on the value of FY. DOE can efficiently estimate and predict the interaction effects that an applied FX and FY have on output. The relative magnitudes of the model coefficients in the model give direct feedback as to the importance of the interaction effects to the overall responses [9].

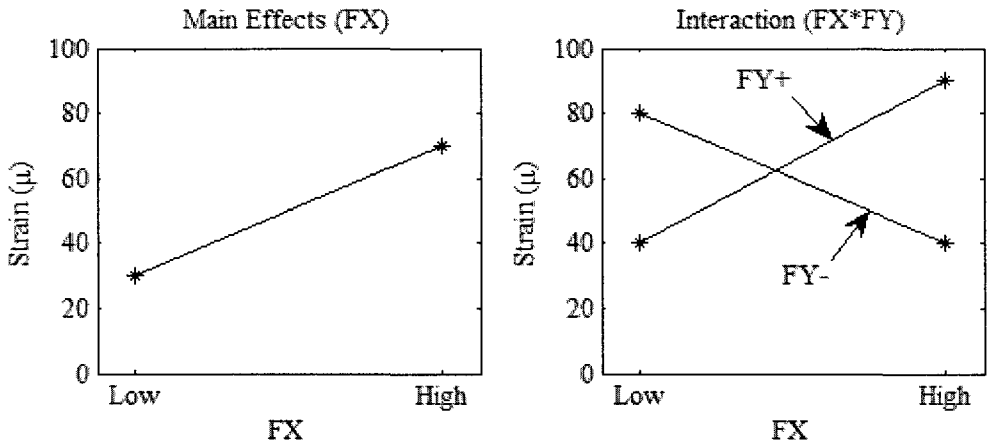

Figure 7. OFAT vs. DOE, Responses

Efficient prediction of an interaction effect is an advantage of DOE that is made possible by thoughtful experiment design planning. This planning must also consider the regression model that is to be fit. In the previous example (figure 6), a fourth design point was required to form a factorial experiment necessary to estimate the interaction effect. Along with replication, randomization and blocking, the factorial experiment is an important aspect of the DOE approach. The previous example showed a simple 2^2 factorial experiment; however, factorials can be scaled to accommodate more than two

factors, allowing for estimation of interaction effects between multiple factors. An orthogonal subset of a multi-factor factorial, referred to as a fractionated factorial, is an efficient experimental design, especially when the number of factors in the experiment increases [13]. Such an experiment is used for SVS calibrations, which is discussed in a later section.

The factorial experiment can independently estimate linear and two factor interactions effects. Including quadratic effects in the calibration model requires augmenting the factorial experiment with additional points. These points are selected such that the main effects and quadratic terms can be estimated nearly independently from each other. For each parameter type added to the model (cubic, bi-cubic, three-factor-interaction), a special alteration to the designed experiment is required. Unfortunately, not all parameter types can coexist in the same model, regardless of the experimental design. Such a case is highlighted in reference [21], where certain model parameters used to estimate the output of non-monolithic balances are shown to be collinear. The metrics used to determine the degree of collinearity, in a given regression model, are presented in the following section.

3.2 Calibration Design Cases

In this section two calibration methods that use DOE are presented. The first method is currently used by the Single Vector System at NASA LaRC, while the second is a method used to calibrate large scale balances.

The second-order SVS calibration model is shown in equation (1). In this equation, i varies from one to six; thus, there are six responses, one for each balance component. The responses, R_i, are electrical output while the six independent factors, F_j or F_k are the

applied forces. a_i is the intercept for the ith model, $b1_{i,j}$ is the main effect coefficient for the jth factor of the ith model, $c1_{i,j}$ is the quadratic coefficient, and $c3_{i,j,k}$ is the two-factor-interaction coefficient between the jth and kth factor for the ith model. In this equation, n is the number of factors, 6, while F_j or F_k is the factor setting (lbs). For each model there is one intercept, six main effects, 6 pure quadratics, and 15 two-factor-interactions, for a total of 27 parameters (not including the intercept). Thus, a 27 x 6 matrix of forward calibration models is required to model the complete balance behavior [2].

$$R_i = a_i + \sum_{j=1}^{n} b1_{i,j} F_j + \sum_{j=1}^{n} c1_{i,j} F_j^2 + \sum_{j=1}^{n} \sum_{k=j+1}^{n} c3_{i,j,k} F_j F_k \qquad (1)$$

A typical SVS experimental design used to accommodate this model is shown in appendix B. The SVS design shown has five center points per block, allowing for eight total degrees of freedom for estimation of pure error. The first block consists of 37 runs, while the second block contains 27 for a total of 64 runs. This design, which is used by the single vector system, is a variation of a 2^{6-1} fractionated-factorial, central composite design (CCD). This design differs from traditional CCDs because the axial (star) points are subjected to the physical constraint of the single vector system. The physical constraint, shown in equation (2), limits certain load combinations. The derivation of this constraint is given in reference [4].

$$-(RM)(AF) + (PM)(SF) - (YM)(NF) = 0 \qquad (2)$$

The constraint exists because a singly applied force vector has physical limitations. Pure moments cannot be achieved; therefore, combinations of two factor loads are used as a substitute where pure moments would ideally be run. This design alteration gives rise to multi-collinearity between three two-factor interactions in a full calibration model. As a result, among the three collinear two-factor-interactions only two can be estimated simultaneously. To circumvent this problem, an iterative model reduction scheme is employed that estimates pair-wise combinations of the three two-factor-interactions and determines which of the three two-factor interactions is least significant, and discards that term. From there, standard model reduction methods are used to reduce the 26 term models.

The calibration design and modeling strategy used by the single vector system is effective for smaller size balances (less than 3000 lbs); however, calibration of large balances presents several additional problems not found with small balance calibrations, which is a problem inherent to manual stand systems too. Using the factorial design method, weights are incremented over the full scale range for six different levels. Achieving exact load conditions for runs that involve up to six active factors might not be possible due to physical constraints. Loading challenges could lead to slight departures from the ideal (exact) loading conditions, which could cause departures of design orthogonally. A previous large-scale calibration of an external balance, performed in reference [12], showed that slight departures from orthogonality are accommodated by factorial designs. In this example, the power for detecting significant effects with two standard deviations varied from 87-99% for the non-ideal loading case versus 99% for

the ideal case (assuming a 5% α level). For the non-ideal case, all main effects were above 96% and all two factor interactions were above 94%. Reference [12] also investigated the non-ideal loading effect on variance inflation factors. Typically with fractional factorial designs, the columns are pair wise orthogonal, resulting in linearly independent estimates of the regression coefficients and ideal VIF's of 1.0 for all terms. In this example, physical constraints required that the standard design be modified, so checking VIF values was important. It was shown that the deviation from the ideal orthogonal design (VIF = 1) is slight with a maximum recorded VIF of 1.18.

Design of experiments proved to be beneficial for the single vector system by substantially reducing calibration time and by demonstrating that factor constraints are tolerated within certain experiments. The next example shows how an experiment can be designed to aid in the calibration of large scale balance using a manual test stand.

The large balance calibration problem, using a manual test stand, is eased by developing a design matrix that requires partial loading per run. This allows for a quicker load application time. The Box-Behnken design (BBD), introduced by Box and Behnken (1960) offers several notable advantages as an alternative to the factorial design presented above [13]. The BBD requires a smaller subset of factors to be set ("active") for each run. For large load manual stand calibration testing, this reduced active factor feature is quite attractive.

Table 1shows a modified BBD developed by Landman and Simpson that contains 5 center points, 65 total runs and three levels for each factor –1, 0 and +1. The two-active-factor BBD alleviates the difficulty of implementation since only two of the six factor components are loaded simultaneously. As a means of estimating pure system

error, five center points are used in the design [10]. Table 1shows the test matrix derived from the BBD with two active factors.

Table 1. Modified Box-Behnken Design

Normal	Axial	Pitch	Roll	Yaw	Side	Runs
±1	±1	0	0	0	0	4
±1	0	±1	0	0	0	4
±1	0	0	±1	0	0	4
±1	0	0	0	±1	0	4
±1	0	0	0	0	±1	4
0	±1	±1	0	0	0	4
0	±1	0	±1	0	0	4
0	±1	0	0	±1	0	4
0	±1	0	0	0	±1	4
0	0	±1	±1	0	0	4
0	0	±1	0	±1	0	4
0	0	±1	0	0	±1	4
0	0	0	±1	±1	0	4
0	0	0	±1	0	±1	4
0	0	0	0	±1	±1	4
0	0	0	0	0	0	5

The disadvantage of this method, however, is that it requires more runs than if a central composite design were employed.

4 A VARIABLE ACCELERATION CALIBRATION SYSTEM

4.1 Introduction

The Variable Acceleration Calibration System (VACS) differs from existing systems because it uses both centripetal and gravitational acceleration to apply loads onto a balance. The fundamental concept uses a mass that is rigidly attached to the balance and is exposed to a centripetal and gravitational acceleration. The resulting force imparted by the attached mass is shown in equation (3).

$$\boldsymbol{F} = m[\boldsymbol{\omega} \times (\boldsymbol{\omega} \times \boldsymbol{r}) + \boldsymbol{g}] \tag{3}$$

A large force can be applied using a relatively small amount of weight and a large rotational velocity. As a result, less weight is moved during the calibration process leading to a decrease in calibration time compared to traditional dead weight loading methods.

Two proof-of-concept systems have been constructed to demonstrate the feasibility of the variable acceleration concept. The hardware of both is designed around a specific set of calibration runs that loads multiple components simultaneously. The prototypes differ in the way the balance is positioned in the rotational field, and where the mass is attached to the balance. The first prototype, referred to as the "centered system," has the balance centered on the rotating table with the balance axial force axis parallel to the axis of rotation. The second prototype, referred to as the "off-center system," differs from the centered system since it is positioned off the center of the table with its axial force axis at an angle relative to the rotation axis.

A simple two dimensional representation of both systems is shown in figure 8, where equations (4) through (6) determine the component loads on the balance. In figure 8, point O is the center of the rotating table, which rotates with angular velocity, ω. The axial force axis of the balance, also referred to as the "balance axis," is defined by line segment AC. Point A is where the balance attaches to the table, point B is the moment center of the balance, θ is the pitch angle of the balance, and α is the misalignment angle between the table rotation axis and the gravity vector. T_x is the translational offset between the balance attachment point and the center of the table. R is the arm length between the balance axial force axis and the center of gravity of the attached weight m, while ϕ is the pitch angle of the arm with respect to line that is perpendicular to the balance axis. For the centered system, T_x and θ are zero, while for the off-center system, R is zero. Equations (4) through (6) assume constant rotational velocity and represent the average load during one revolution. Further details about the derivation of equations (4) through (6) can be found in appendix C.

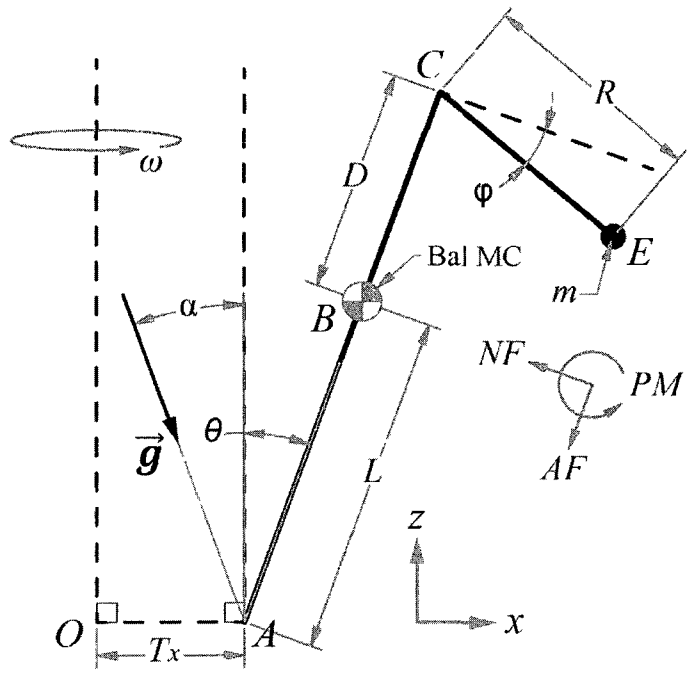

Figure 8. Geometry of Calibration Systems

$$NF = -m\omega^2[T_x + sin(\theta)(L + D) + cos(\phi)cos(\theta)R - sin(\phi)sin(\theta)R]cos(\theta) - mgcos(\alpha)sin(\theta) \quad (4)$$

$$AF = -m\omega^2[T_x + sin(\theta)(L + D) + cos(\phi)cos(\theta)R - sin(\phi)sin(\theta)R]sin(\theta) + mgcos(\alpha)cos(\theta) \quad (5)$$

$$PM = [cos(\phi)D - sin(\phi)R]NF + [sin(\phi)D + cos(\phi)R]AF \quad (6)$$

4.2 Calibration Models and Experimental Designs

Two-level factorial designs are foundational to designed experiments since they provide an efficient experimental strategy to explore first order effects and two-factor interactions. In these designs, the factors of interest are changed between predetermined high and low levels, often denoted in coded units as the +1 and -1 levels [10]. The high

and low levels of the ideal calibration experiment are chosen to be safely within the maximum balance design loads of the UT-36 balance, as shown in table 2.

Table 2. UT-36 Design Loads and Calibration Loads

	NF (lbs)	AF (lbs)	PM (in-lbs)
Balance Design Loads	100	60	800
Calibration Loads	30	20	120

The calibration experiments for the centered and off-center system are shown in table 3 and table 4 respectively. The calibration experiments are factorial experiments in three factors. Both designs consist of eight factorial points and one center points. The design is fully replicated, which provides a total of 18 runs. Point replication is employed to provide an internal estimate of experimental error. Full replication also helps increase power, which is defined as the probability that the statistical test will reject the null hypothesis when the null hypothesis is false. Additionally, by replicating each point in the experiment, dispersion effects caused by different system configurations can be investigated. Hypothetically speaking, suppose the following effects are calculated for factor settings X, Y and Z in an experiment:

$$\begin{aligned} \beta_X &= +3.5 \\ \beta_Y &= +5.7 \\ \beta_Z &= -3.0 \quad . \end{aligned} \tag{7}$$

These effects reflect the change in the mean response as the factor settings change. As factors X and Y increase, the mean response increases. As factor Z increases, the mean response decreases. These are known as location effects. Suppose an increase in X results in an increase in the variance of the response. Now X has a location and dispersion effect which results in a mean-variance tradeoff which must be considered when changing X [10].

In natural units, the axial force calibration loads are not centered about zero because of the orientation constraint of the centered system. Due to this constraint, the balance cannot be pitched; therefore, gravity always acts in the positive axial force direction. This hindrance is acceptable for some wind tunnel balance applications since axial force loads of some balances can be dominated by a unidirectional drag force. In contrast to the centered system design, the off-center system contains axial force loads centered about zero load. For the off-center system, negative loads are made possible by applying centrifugal force while the balance is pitched. In coded units, the ideal calibration experiments of both systems are identical.

The experiments are presented in standard order, meaning they are sorted by ascending standard run number. The standard order, which is non-random, aids in visualizing the experiment from a design perspective. The run number, which is random, dictates the sequence of the actual experiment. Randomization of run order is used to decouple systematic error effects from independent variable effects. Randomization requires that both the experimental factor choices and the order of the runs are randomly determined [25]. By randomizing the set point order of the independent variable levels,

the systematic error effects are converted to additional components of random error, which can be analyzed using replication [26].

Table 3. Ideal Centered System Calibration Experiment

Centered System							
		Natural Units			Coded Units		
Std Run#	Run#	NF (lbs)	AF (lbs)	PM (in-lbs)	NF	AF	PM
1	4	-30	6	-120	-1	-1	-1
2	18	-30	6	-120	-1	-1	-1
3	9	30	6	-120	1	-1	-1
4	15	30	6	-120	1	-1	-1
5	2	-30	20	-120	-1	1	-1
6	6	-30	20	-120	-1	1	-1
7	5	30	20	-120	1	1	-1
8	11	30	20	-120	1	1	-1
9	10	-30	6	120	-1	-1	1
10	12	-30	6	120	-1	-1	1
11	17	30	6	120	1	-1	1
12	16	30	6	120	1	-1	1
13	1	-30	20	120	-1	1	1
14	13	-30	20	120	-1	1	1
15	14	30	20	120	1	1	1
16	7	30	20	120	1	1	1
17	8	0	13	0	0	0	0
18	3	0	13	0	0	0	0

The calibration experiments accommodate the calibration model shown in equation (8).

$$R_i = a_i + \sum_{j=1}^{3} \beta_{i,j} F_j + \sum_{j=1}^{3} \sum_{k=j+1}^{3} \beta_{i,j,k} F_j F_k \tag{8}$$

Equation (8) represents the forward calibration model, which models the electrical response of each balance component as a function of applied forces. In this equation, R_i

is the electrical response (volts) for the ith balance component, where i varies from one to three, since it is a three component calibration. a_i is the intercept for the ith model. $\beta_{i,j}$ and $\beta_{i,j,k}$ are the linear and two-factor-interaction coefficients, respectively, and F_j or F_k corresponds to the applied component loads (lbs or in-lbs). Each model contains two degrees of freedom for estimation of lack-of-fit and nine degrees of freedom for estimation of pure error.

Table 4. Ideal Off-Center System Calibration Experiment

Off-Center System							
		Natural Units			Coded Units		
Std Run#	Run#	NF (lbs)	AF (lbs)	PM (in-lbs)	NF	AF	PM
1	1	-30	-20	-120	-1	-1	-1
2	14	-30	-20	-120	-1	-1	-1
3	15	30	-20	-120	1	-1	-1
4	6	30	-20	-120	1	-1	-1
5	18	-30	20	-120	-1	1	-1
6	8	-30	20	-120	-1	1	-1
7	16	30	20	-120	1	1	-1
8	4	30	20	-120	1	1	-1
9	2	-30	-20	120	-1	-1	1
10	9	-30	-20	120	-1	-1	1
11	13	30	-20	120	1	-1	1
12	5	30	-20	120	1	-1	1
13	10	-30	20	120	-1	1	1
14	7	-30	20	120	-1	1	1
15	17	30	20	120	1	1	1
16	11	30	20	120	1	1	1
17	12	0	0	0	0	0	0
18	3	0	0	0	0	0	0

When implementing a designed experiment, it is often not feasible to perfectly set factor settings for each trial. In these cases, factors are set as close as possible to the ideal

settings, while the actual settings are recorded during the experiment and are used in the regression analysis. For this research, the ideal calibration experiments contain loads prescribed during the preliminary design phase of each system; however, due to fabrication errors and limited resources, the actual calibration loads deviate from ideal settings. The actual calibration loads for each system are shown in table 5 and table 6. Compared to the ideal designs, the actual designs show a slight departure from orthogonality. This departure can result in multi-collinearity between parameters in the regression model, which is assessed using metrics such as variance inflation factors and correlation coefficients, which are detailed in appendix A. By inspection of the variance inflation factors, shown in table 7, it is evident that the departure from orthogonality is tolerable since all variance inflation factors are nearly one.

Table 5. Actual Centered System Calibration Experiment

Centered System							
		Natural Units			Coded Units		
Std Run#	Run#	NF (lbs)	AF (lbs)	PM (in-lbs)	NF	AF	PM
1	4	-30.28	6.00	-99.06	-0.92	-0.98	-0.86
2	18	-30.33	6.00	-99.11	-0.92	-0.98	-0.86
3	9	32.86	6.04	-110.78	0.99	-0.97	-0.97
4	15	32.89	6.05	-110.92	0.99	-0.97	-0.97
5	2	-30.74	15.97	-107.06	-0.93	0.99	-0.93
6	6	-30.76	15.97	-106.99	-0.93	0.99	-0.93
7	5	33.21	16.04	-114.41	1.00	1.00	-1.00
8	11	33.28	16.03	-114.76	1.00	1.00	-1.00
9	10	-32.69	6.00	112.04	-0.99	-0.98	0.96
10	12	-32.74	6.01	112.25	-0.99	-0.97	0.97
11	17	30.42	5.88	98.57	0.91	-1.00	0.85
12	16	30.45	5.88	98.68	0.91	-1.00	0.85
13	1	-33.05	15.97	116.19	-1.00	0.99	1.00
14	13	-33.05	15.99	116.17	-1.00	0.99	1.00
15	14	30.89	15.84	107.14	0.93	0.96	0.92
16	7	30.89	15.84	107.10	0.93	0.96	0.92
17	8	0.01	10.97	0.04	0.00	0.00	-0.01
18	3	0.01	10.98	0.08	0.00	0.00	-0.01

Table 6. Actual Off-Center System Calibration Experiment

Off-Center System							
		Natural Units			Coded Units		
Std Run#	Run#	NF (lbs)	AF (lbs)	PM (in-lbs)	NF	AF	PM
1	1	-31.19	-19.30	-125.52	-1.00	-0.99	-1.00
2	14	-31.26	-19.27	-125.38	-1.00	-0.99	-1.00
3	15	30.98	-18.53	-124.15	0.99	-0.95	-0.99
4	6	30.98	-18.53	-124.16	0.99	-0.95	-0.99
5	18	-30.34	17.69	-121.48	-0.97	0.97	-0.97
6	8	-30.39	17.73	-121.68	-0.97	0.97	-0.97
7	16	30.70	18.28	-122.07	0.98	1.00	-0.97
8	4	30.66	18.27	-122.08	0.98	1.00	-0.97
9	2	-30.92	-18.62	123.06	-0.99	-0.95	0.99
10	9	-30.96	-18.67	123.11	-0.99	-0.96	0.99
11	13	31.25	-19.35	124.21	1.00	-0.99	1.00
12	5	31.34	-19.52	124.34	1.00	-1.00	1.00
13	10	-30.68	18.20	122.22	-0.98	1.00	0.98
14	7	-30.69	18.20	122.18	-0.98	1.00	0.98
15	17	30.32	17.60	121.28	0.97	0.96	0.98
16	11	30.33	17.60	121.38	0.97	0.96	0.98
17	12	0.00	0.00	0.00	0.00	0.03	0.00
18	3	0.00	0.00	0.00	0.00	0.03	0.00

Table 7. Variance Inflation Factors for the Calibration Experiments

	Variance Inflation Factors (VIF)			
	Off-Center System		Centered System	
Parameter	Ideal	Actual	Ideal	Actual
β_1	1.000	1.001	1.000	1.008
β_2	1.000	1.001	1.000	1.000
β_3	1.000	1.001	1.000	1.011
β_{12}	1.000	1.001	1.000	1.008
β_{13}	1.000	1.001	1.000	1.000
β_{23}	1.000	1.001	1.000	1.011

4.3 Tare Loads

The calibration loads presented in the previous section reflect the difference between the total load and tare load. The calibration loads represent the gravitational and centrifugal force imparted by the attached weight. The tare loads represent the force imparted by the fixture and balance weights. Tare runs are performed before each run in the calibration matrix, from which tare loads are measured for a particular configuration of the calibration system. The tare loads are dynamic, meaning that a tare load is taken while the balance is spinning at the specified angular velocity, albeit with no weights attached. The centered system has the advantage that the tare loads are nearly identical for each calibration load since the balance remains fixed in the same position throughout the calibration experiment. On the other hand, the off-center system has varying tare loads since the balance is oriented in various off-center, asymmetric configurations throughout the calibration experiment. The centered system has tare loads that are approximately 5% of the balance load capacity, while the off-center system has tare loads that are 10-40% of the full scale load. The tare load to calibration load ratio for the SVS is about 5%. A smaller tare load is desirable so that the fitted calibration model will span

the majority of the balance design load space. Large tare loads could also lead to calibration model extrapolation to estimate loads outside the delta space, resulting in an increased prediction variance for that estimate.

4.4 Centered System Mechanical Design

As mentioned before, the calibration loads were based on the balance design load capabilities of the NASA UT-36 force balance. The mechanical hardware required to implement the planned calibration experiments is sized according to the calibration loads. The purpose of the hardware is to provide an accurate and repeatable means of positioning and fixing the non-metric end of the balance on the rotating table. Additionally, the hardware shall provide a repeatable and accurate means of attaching weight to the metric end of the balance.

The centered system, shown in figure 10, has the balance centered on the rotating table with the balance axial force axis parallel to the axis of rotation. A load is applied by attaching a mass to one of the six attachment points at the end of the arms.

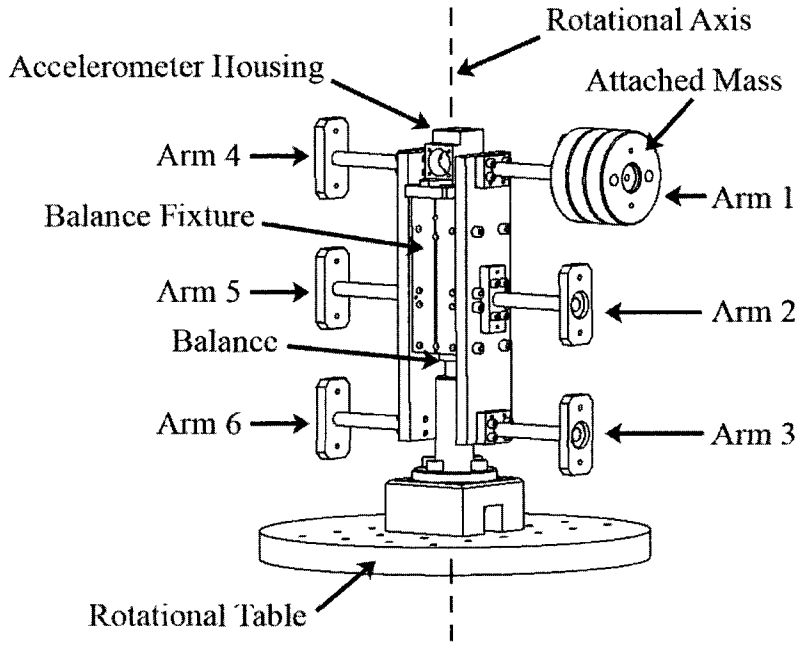

Figure 9. Centered System Overview

Opposing force vector loading schemes can be achieved by attaching mass on opposite sides. These coupled opposing force vectors allow for pure moment application to the balance if the axial force contribution is tared out. As a result, the centered system is capable of employing unique combinations of simultaneously applied loads. The centrifugal force from the mass of the balance is minimized by aligning the center of gravity of the balance with the axis of rotation of the table. This helps decrease the tare loads relative to the calibration loads. As a rule of thumb, tare loads are supposed to be less than five percent of the total load [2].

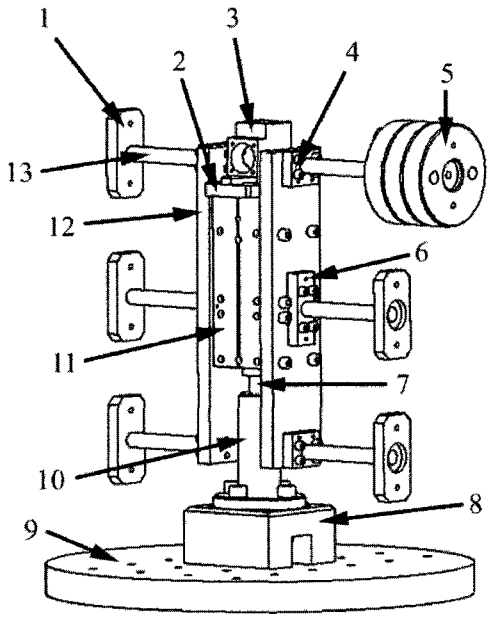

Figure 10. Centered System Parts Layout

Table 8. Centered System Parts

Part #	Name	Qty	Existing Part?
1	Weight Adapter	6	N
2	AoA Adapter	6	N
3	AoA Fixture	1	Y
4	Outer Arm Adapter	4	N
5	Attached Weight	various*	Y
6	Middle Arm Adapter	2	N
7	UT-36 Balance	1	Y
8	Table Adapter	1	N
9	Rotating Table	1	Y
10	Taper Adapter	1	Y
11	Balance Fixture	1	Y
12	Fixture Adapter	2	N
13	Arm	6	N

The centered system required design and fabrication of numerous parts; however, some parts already existed, such as the balance fixture, taper adapter and accelerometer housing, as show in figure 10 and table 8. The newly fabricated parts were designed to adapt to the existing parts and were sized around the calibration loads of the experiment. The fixture adapter width and arm diameter were sized such that the deflection due to the maximum calibration load was less than the uncertainty of the parts dimensions. The finite element analysis, presented in section J, demonstrates that the deflection under maximum load is approximately 0.005", which is less than the part's dimensional uncertainty of 0.01". The arms were welded to the weight adapter at one end and welded to the arm adapter on the other. A source of fabrication error stemmed from these welds since angle orthogonality between welded parts was difficult to achieve. The centerline axes of arm two and five are colinear with the balance moment center and perpendicular to the balance axis. The other four arms are positioned equally above and below the moment center, as shown in figure 9. The distance between arms was dictated by the calibration load ratios. Since the taper adapter was not meant to mate with the UT36, special alterations were required. Specifically, threads were machined onto the taper adapter so that a draw nut, which has opposite threads at either end, could fasten the balance with the taper adapter. This required fabrication of the new draw nut shown in figure 11.

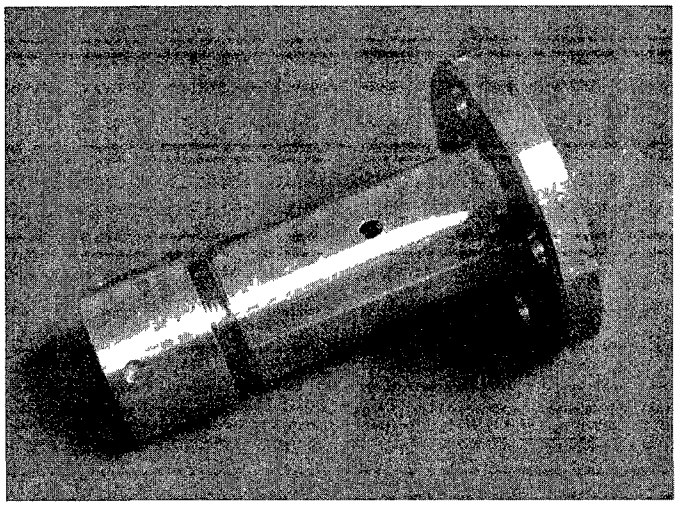

Figure 11. Draw Nut Fabricated for the UT-36

The table adapter was designed to fit the taper adapter to the table. An opening was machined into the side of the table adapter to allow for the balance wires to exit through this orifice and connect to the slip-ring panel shown in figure 12. The CAD drawings of the centered system can be found in appendix D.

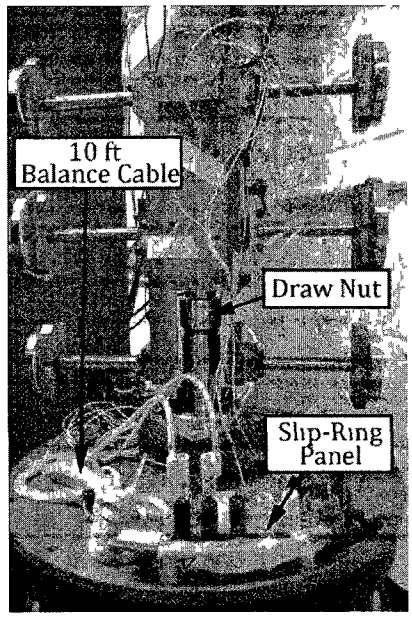

Figure 12. Centered System

The arm adapters are mated to the fixture adapter using two dowels, and the fixture cover is mounted to the balance fixture using two dowels. The two dowel approach is used to ensure repeatable alignments between mated hardware. On top of the balance fixture is an accelerometer package that hosts three mutually orthogonal accelerometers. The accelerometer package is doweled to the fixture such that the balance's coordinate system is aligned with accelerometer's coordinate system. The accelerometer package was used to measure the initial orientation of the balance. While this initial angle should be nominally zero, table alignment errors and fixture fabrication errors proved otherwise.

The generic governing equations are applied to each arm of the centered system and then summed as shown in equations (9) through (12). In equations (9) through (12), NF_i corresponds to the normal force imparted by the attached weight on the ith arm. There are six arms; therefore, i varies from one to six.

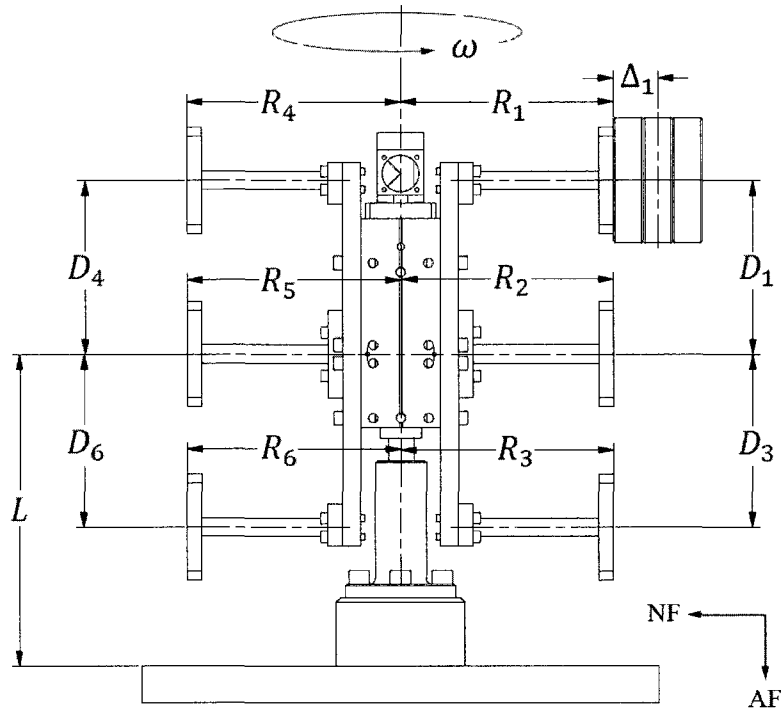

Figure 13. Centered System Modeling Example

$$NF_\iota = -m_\iota\omega^2[T_x + sin(\theta)(L + D_\iota) + cos(\phi_\iota)cos(\theta)(R_\iota + \Delta_\iota) - sin(\phi_\iota)sin(\theta)(R_\iota + \Delta_\iota)]cos(\theta) - m_\iota g cos(\alpha)sin(\theta) \quad (9)$$

$$AF_\iota = m_\iota\omega^2[T_x + sin(\theta)(L + D_\iota) + cos(\phi_\iota)cos(\theta)(R_\iota + \Delta_\iota) - sin(\phi_\iota)sin(\theta)(R_\iota + \Delta_\iota)]sin(\theta) + m_\iota g cos(\alpha)cos(\theta) \quad (10)$$

$$PM_\iota = [cos(\phi_\iota)D_\iota - sin(\phi_\iota)(R_\iota + \Delta_\iota)]NF_\iota + [sin(\phi_\iota)D_\iota - cos(\phi_\iota)(R_\iota + \Delta_\iota)]AF_\iota \quad (11)$$

$$NF_{Tot} = \sum_\iota^6 NF_\iota \qquad AF_{Tot} = \sum_\iota^6 AF_\iota \qquad PM_{Tot} = \sum_\iota^6 PM_\iota \quad (12)$$

The arm lengths, R_i, and the moment arm distances, D_i, were designed to meet the load requirements of the calibration design matrix. The parts were measured with vernier calipers while the system was in its final assembled state. The measured arm lengths and moment arm distances, shown in table 9 and table 10, are held constant throughout the experiment. Similarly, the distance between the balance attachment point and the balance moment center, L, is also held constant and is equal to 8.563 inches.

Table 9. Arm Lengths for the Centered System

R_1	6.176 in
R_2	6.148 in
R_3	6.133 in
R_4	-6.178 in
R_5	-6.158 in
R_6	-6.175 in

Table 10. Moment Arm Distances for the Centered System

Arm #	D (in)
D_1	4.701
D_2	0.000
D_3	-4.790
D_4	4.713
D_5	0.000
D_6	-4.734

As stated before, the variables of the experiment are mass location, mass quantity and rotational velocity. Table 11 shows the settings required to achieve the calibration loads. While numerous combinations of independent variables could have achieved the required

loading conditions, the settings shown in table 11 were chosen to represent a broad range of each possible setting.

Table 11. Independent Variable Settings for the Centered System Experiment

Std Run#	m_1 (lbm)	m_2 (lbm)	m_3 (lbm)	m_4 (lbm)	m_5 (lbm)	m_6 (lbm)	ω (rev/s)
1	2.5	3.5	0	0	0	0	2.69
2	2.5	3.5	0	0	0	0	2.69
3	0	0	0	0	0	6	2.69
4	0	0	0	0	0	6	2.69
5	3.5	8	4.5	0	0	0	1.59
6	3.5	8	4.5	0	0	0	1.59
7	3	0	0	0	3	10	1.99
8	3	0	0	0	3	10	1.99
9	0	0	6	0	0	0	2.69
10	0	0	6	0	0	0	2.69
11	0	0	0	2.5	3.5	0	2.69
12	0	0	0	2.5	3.5	0	2.69
13	0	3	10	3	0	0	1.99
14	0	3	10	3	0	0	1.99
15	0	0	0	3.5	8	4.5	1.59
16	0	0	0	3.5	8	4.5	1.59
17	5.5	0	0	5.5	0	0	0
18	5.5	0	0	5.5	0	0	0

In figure 13, the extra arm distance Δ_i is a function of the applied weight. When multiple weights are attached on one arm, the center of gravity of the group of weights is extended and the arm distance becomes larger. When there is no weight attached, the extra arm distance, Δ_i, is zero. The attached weights used for this experiment come in three different sizes: 2 lbm, 1 lbm and 1/2 lbm. The weight set is borrowed from an existing calibration system since the weights are already calibrated. The 2 lbm weight has a thickness of 0.8" while the 1 lbm and 1/2 lbm weights have a 0.4" thickness. For a

given load, the fewest number of weights are used. This corresponds to the following calculated Δ_i values for the given weights shown in table 12. The effect of the difference between standard and local gravity was neglected in this research.

Table 12. Extra Arm Length Distances

m_i (lbm)	Δ_i (inches)
1.5	0.33
2.0	0.40
2.5	0.52
3.0	0.60
3.5	0.71
4.5	0.91
5.5	1.11
6.0	1.20
8.0	1.60
10.0	2.00

The table was leveled using an accelerometer package fixed on top of the center of the table. Leveling screws near the base of the table were adjusted until the accelerometer package output in both horizontal axes was nominally zero. This means that the misalignment angle, α, was nominally zero throughout the experiment, with an uncertainty dictated by the accelerometer package.

The initial balance orientation was measured by mounting an accelerometer package on top of the balance fixture while on the table. Using the measured gravity vectors, the initial pitch and yaw angles of the balance were calculated. The initial pitch angle is used as a bias offset throughout the experiment, while the calculated yaw angle is neglected since the model formulation is limited to two dimensions. Calibration of the

accelerometer package was performed using the A.G. Davis table at NASA LaRC. Details about the angle calculation and accelerometer calibration are presented in appendix E.

Deflections constants were used to calculate the pitch angle while the balance was under load. The deflection constants were obtained from a previous calibration of the UT-36 using a manual stand calibration system. The deflection constants can be found in appendix F and have units of arc-secs per lb or in-lb. These constants were extracted by assuming the balance structure acts as a simple spring. Using these constants, the balance deflection angle is calculated as a function of applied loads, as shown in equation (13).

$$\theta_{defl} = (-0.0200NF - 0.0425PM)(1/60) \tag{13}$$

In this equation, the right hand side is divided by a factor of 60 to convert from minutes to degrees. The minus sign before each constant reflects the fact that a positive normal force or positive pitching moment corresponds to a negative pitch angle, according to figure 13. The balance pitch angle for each run is calculated as the deflection angle plus the initial balance offset angle. Table 13 shows the calculated balance pitch angles for each run of the experiment.

Table 13. Computed Deflection Angle for the Centered System

Std Run#	θ (deg)	Std Run#	θ (deg)
1	0.080	10	-0.069
2	0.080	11	-0.080
3	0.068	12	-0.080
4	0.068	13	-0.071
5	0.086	14	-0.071
6	0.086	15	-0.086
7	0.070	16	-0.086
8	0.070	17	-0.005
9	-0.068	18	-0.005

4.5 Off-Center System Mechanical Design

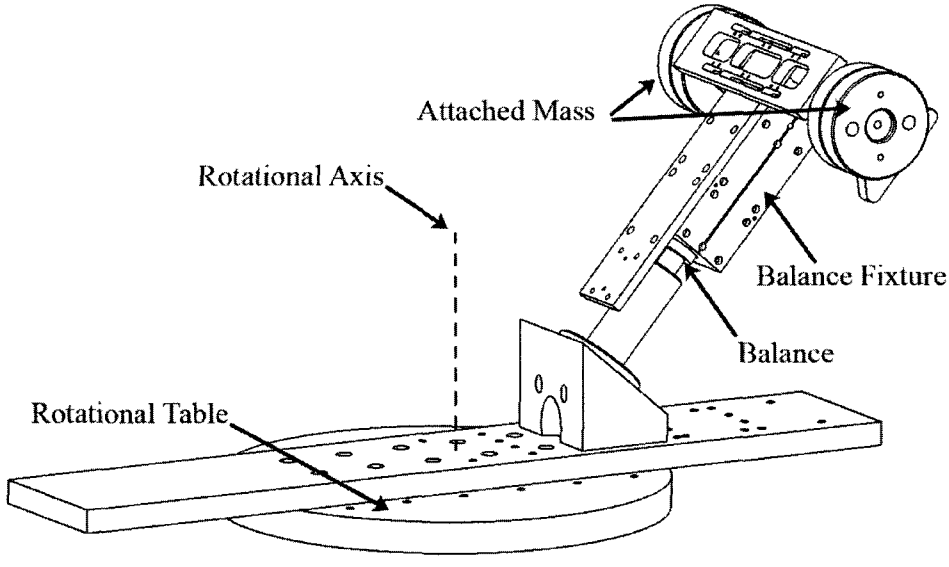

Figure 14. Off-Center System

The general layout of the off-center system is shown in figure 14. Similar to the centered system, the number of independent variables for the off-center system is

minimized to reduce system complexity and cost. Here, the independent variables are translation offset, pitch angle, roll angle, angular velocity and moment arm distance, as shown in figure 15. The translation offset, T_x, is changed by fastening the wedge adapter at different locations along the table adapter. The pitch angle is determined by the wedge adapter selection, while the roll angle is adjusted by detaching the balance from the wedge, and fastening at the specified roll angle. To satisfy the loading requirements of the calibration experiment, only two roll angles are required: 0 and 180 degrees. A threaded hole pattern on the fixture cover allows for the arm bracket to fasten at various locations, which effectively alters the moment arm distance, D.

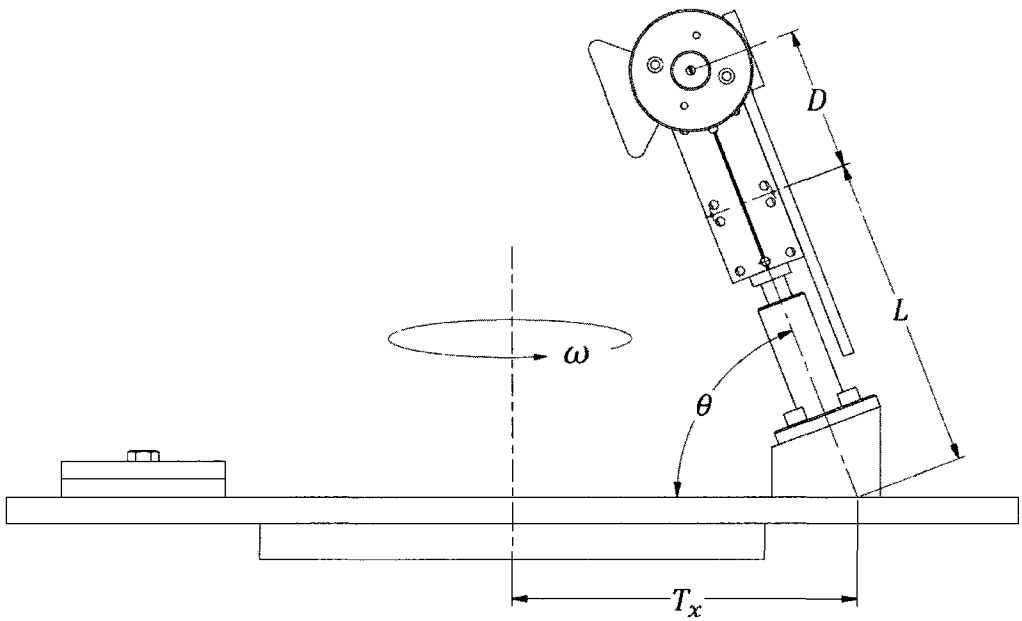

Figure 15. Off-Center System

For each loading configuration, the attached weight is equally spaced on either side of the arm bracket so that the center of gravity of attached weight is coincident with the axis of the balance. The arm bracket is an existing part, which is used as a force positioning system for low-weight SVS calibrations at NASA LaRC. The calibrated weights used for the centered system are similarly used here. Each part of the off-center system is indentified in figure 16. The corresponding parts numbers are shown in table 14. CAD drawings of the off-center system are shown in appendix G.

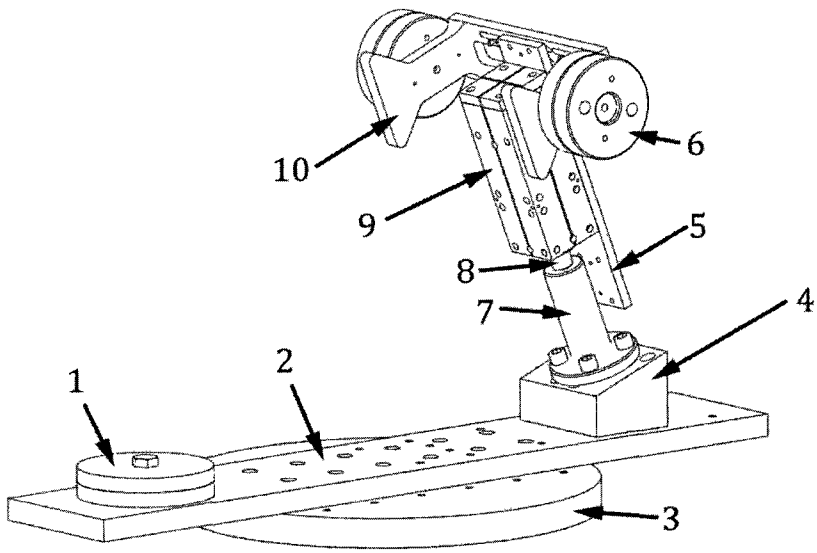

Figure 16. Off-Center System

Table 14. Off-Center System Parts

Part #	Name	Qty	Existing Part?
1	Counter Weights	*various	Y
2	Table Adapter	1	N
3	Rotating Table	1	Y
4	Wedge	2	N
5	Fixture Cover	1	N
6	Attached Weight	*various	Y
7	Taper Adapter	1	Y
8	UT-36 Balance	1	Y
9	Balance Fixture	1	Y
10	Arm Bracket	1	Y

In contrast to the centered system, the off-center system uses a single applied force vector. As a result, the off-center system is subject to the single force vector loading constraint shown in equation (2). While this becomes an issue for six component calibrations, a three-component calibration involving NF, AF and PM is not affected by this constraint since RM, SF and YM are always zero, thereby satisfying equation (2).

The generic governing equations are applied to the off-center system, as shown in equations (14) through (16). In equation (14), q is equal to 1 if the balance has a zero degree roll angle (the balance is in its nominal state), while q is equal to -1 if the balance is rolled 180 degrees.

$$NF = q(-m\omega^2[T_x + sin(\theta)(L + D) + cos(\phi)cos(\theta)R - sin\phi sin\theta Rcos\theta - mgcos\alpha sin\theta) \quad (14)$$

$$AF = -m\omega^2[T_x + sin(\theta)(L + D) + cos(\phi)cos(\theta)R - sin(\phi)sin(\theta)R]sin(\theta) + mgcos(\alpha)cos(\theta) \quad (15)$$

$$PM = [cos(\phi)D - sin(\phi)R]NF + [sin(\phi)D + cos(\phi)R]AF \quad (16)$$

The independent variable settings for the experiment are shown in table 15. The rotational velocity and attached mass are held constant throughout the experiment, except for the center runs (standard run number 17 through 18). The moment arm distance, D, was designed for the ratio of the calibration loads and has two unique configurations throughout the experiment.

Table 15. Independent Variable Settings for the Off-Center System

Std Run#	m (lbm)	ω (rev/s)	L (inch)	T_x (inch)	θ_{wedge} (deg)	D (inch)	q
1	6.00	2.70	10.50	-1.40	40.80	4.00	1
2	6.00	2.70	10.50	-1.40	40.80	4.00	1
3	6.00	2.70	10.50	3.70	40.80	-4.00	-1
4	6.00	2.70	10.50	3.70	40.80	-4.00	-1
5	6.00	2.70	9.63	12.56	-20.92	4.00	1
6	6.00	2.70	9.63	12.56	-20.92	4.00	1
7	6.00	2.70	9.63	9.86	-20.92	-4.00	-1
8	6.00	2.70	9.63	9.86	-20.92	-4.00	-1
9	6.00	2.70	10.50	3.70	40.80	-4.00	1
10	6.00	2.70	10.50	3.70	40.80	-4.00	1
11	6.00	2.70	10.50	-1.40	40.80	4.00	-1
12	6.00	2.70	10.50	-1.40	40.80	4.00	-1
13	6.00	2.70	9.63	9.86	-20.92	-4.00	1
14	6.00	2.70	9.63	9.86	-20.92	-4.00	1
15	6.00	2.70	9.63	12.56	-20.92	4.00	-1
16	6.00	2.70	9.63	12.56	-20.92	4.00	-1
17	0.00	0.00	9.63	9.86	-20.92	-4.00	-1
18	0.00	0.00	10.50	3.70	40.80	-4.00	1

As shown in table 15, the experiment requires only two unique angle settings. In the experiment, there are 8 unique configurations, plus one center point run. Four of the unique configurations use one wedge adapter, while the other four configurations use the other. The distance between the balance attachment point and the balance moment center, L, is dependent on wedge selection. Figure 17 shows the factorial runs of the experiment.

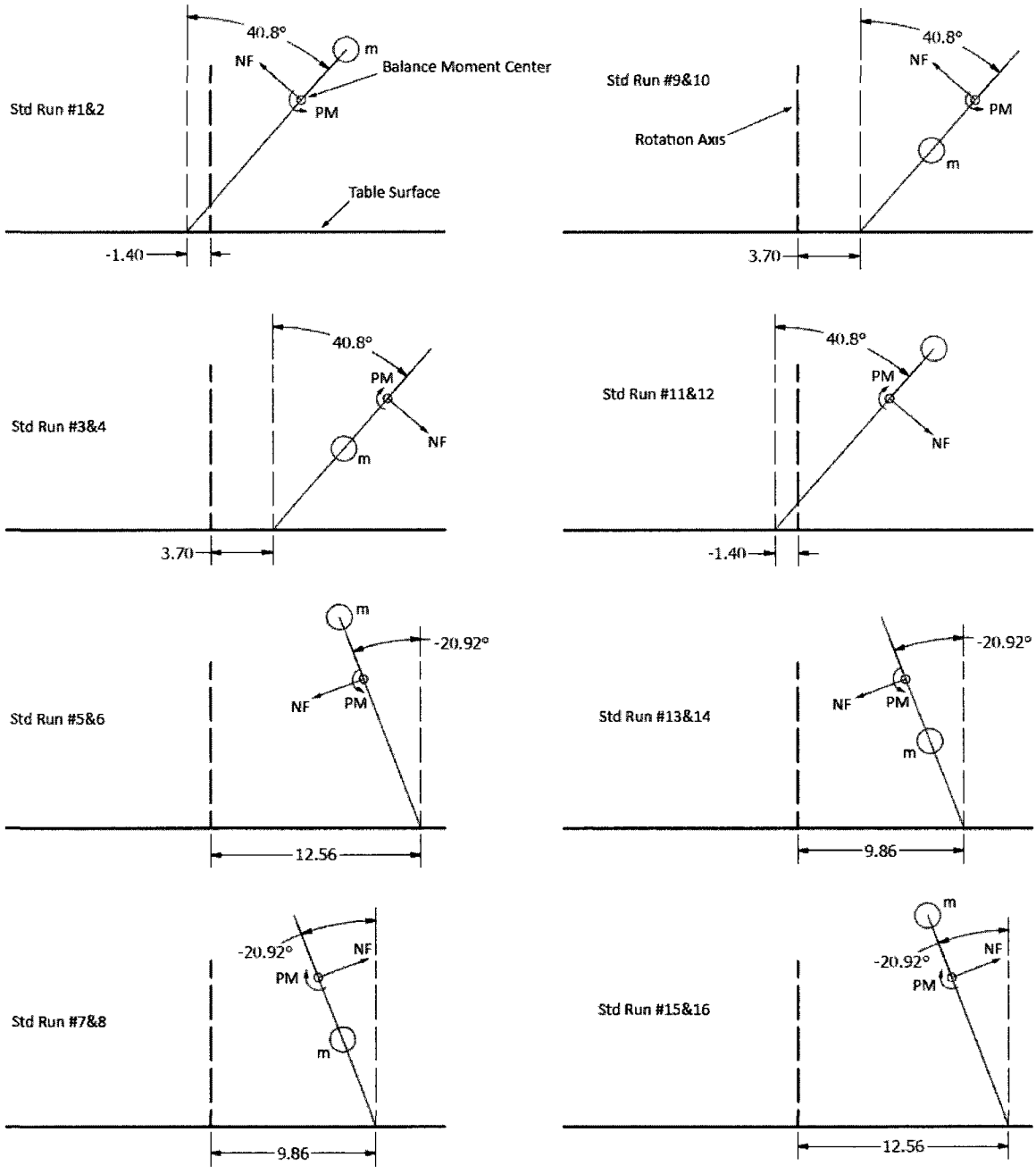

Figure 17. Sketch of the Off-Center System Factorial Runs

The initial pitch angles of the balance were calculated for each wedge, using the accelerometer output, while the balance was attached to the table. The deflection angles

were calculated using equation (17), where q is equal to -1 if the balance is rolled 180 degrees and equal to 1 otherwise. In contrast to the centered system calculation, the off-center system uses the total loads in the deflection equation, not the calibration loads.

$$\theta_{defl} = q(-0.0200NF - 0.0425PM)(1/60) \tag{17}$$

Table 16 summarizes the pitch angles for each run in the experiment.

Table 16. Computed Balance Angles for the Off Center System Experiment

Std Run#	θ_0 (deg)	θ_{defl} (deg)	θ (deg)
1	40.80	0.17	40.97
2	40.80	0.18	40.98
3	40.80	-0.03	40.77
4	40.80	-0.03	40.77
5	-20.92	0.17	-20.75
6	-20.92	0.17	-20.75
7	-20.92	-0.08	-21.00
8	-20.92	-0.08	-21.00
9	40.80	-0.03	40.77
10	40.80	-0.03	40.77
11	40.80	0.18	40.98
12	40.80	0.18	40.98
13	-20.92	-0.08	-21.00
14	-20.92	-0.08	-21.00
15	-20.92	0.17	-20.75
16	-20.92	0.17	-20.75
17	-20.92	0.00	-20.92
18	40.80	0.05	40.85

Counterbalancing is used to counteract centrifugal forces generated by the fixture, balance and attached weight. The purpose is to maintain a center of gravity location that is colinear with the table rotation axis. For each run, a specific amount of weight is used as a counterbalance. This precaution ensured that the table did not oscillate or tip during

testing A rubber mat was placed between counter weights to hinder movement and dampen vibrations The counter weights used were un-calibrated barbell weights, as shown in figure 18.

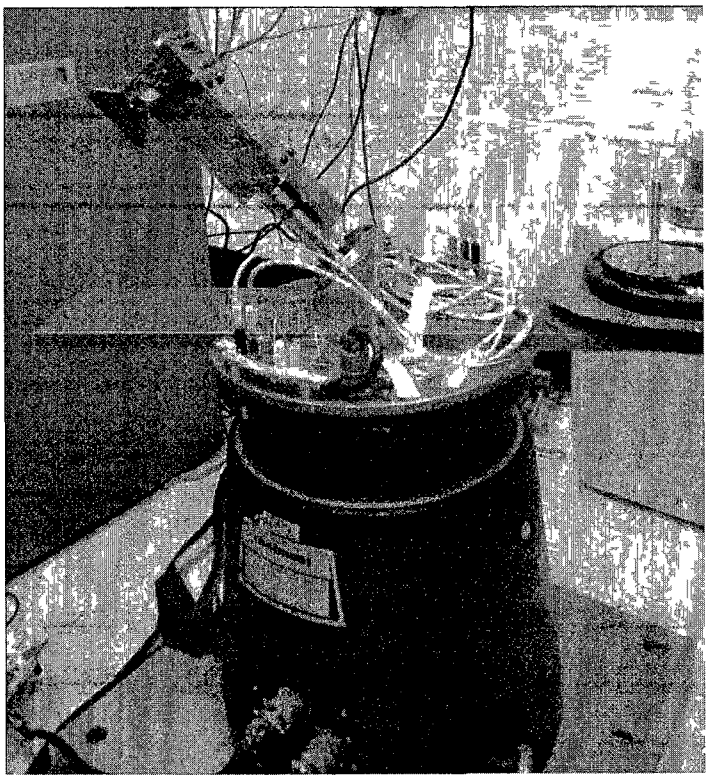

Figure 18. Off-Center System

4.6 Experimental Setup

Figure 19 shows the wiring setup for the experiments Six multi-meters, and two power supplies were connected via a single GPIB bus A GPIB to USB adapter was used to communicate with a computer using Labview. Within Labview, the instruments were

controlled remotely using SCPI language. The multi-meters were sampled simultaneously using a SCPI trigger command.

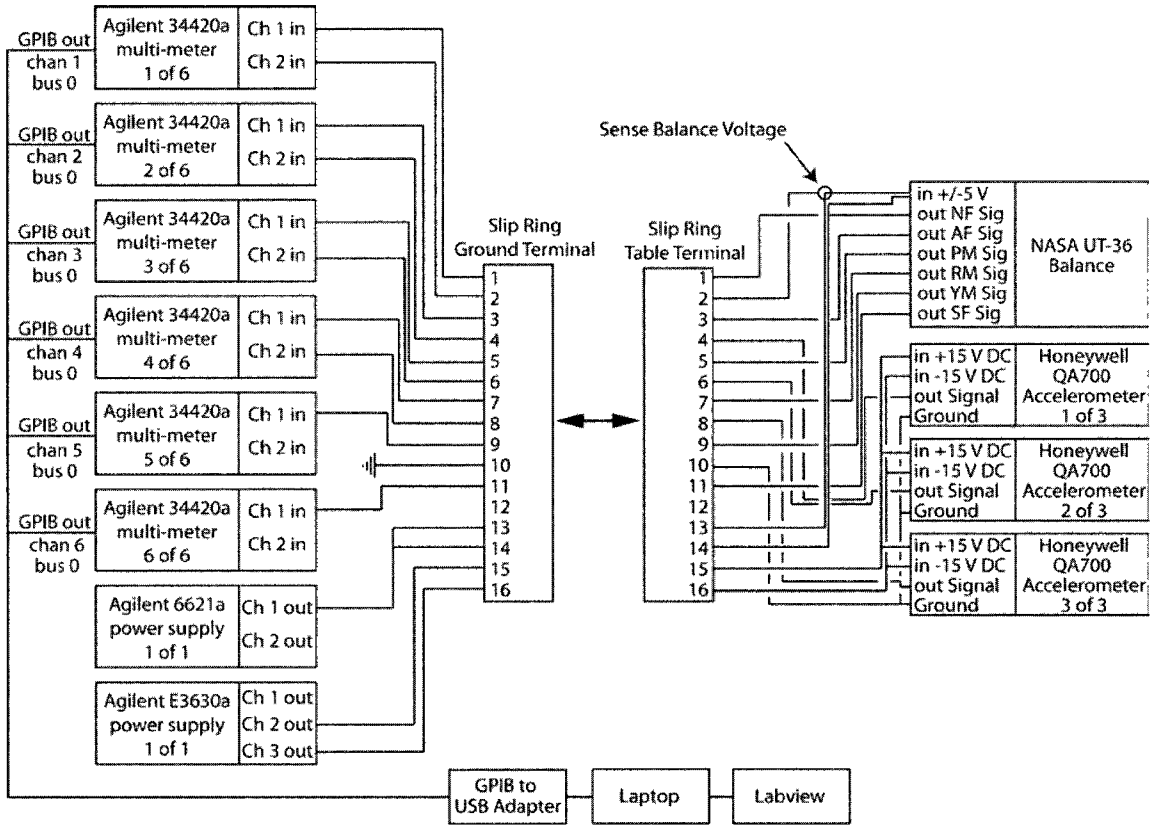

Figure 19. Wiring Diagram

An Agilent 6621A DC power supply is used to power the balance. The programming accuracy and read back accuracy of the 6621A are of little importance, since the Agilent 34420A multi-meter is used to monitor the supplied voltage. The noise of the 6621A is the important specification and is shown in table 17.

Table 17. Agilent 6621A Performance Specifications

Agilent 6621A DC Power Supply		
	Channels	2
Output Power	Low Range	0-20V, 0-2A
	High Range	0 to 50V, 0 to 0.8A
Programming Accuracy	Voltage	50 mV +0.06%
	Current	20 mA +0.16%
Readback Accuracy	Voltage	50 mV+0.05%
	+Current	4 mA +0.1%
	-Current	8 mA+0.2%
Noise	Voltage RMS	500μV
	Constant Current RMS	1mA

The UT-36 balance had a 0.2 mA current draw due to the excitation voltage, which is abnormally large since it is an older style balance that uses smaller resistors compared to current balances. This causes the UT-36 to generate more heat, which could contribute to thermal related balance error. To defend against this, all instruments were left on over night before the experiment to allow the system to reach thermal equilibrium in a temperature controlled room.

The Agilent E3630A power supply is used to power the accelerometer package, which requires a positive and negative 15 V DC voltage. The performance specifications for the E3630A are shown in table 18.

Table 18. Agilent E3630A Performance Specifications

Agilent E3630A DC PS	
Channels	3
Ranges	0 to 6V, 2.5A
	0 to 20V, 0.5A
	0 to -20V, 0.5A
Noise	<350μV RMS

The Agilent 34420A was chosen over an A/D DAQ card mainly for accuracy purposes, which it is able to achieve through filtering and averaging within the unit. Measurements are sampled fairly slowly, (0.3 samples per second), which is a function of integration time (number of power line cycles (NPLC)), range, and analog and digital filter settings. For this experiment, the meters were set for 100 PLCs at a 10mV range, with analog filters on. Thirty samples were taken for each run, which amounted to approximately 10 seconds of data sampling. Each run took approximately 30 seconds, which included table acceleration and deceleration phases.

Table 19. Agilent 34420A Accuracy Specifications

Agilent 34420A Accuracy Specifications ±(% of reading + % of range)***				
	Range	24 Hour	90 Day	1 year
DC Voltage	1 mV	0.0025+0.0020	0.0040+0.0020	0.0050+0.0020
	10 mV	0.0025+0.0002	0.0040+0.0002	0.0050+0.0003
	100 mV	0.0015+0.0003	0.0030+0.0004	0.0040+0.0004
	1 V	0.0010+0.0003	0.0025+0.0004	0.0035+0.0004
	10 V	0.0002+0.0001	0.0020+0.0004	0.0030+0.0004
	100 V	0.0010+0.0004	0.0025+0.0005	0.0035+0.0005

** after 2 hour warm-up, resolution = 7.5 (100 NPLC), filters off

To examine the contribution of multi-meter error as a percentage of the full scale output the following example is given. The normal force component of the UT-36 has a 4.85 mV/5V full scale output. Assuming a 10mV range and a 90 day accuracy, the multi-meter error is calculated as follows.

$$\left[\frac{.004}{100} \times 4.85E-3\,V\right] + \left[\frac{.0002}{100} \times 10\,E-3\,V\right] = 0.214\,\mu V \tag{18}$$

The percent of full scale error is

$$\frac{0.214\,E-6\,V}{4.85E-3\,V} = \boxed{0.004\%} \tag{19}$$

which is sufficiently less than the 0.05% full scale error desired level; therefore, this type of error is negligible.

Table 20. Agilent 34420A Noise Specifications

Agilent 34420A DC Voltage Noise			
	Observation Period		
Range	2-Minute RMS Noise	2-Minute P2P Noise	24-Hour P2P Noise
1 mV	1.3nVrms	8nVpp	12nVpp
10 mV	1.5nVrms	10nVpp	14nVpp
100 mV	10nVrms	65nVpp	80nVpp
1 V	100nVrms	650nVpp	800nVpp
10 V	450nVrms	3μVpp	3.7μVpp
100 V	11μVrms	75μVpp	90μVpp

Table 21. Agilent 34420A Reading Specifications

Agilent 34420A Operating Characteristics			
	Digits	Integration Time	Readings / s
dcV	7.5	200 plc	0.15
	7.5	100 plc	0.3
	6.5	20 plc	1.5
	6.5	10 plc	3
	5.5	1 plc	25
	5.5	0.2 plc	100
	4.5	0.02 plc	250

Honeywell QA 700 accelerometers are used for angle measurements. The performance specifications for the QA700 are shown in table 22. The accelerometers are used to measure the balance angle while at rest and to level the rate table in the lab. The accelerometers are not used to measure the balance deflection angles while the table is rotating; instead, deflection constants are used.

Table 22. Honeywell QA700 Performance Specifications

Input Range	±30 g
Bias	<8 mg
One Year Composite Repeatability	1.2 mg
Temperature Sensitivity	<70 µg/°C
Axis Misalignment	<2000 µrad
Vibration Rectification	<50 µg/g^2 rms for (50-200Hz)
	<100 µg/g^2 rms for (200-750Hz)
	<150 µg/g^2 rms for (750-2000Hz)
Intrinsic Noise	<7 µg rms for (0-10Hz)
	<70 µg rms for (10-500Hz)
	<1500 µg rms for (500-10,000Hz)

An accelerometer cannot be used to measure the angle of the balance while the table is rotating because the centripetal portion of the acceleration cannot be decoupled from the acceleration due to gravity; therefore, the balance deflection angle cannot be inferred. If the balance didn't deflect during rotation, the distance between the accelerometer seismic mass and the rotation axis could be measured. Then the centripetal acceleration could be calculated and subtracted from the accelerometer output. Using this output, the angle of the balance could be calculated. Unfortunately, the balance does deflect; therefore, the additional centripetal acceleration due to deflection cannot be decoupled from acceleration due to gravity. For example, consider an accelerometer placed on top of a 0.25 meter rod in the center of a rotating table. At rest, the accelerometer sensitive axis is perpendicular to gravity, and the seismic mass and axis of the rod is aligned with the rotational axis of the table. When the table rotates at 17 rad/s, assume the rod deflects 0.2 degrees, which is representative of the deflection shown in VACS. The output of the accelerometer is calculated as shown in equation (20).

$$a_x = \frac{(0.25m)sin(0.20°)(17\ rad/s)^2}{9.806\ m/s^2} = 0.0257\ g's \tag{20}$$

The angle is calculated from the component of acceleration using equation (21).

$$\theta = sin^{-1}(0.0257) = 1.47° \tag{21}$$

This result means that the output of the accelerometer could have as much as 1.47° of error in the reading due to the additional centripetal acceleration caused by balance

deflection. For VACS, this is excessive; therefore, an alternative instrument or method should be used in future systems.

Table 23. Rate Table Performance Specifications

Contraves Rate Table System	
Manufacturer	Contraves Corp
Model	800HL (IM-8661)
Peak Torque, nominal	30 ft-lbs
Load Capacity	1000 lbs
Max Rate	1000 deg/s
Slip Ring Circuits	23
Rate Accuracy (>500 deg/s)	0.4 deg/s
Date of previous calibration	03/14/2005
Manufacture Date	1984

Performance specifications for the rate table are shown in table 23. The Model 800 HL rate table uses direct drive components, thereby avoiding mechanical gears or ball disc drives, which provides smooth speed control. The rate accuracy is evaluated over one revolution. The rate accuracy is specified for high speed mode, where the rate is set using the command module, inputted on a numeric pad. Slip ring terminals are used to feed signals from the rotating frame and ground frame, as shown in figure 20.

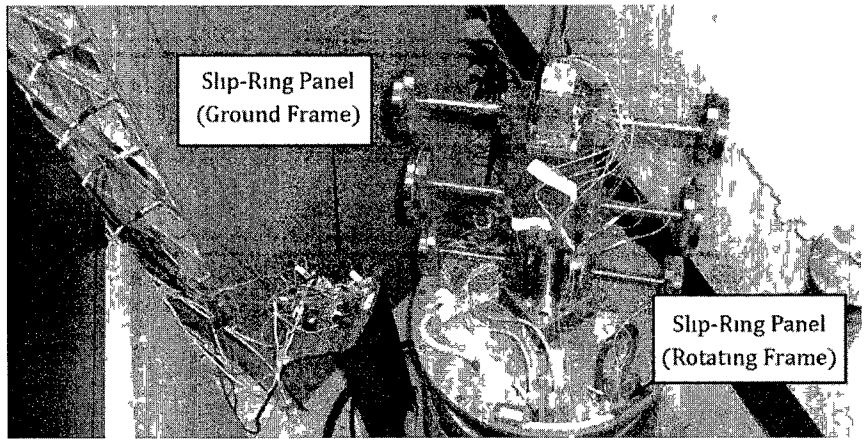

Figure 20. Slip Ring Terminals

4.7 Calibration Experiment Results

For each run in the calibration experiments, the applied load error, $\boldsymbol{E}$, is calculated as the difference between the experimentally measured loads from the force balance and the loads predicted using the physics based models, as shown in equation (22) or (23).

$$\boldsymbol{E} = \boldsymbol{Y}_{exp} - \boldsymbol{Y}_{pred} \tag{22}$$

$$\begin{bmatrix} E_{NF} \\ E_{AF} \\ E_{PM} \end{bmatrix} = \begin{bmatrix} Y_{exp\,,NF} \\ Y_{exp\,,AF} \\ Y_{exp\,,PM} \end{bmatrix} - \begin{bmatrix} Y_{pred\,,NF} \\ Y_{pred\,,AF} \\ Y_{pred\,,PM} \end{bmatrix} \tag{23}$$

The predicted loads are calculated using the physics-based models, which were previously formulated in equations (4) through (6). The experimentally measured loads are determined from the electrical balance signals, which are converted to forces and moments using a calibration model obtained from a previous calibration of the UT-36.

An iterative inverse prediction method is used to invert the forward calibration function to obtain the loads as a function of electrical signals of the balance. The iterative inverse prediction procedure is detailed in appendix H.

For comparison between systems, the applied load error is presented as a percentage of the full scale loads of the calibration experiments, referred to as "percent of full scale error" (%FSE). The normalizing full scale loads used for each system are shown in table 24.

Table 24. Full Scales Loads used to Calculate %FSE for Both Systems

NF (lbs)	AF (lbs)	PM (in-lbs)
30	20	120

The applied load error is plotted versus standard run number for each system in figure 21 and figure 22.

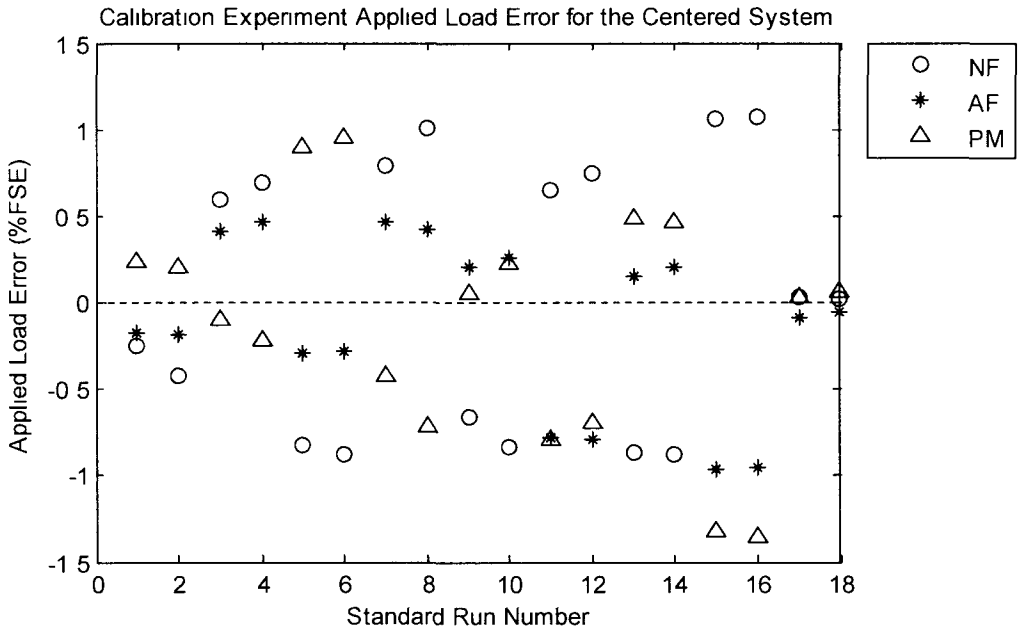

Figure 21. Applied Load Error for the Centered System Calibration Experiment

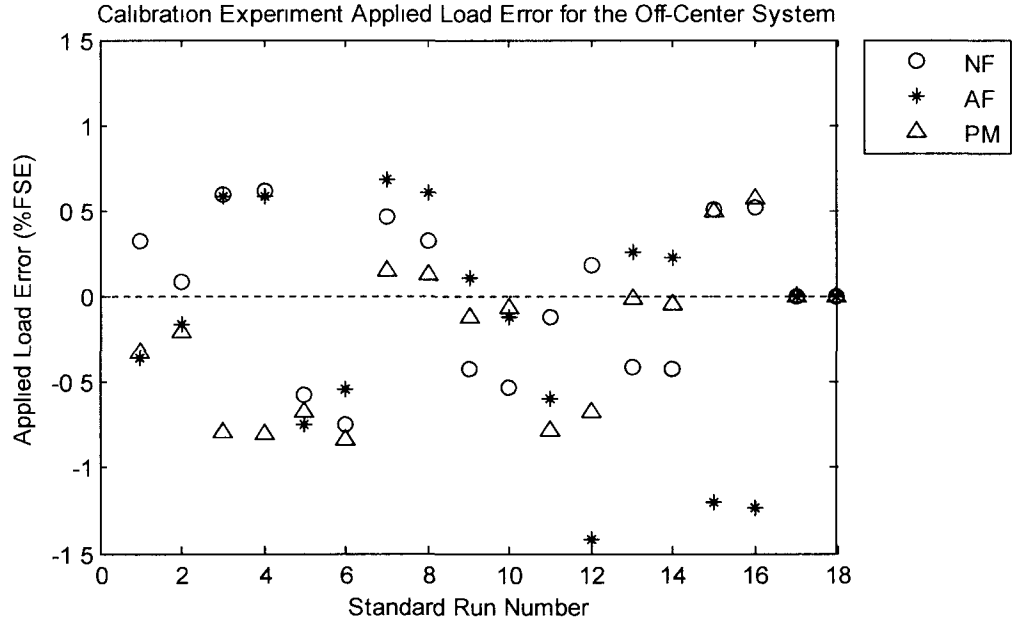

Figure 22. Applied Load Error for the Off-Center System Calibration Experiment

Summary statistics for the applied load errors are presented in table 25.

Table 25. Statistical Summary of Calibration Experiments Applied Load Error

	Centered System			Off-Center System		
	E_{NF}	E_{AF}	E_{PM}	E_{NF}	E_{AF}	E_{PM}
Mean (%FSE)	0.06	-0.16	-0.11	0.02	-0.18	-0.22
2σ (%FSE)	1.34	0.98	1.40	0.75	1.33	0.84

Table 25 shows that the mean applied load error is non-zero for the calibration experiments. This is especially true for axial force and pitching moment; however, this result is expected since it is assumed that bias error exists in applying the loads. To provide a basis to compare the tabulated applied load errors accuracies, consider the following. The applied load error must be substantially less than a quoted balance calibration accuracy in order to accommodate errors associated with the regression model fit and system noise.

Figure 23 shows a compilation of balance calibration accuracies expressed as box plots, which were obtained from the NASA balance database. This chart includes data from 208 six component balance calibrations. The middle line in each box is the median of the data, while the top and bottom of the box represent the 25th and 75th percentile. The whiskers extend to the most extreme data point the algorithm considers to be not outliers; although, it should be mentioned that each component contains about 5-10 outliers that are not plotted. The compilation contains information dating back to 2000.

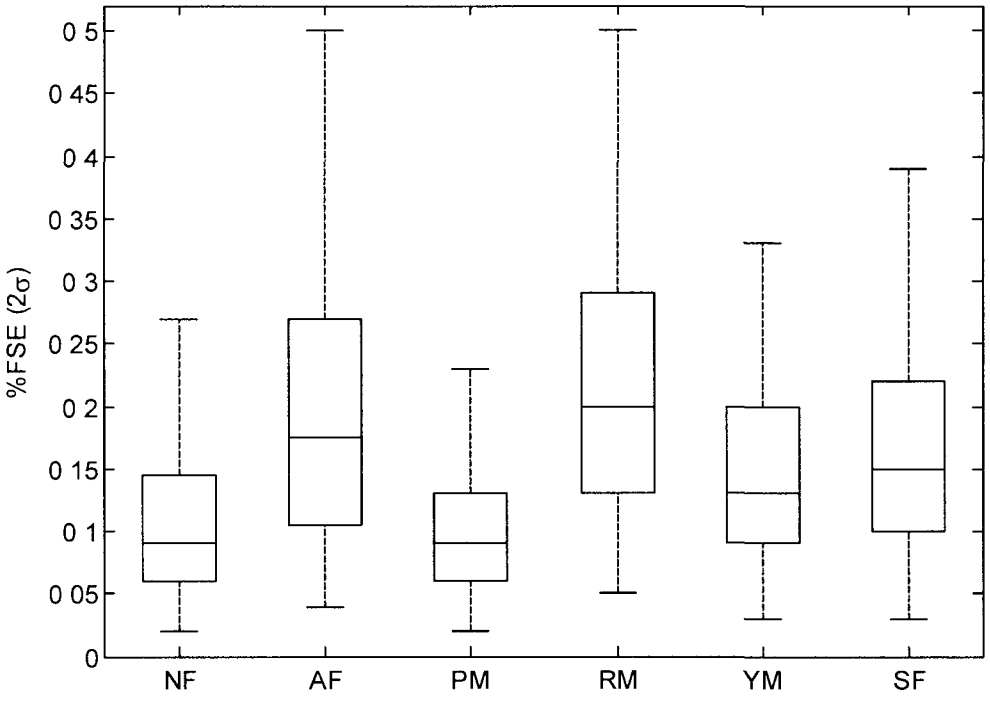

Figure 23. Calibration Accuracies for Balances in NASA LaRC Inventory

In figure 23 it can be seen that a typical six component balance calibration accuracy is approximately 0.2 %FSE. To achieve this level of calibration accuracy, the applied load error of the calibration system used must be much less than 0.2% in order to accommodate model fit error and system noise. In comparison, the VACS applied load error is about one order of magnitude larger. This result was anticipated since it is a proof-of-concept system; therefore, the objective was to verify that the applied load error is within the bounds of the predicted uncertainty. Even though the applied load error of the VACS calibration experiments is large, calibration models were fit to the VACS calibration experiment data for the purpose of comparing model coefficients to historical estimates. Details about this analysis are presented in appendix I.

5 UNCERTAINTY ANALYSIS

For the ideal production calibration system, the applied load error is negligible compared to the precision error and the error in fitting a regression calibration model. Hence, the purpose of the traditional balance calibration experiment is to quantify the uncertainty of the balance alone and not the calibration system. In contrast, VACS exhibits significant applied load error; therefore, this error must be characterized to verify the accuracy of each system and to provide a basis to recommended future system improvements. Accordingly, the primary objective of this section is to verify that the applied load error is within the uncertainty intervals predicted for each system. Successful verification implies that the majority of error contributions have been accounted for and that the systems have performed as expected. A secondary objective is to provide hardware specification requirements to yield a production quality system.

5.1 Experimental Error Sources

The experimentally measured balance load ($\boldsymbol{Y}_{exp}$) is equal to the true balance load ($\widehat{\boldsymbol{Y}}_{exp}$) combined with an experimental uncertainty ($\boldsymbol{U}_{exp}$) as shown in equation (24) or (25).

$$\boldsymbol{Y}_{exp} = \widehat{\boldsymbol{Y}}_{exp} \pm \boldsymbol{U}_{exp} \tag{24}$$

$$\begin{bmatrix} Y_{exp,NF} \\ Y_{exp,AF} \\ Y_{exp,PM} \end{bmatrix} = \begin{bmatrix} \hat{Y}_{exp,NF} \\ \hat{Y}_{exp,AF} \\ \hat{Y}_{exp,PM} \end{bmatrix} \pm \begin{bmatrix} \sqrt{U_{cal,NF}^2 + U_{PE,NF}^2} \\ \sqrt{U_{cal,AF}^2 + U_{PE,AF}^2} \\ \sqrt{U_{cal,PM}^2 + U_{PE,PM}^2} \end{bmatrix} \quad (25)$$

The experimental uncertainty is comprised of calibration uncertainty and pure error of the experiment. The calibration uncertainty was estimated during the previous calibration of the UT-36 using a manual stand system. Results for that calibration are summarized in table 26.

Table 26. Manual Stand Calibration Summary

	NF	AF	PM	RM	YM	SF
Full Scale Loads (lbs or in-lbs)	100	60	800	50	200	100
Full Scale Output (mV/V)	0.98	1.03	1.27	0.78	1.09	1.05
Sensitivities (lbs or in-lbs /mV/V)	102.34	58.52	628.37	64.52	183.04	95.24
Accuracy (lbs or in-lbs, ±2sigma)	0.04	0.04	0.32	0.15	0.16	0.06

The calibration accuracies shown in table 26 are converted to an equivalent %FSE using the VACS full scale loads (specified in table 24), resulting in the calibration uncertainties shown in table 27.

Table 27. Calibration Uncertainty for the UT-36

	$U_{cal,NF}$	$U_{cal,AF}$	$U_{cal,PM}$
(%FSE, ±2sigma)	0.133	0.200	0.266

The second error source in equation (25) is pure error. Pure error or model independent error is estimated using replicated design points and characterizes the repeatability of the calibration system. Potential causes of pure error may come from the shifting of mechanically fastened parts between runs or due to the noise of the data acquisition system. Pure error is estimated as shown

$$U_{PE} = \sqrt{\frac{\sum_{i=1}^{m}\sum_{j=1}^{n_i}\left(y_{ij} - \bar{y}_i\right)^2}{\sum_{i=1}^{m}(n_i - 1)}} \tag{26}$$

where y_{ij} denotes the jth observation in the ith set of replicates, $\bar{y}_i$ is the average of the ith set of replicates, n_i is the number of replicates in the ith set, $i = 1,2,\ldots,m$ and $j = 1,2,\ldots,n_i$. Applied to the experimentally measured balance loads, equation (26) becomes

$$U_{PE,NF} = \sqrt{\frac{\sum_{i=1}^{9}\sum_{j=1}^{2}\left(Y_{exp,NF_{ij}} - \bar{Y}_{exp,NF_i}\right)^2}{\sum_{i=1}^{9}(2-1)}} \quad . \tag{27}$$

$U_{PE,AF}$ and $U_{PE,PM}$ are computed in a similar fashion. Since the calibration experiments are fully replicated, n_i equals two for each set of replicates, resulting in nine degrees of freedom for estimation of pure error. The calculated pure error uncertainties for each system are presented in table 28.

Table 28. Pure Error Uncertainties for Both Systems

	$U_{PE,NF}$ (%FSE)	$U_{PE,AF}$ (%FSE)	$U_{PE,PM}$ (%FSE)
Centered System	0.13	0.04	0.16
Off-Center System	0.33	0.64	0.18

5.2 Physics Model Prediction Errors

The predicted physics-based loads ($\boldsymbol{Y}_{pred}$) equal the true predicted loads ($\widehat{\boldsymbol{Y}}_{pred}$) combined with an uncertainty ($\boldsymbol{U}_{pred}$) as shown in equation (28) or (29).

$$\boldsymbol{Y}_{pred} = \widehat{\boldsymbol{Y}}_{pred} \pm \boldsymbol{U}_{pred} \tag{28}$$

$$\begin{bmatrix} Y_{pred,NF} \\ Y_{pred,AF} \\ Y_{pred,PM} \end{bmatrix} = \begin{bmatrix} \hat{Y}_{pred,NF} \\ \hat{Y}_{pred,AF} \\ \hat{Y}_{pred,PM} \end{bmatrix} \pm \begin{bmatrix} U_{pred,NF} \\ U_{pred,AF} \\ U_{pred,PM} \end{bmatrix} \tag{29}$$

$\widehat{\boldsymbol{Y}}_{pred}$ is calculated using the nominal settings of the independent variables. The independent variables of the experiments are shown below.

$$\boldsymbol{X} = [\omega \quad R \quad D \quad T_x \quad L \quad \theta \quad \phi \quad \alpha \quad m] \tag{30}$$

$\boldsymbol{Y}_{pred}$ represents the loads predicted in the ideal case where the nominal settings contain zero uncertainty. In reality, the nominal settings contain uncertainty due to the methods used to measure them, resulting in the independent variable uncertainties shown in equation (31).

$$\boldsymbol{u_X} = [u_\omega \quad u_R \quad u_D \quad u_{T_x} \quad u_L \quad u_\theta \quad u_\phi \quad u_\alpha \quad u_m] \tag{31}$$

$\boldsymbol{U}_{pred}$ is estimated using the Taylor series based propagation of error analysis as presented by Coleman and Steele in equation (32).

$$U^2(y) = \sum_{i=1}^{N} \left(\frac{\partial f}{\partial x_i}\right)^2 U^2(x_i) + 2\sum_{i=1}^{N-1}\sum_{j=i+1}^{N} \frac{\partial f}{\partial x_i}\frac{\partial f}{\partial x_j} U(x_i, x_j) \tag{32}$$

In the generic form, y is a function of x_i, and $U(x_i, x_j)$ is the estimated covariance associated with x_i and x_j, while the term $\frac{\partial f}{\partial x_i}$ is often referred to as the sensitivity. For this analysis, $U(x_i, x_j)$ is assumed to be zero, resulting in the form shown in equation (33).

$$U(y) = \sqrt{\sum_{i=1}^{N} \left(\frac{\partial f}{\partial x_i}\right)^2 U^2(x_i)} \tag{33}$$

For the off-center system, equation (33) becomes

$$U_{pred,NF} = 2\sqrt{\sum_{j=1}^{9} \left(\frac{\partial NF}{\partial X_j} u_{X_j}\right)^2} \tag{34}$$

where X_j denotes the jth independent variable in $\boldsymbol{X}$. Similarly, u_{X_j} is the jth independent variable uncertainty in $\boldsymbol{u_X}$. For the centered system, an additional summation operator is required to sum the uncertainties due to the individuals arms, as shown in equation (35).

$$U_{pred\ ,NF} = 2\sqrt{\sum_{i=1}^{6}\sum_{j=1}^{9}\left(\frac{\partial NF_i}{\partial X_j}u_{X_j}\right)^2} \tag{35}$$

$U_{pred\ ,AF}$ and $U_{pred\ ,PM}$ are calculated similarly to $U_{pred\ ,NF}$ for each system. In equation (35), i is the index for the arm number, where $i = 1,2 \ldots 6$. NF_i represents the normal force physics based equation for the ith arm of the centered system. Each equation is multiplied by two, which is an estimate of the t-statistic, to provide a coverage factor for 95% confidence. The partial derivative term is estimated at the nominal independent variable settings, which vary between runs, while the independent variable uncertainties remain constant and are shown in table 29.

Table 29. Independent Variable Uncertainties

Variable	Uncertainty	Units
u_ω	0.001	rev/s
u_R	0.01	in
u_D	0.01	in
u_{T_x}	0.01	in
u_L	0.01	in
u_θ	0.08	deg
u_φ	0.05	deg
u_α	0.001	deg
u_m	0.001	lbs

The independent variable uncertainties reflect the uncertainty of the instruments and methods used to estimate the independent variables. The rotational velocity uncertainty (u_ω) was provided by the table's manufacturer specifications. The length uncertainties (u_R, u_D, u_{T_x}, u_L) represent a combination of the precision of the vernier calipers used to take the measurements and the associated human error. The misalignment angle uncertainty between the table rotational axis and gravitational axis (u_α) reflects the accuracy of the accelerometer package that was used to level the rotating table in the lab. The balance deflection uncertainty (u_θ) was estimated as half of the maximum balance deflection angle experienced during the calibration experiment which was calculated using the deflection constants acquired from a previous calibration of the UT36. The arm deflection angle uncertainty (u_φ) reflects fabrication error and the potential for the arms to deflect under load, which was investigated using finite element analysis and is discussed in appendix J. The applied weight error (u_m) is representative of the calibrated weights used in the experiments.

Figure 24 and figure 25 show the propagated prediction error for each system. The bar lengths represent the total force component uncertainty calculated using equation (34) or (35), while the subdivisions within each bar represent the percent contribution of each independent variable uncertainty.

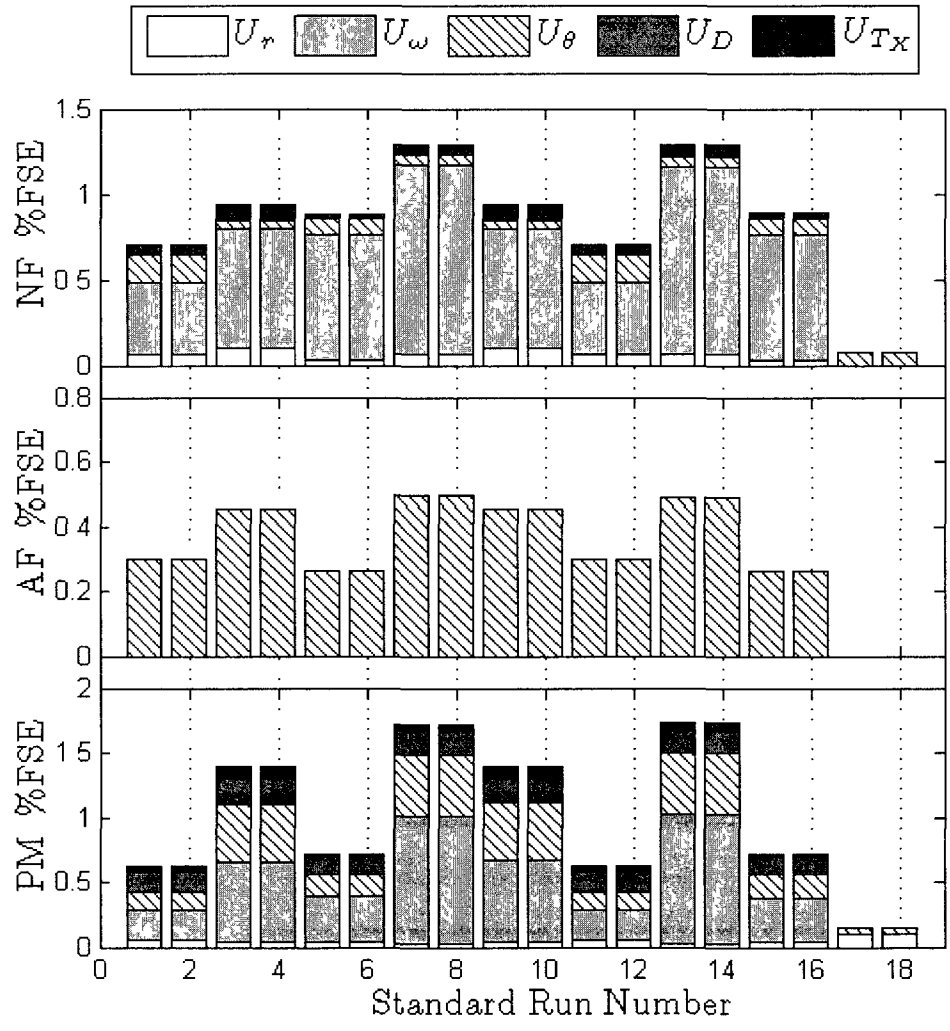

Figure 24. Centered System Propagated Prediction Error (Factorial Block)

For the centered system, it can be seen that the rotational velocity uncertainty has the greatest effect on normal force. Standard runs 17 and 18 are center points runs that

load the balance while at rest; therefore, angular velocity error effects are irrelevant. Balance deflection angle dominates the axial force load uncertainty since axial loads are applied predominately using gravity. Pitching moment uncertainty is the largest since the pitching moment uncertainty is dependent on the normal force and axial force uncertainty. Standard runs 7-8 and 13-14 have the largest uncertainties due to an increased attached weight and angular speed.

For the off-center system, angular velocity uncertainty effects are prevalent in all three force components. Balance deflection angle uncertainty is more pronounced in normal and axial force error, while moment arm distant uncertainty contributes largely to the pitching moment error. The center runs apply zero load; therefore, no applied load error is possible, as shown in standard runs 17 and 18.

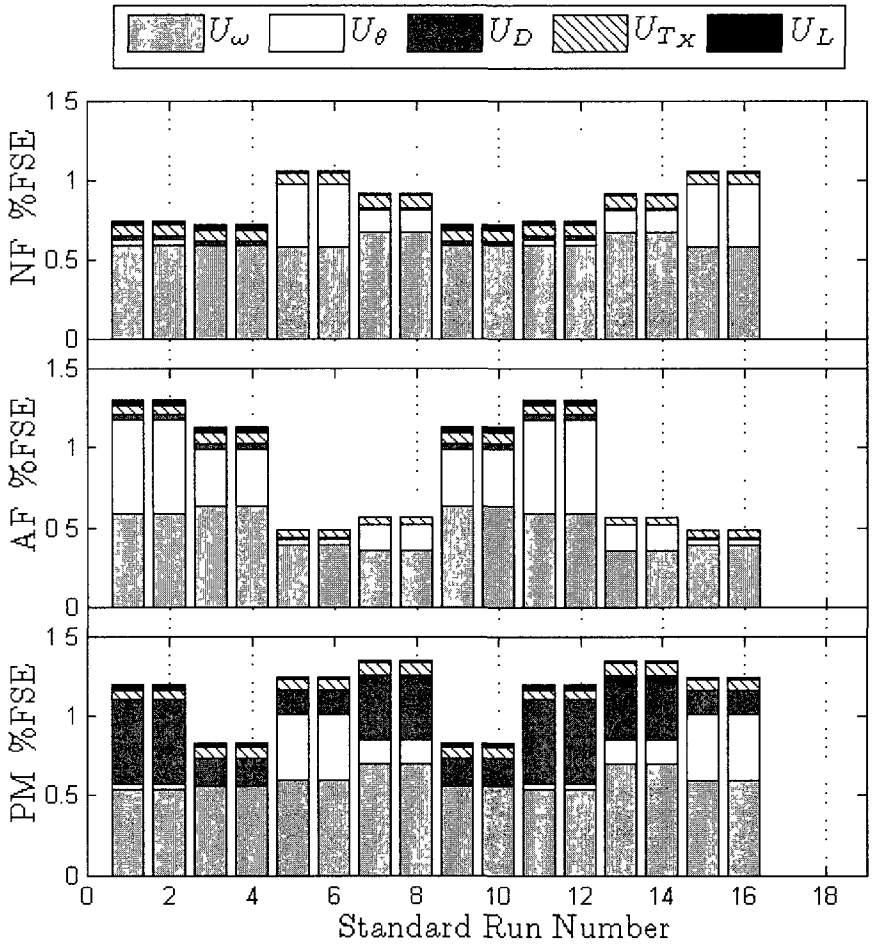

Figure 25. Off-Center System Propagated Prediction Error (Factorial Block)

5.3 Summary of Error sources

Let the total uncertainty in the calculation of applied load error ($\boldsymbol{U_E}$) be the root summed square of the individual sources of uncertainties, as shown in equation (36).

$$\boldsymbol{U_E} = \begin{bmatrix} U_{E,NF} \\ U_{E,AF} \\ U_{E,PM} \end{bmatrix} = \begin{bmatrix} \sqrt{U_{cal,NF}^2 + U_{PE,NF}^2 + U_{B,NF}^2} \\ \sqrt{U_{cal,AF}^2 + U_{PE,AF}^2 + U_{B,AF}^2} \\ \sqrt{U_{cal,PM}^2 + U_{PE,PM}^2 + U_{B,PM}^2} \end{bmatrix} \quad (36)$$

$\boldsymbol{U_E}$ is the total uncertainty in the calculation of applied load error, where the applied load error equals the true error plus or minus the total uncertainty, as shown in equation (37).

$$\boldsymbol{E} = \widehat{\boldsymbol{E}} \pm \boldsymbol{U_E} \quad (37)$$

Figure 26 and figure 27 summarized the contributions of the total uncertainty for each run in the calibration experiments, where the bar length represents the magnitude of the total uncertainty. The components within each bar represent the percent contribution of the individual sources of uncertainty.

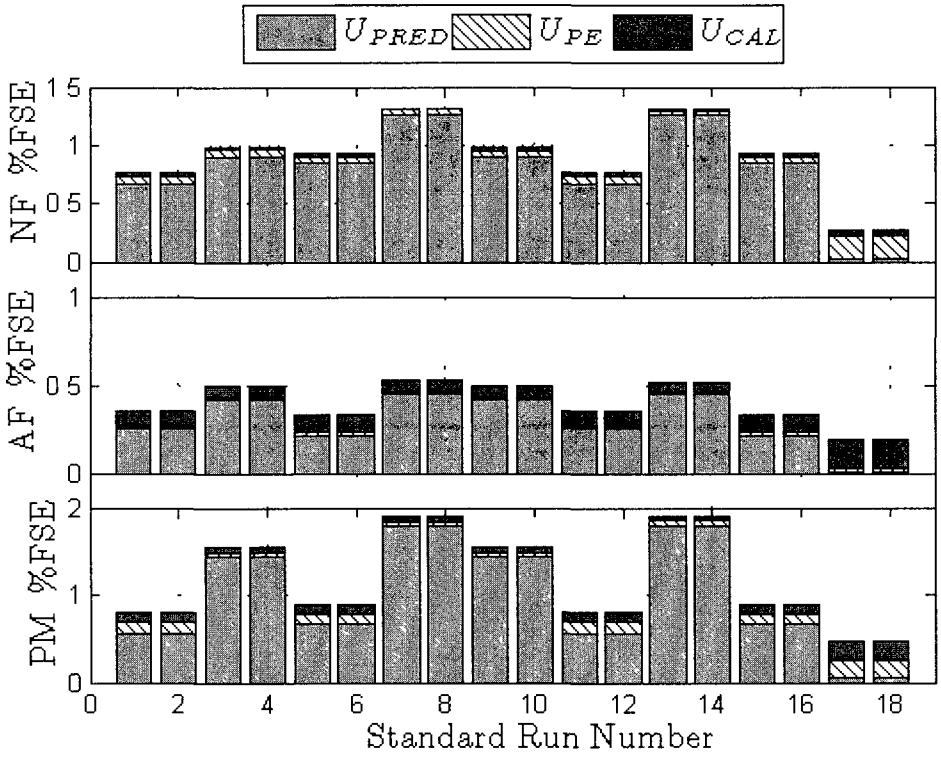

Figure 26. Centered System Total Error (Factorial Block)

In the centered system, the prediction uncertainty dominates over the pure error and calibration uncertainties. This is also true for the off-center system except for axial force, where pure error plays a more important role. Potential causes of pure error may have come from the shifting of mechanically fastened parts between runs or due to the noise of the data acquisition system. The centered system exhibits less pure error because there were no major hardware configuration changes made throughout the experiment besides replacing weights on the arms. In contrast, the off center system hardware changes involve removing the angled wedge blocks as well as the balance taper adapter and weights.

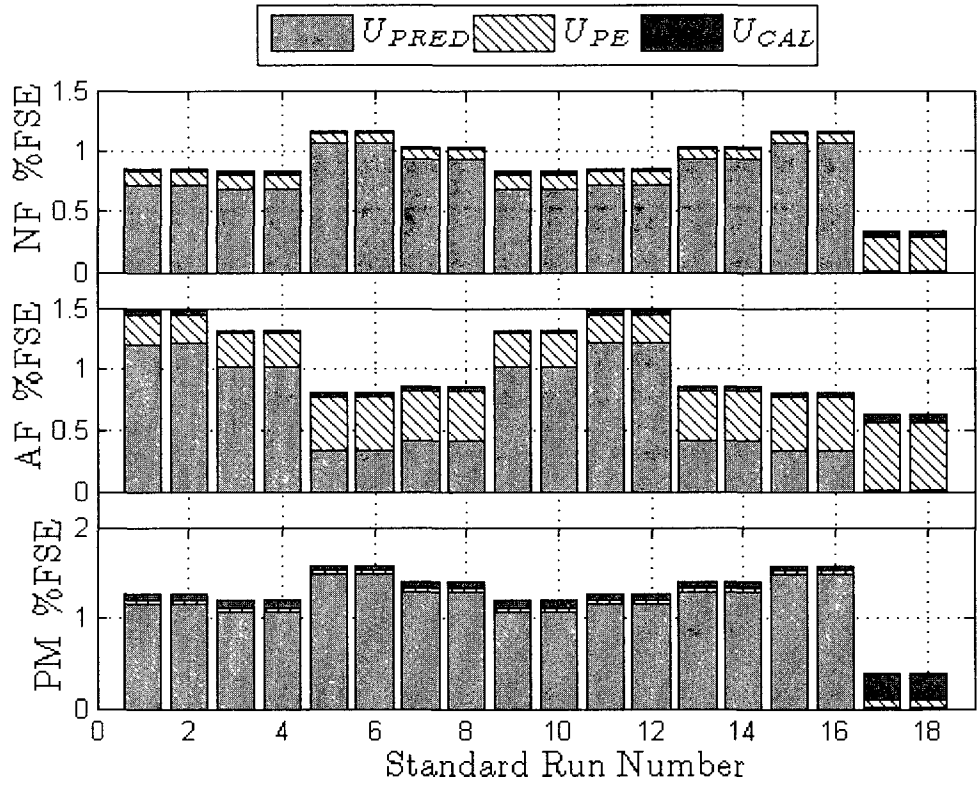

Figure 27. Off-Center System Total Error (Factorial Block)

The fact that pure error is much smaller than prediction error indicates that each system has the potential for improvement. The small amount of pure error indicates that the measurements are quite repeatable, but the independent variable settings are not precisely known. With better means of measuring the independent variables, the calibration systems could reduce the total uncertainty down to the pure error level via calibration. Pure error could be reduced by redesigning the system so that fewer hardware changes are required.

5.4 Applied Load Verification

As previously stated, the primary objective of the uncertainty analysis is to verify that the applied load error is within the uncertainty intervals predicted for each system. The equation for applied load uncertainty is restated below in equation (38),

$$\boldsymbol{E} = \widehat{\boldsymbol{E}} \pm \boldsymbol{U}_E \tag{38}$$

where the true applied load error ($\widehat{\boldsymbol{E}}$) is the difference between the true experimentally measured loads and the true predicted loads, as shown in equation (39). The true experimentally measured load represents the ideal case where the measurement contains zero uncertainty. Similarly, the true predicted load represents an ideal case where the estimates of independent variables in the physics-based models contain zero uncertainty. The true experimentally measured loads and the true predicted loads represent the actual force applied to the balance; therefore, the difference between them is zero.

$$\widehat{\boldsymbol{E}} = \widehat{\boldsymbol{Y}}_{exp} - \widehat{\boldsymbol{Y}}_{pred} = \mathbf{0} \tag{39}$$

Inserting this result in equation (38), we have

$$\boldsymbol{E} = \pm \boldsymbol{U}_E \quad . \tag{40}$$

Equation (38) implies that 95% of the applied load error samples should fall within the total uncertainty interval since the total uncertainty represents a 95% confidence interval.

To verify this assertion, the applied load errors are plotted with the total uncertainty intervals for each run in the calibration experiments, as shown in figure 28 and figure 29.

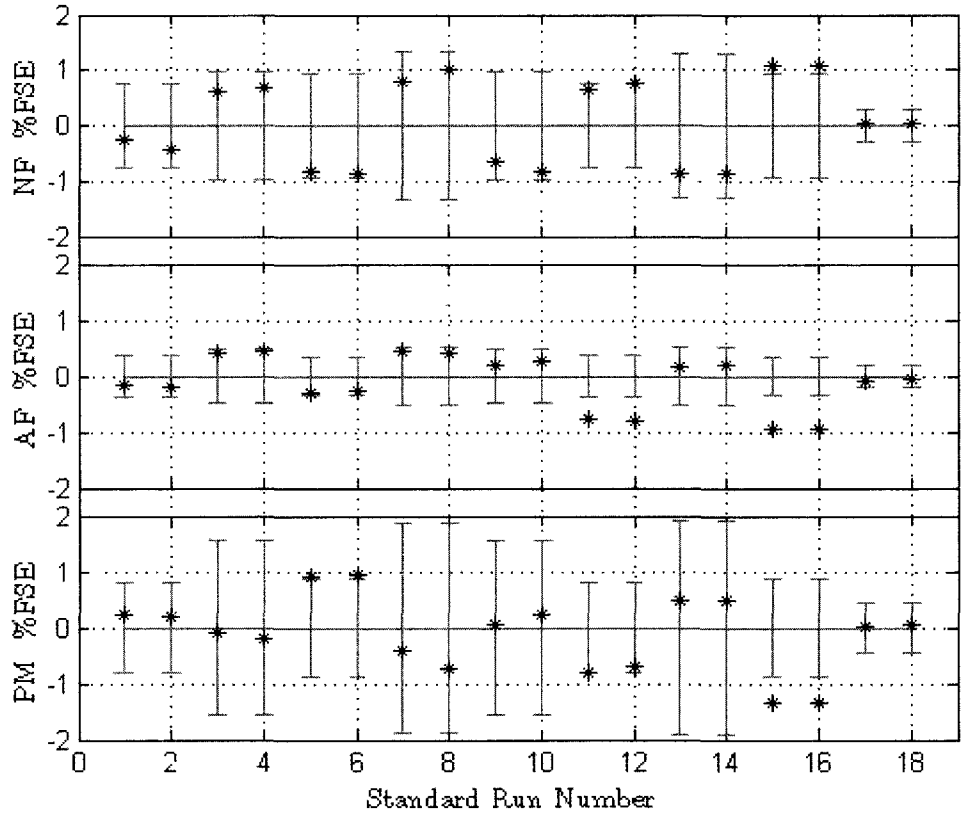

Figure 28. Centered System Applied Load Error with Total Uncertainty Intervals

The start points represent the applied load error, while the gray bars represent the total uncertainty interval.

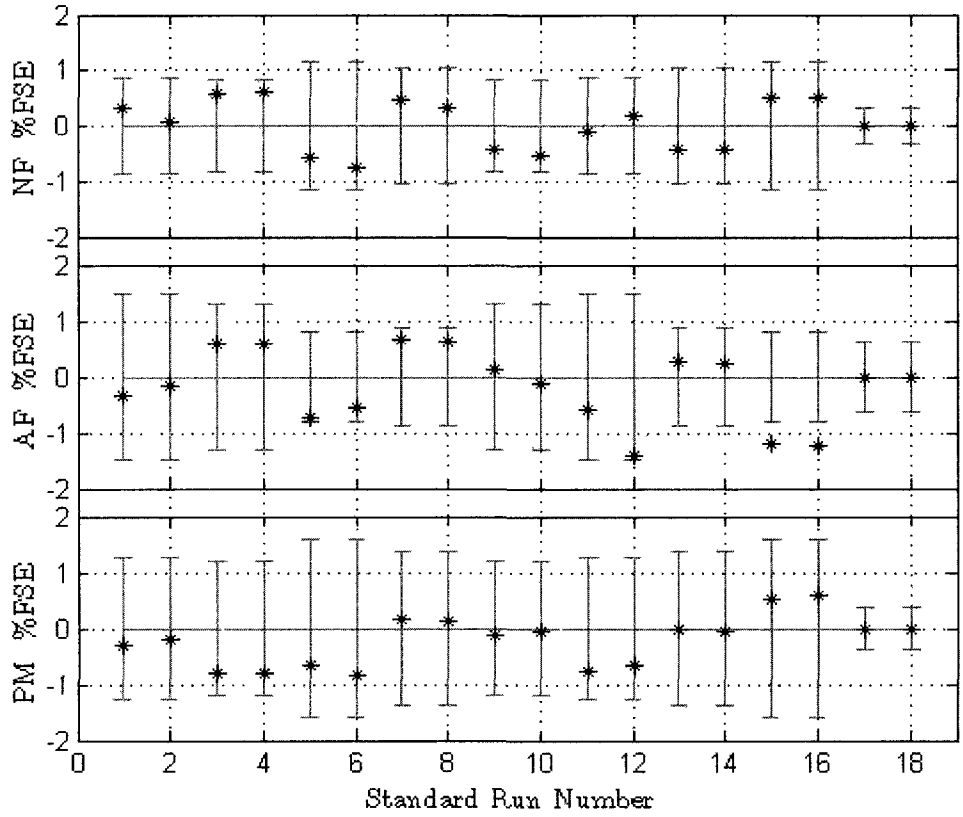

Figure 29. Off-Center System Applied Load Error with Total Uncertainty Intervals

The primary objective was to verify that the applied load errors were within the total uncertainty intervals. For the centered system, 46 out of 54 (≈80%) applied load error samples were within the total uncertainty intervals, while for the off-center system, 52 out of 54 (≈96%) samples fell within the interval. To investigate potential causes of error, the applied load error residuals are examined.

5.5 Centered System Residuals

Typically, residual analyses investigate model error estimates to test model assumptions, using data from the experiment. For example, normality, independence

and constant variance are tested after a model has been fit to the data to ensure the statistical hypotheses have been upheld. For the VACS calibration experiments, a residual analysis is used in a different manner since a model is not being fit to the data. In this section, tests for non-constant variance and dispersion are investigated to indentify faults in the mechanical components of each variable acceleration system. Plots of applied load error versus experimental factors are used to check for non-constant variance. Plots of pure error versus experimental factors are used to check for dispersion.

Figure 30 shows no correlation between rotational velocity and applied load error.

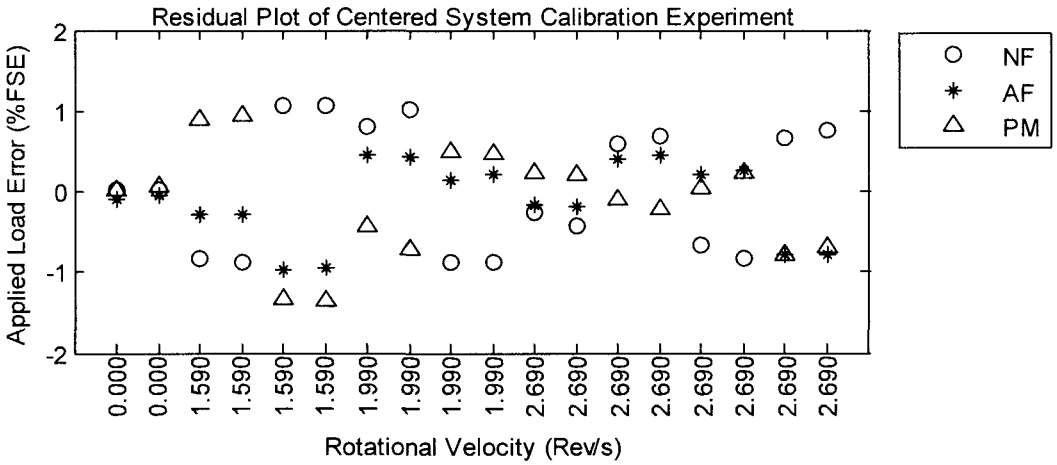

Figure 30. Centered System Rotational Velocity vs. Applied Load Error

Figure 31 shows the applied load error plotted against deflection angle of the balance. The centered system positions the balance vertically (zero angle), so the angle plotted in figure 31 is the deflection angle due to the applied load. It should be remembered that deflection angle is calculated using the deflection constants obtained during a previous manual stand calibration of the UT-36. In figure 31, it is clear that the applied load error

increases as the magnitude of the computed deflection angle increases. This demonstrates a clear problem with the angle deflection calculation method.

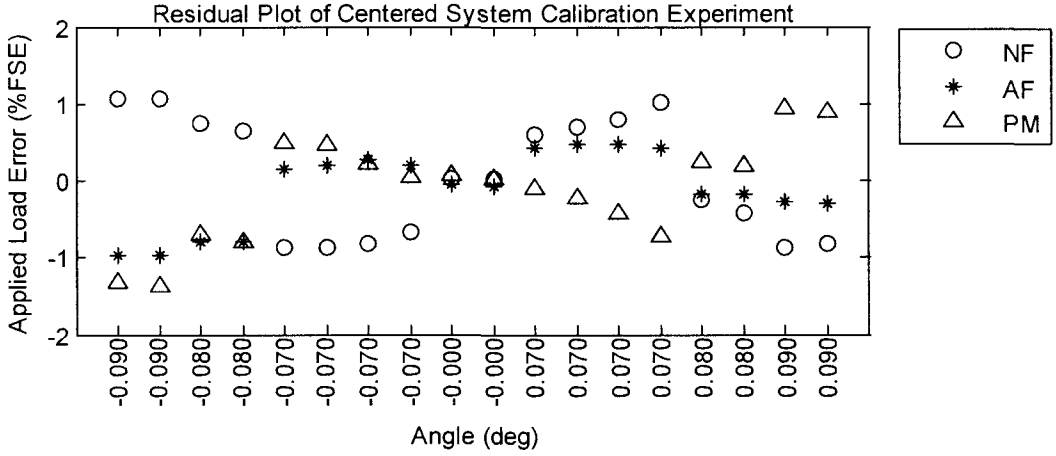

Figure 31. Centered System Deflection Angle vs. Applied Load Error

Figure 32 shows fairly scattered data, meaning pure error may not be directly correlated with deflection angle.

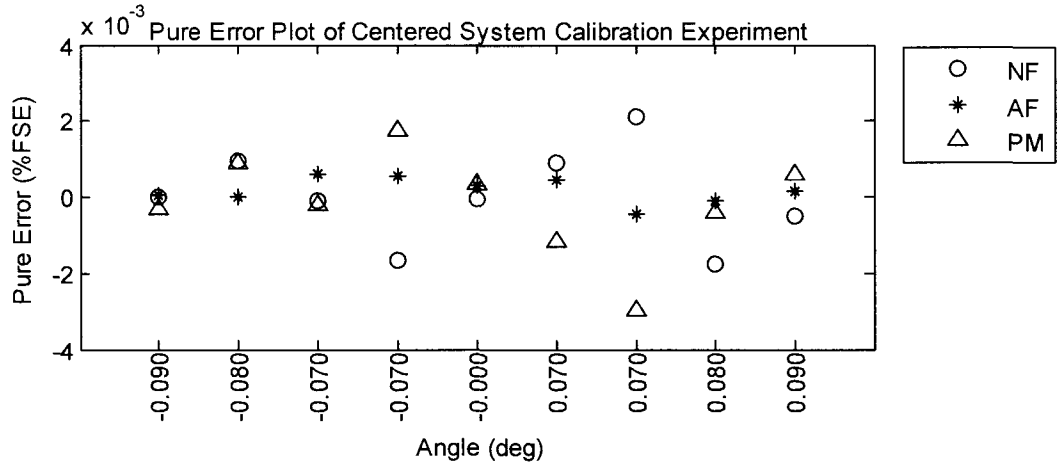

Figure 32. Centered System Deflection Angle vs. Pure Error

In figure 33, normal force applied load error shows a strong correlation with normal force load. Pitching moment applied load error also shows a correlation with normal force load.

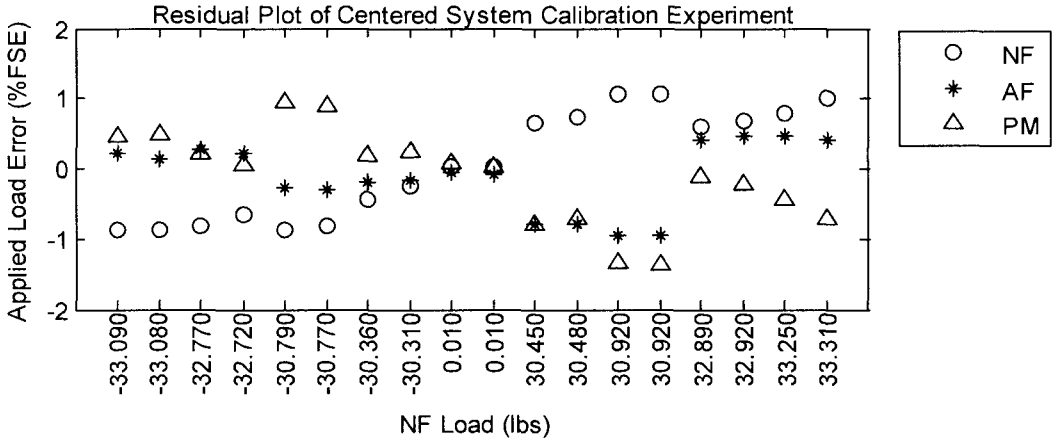

Figure 33. Centered System Normal Force vs. Applied Load Error

Figure 34 shows a slight trend of an increase in pure error as normal force load magnitude increases.

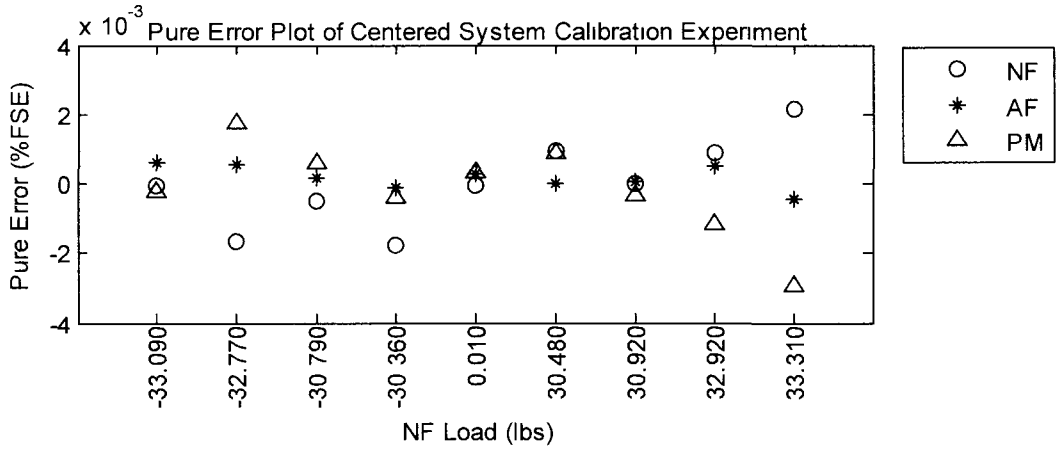

Figure 34. Centered System Normal Force vs. Pure Error

The effect of axial force load is inconsequential to the applied load error as seen in figure 35.

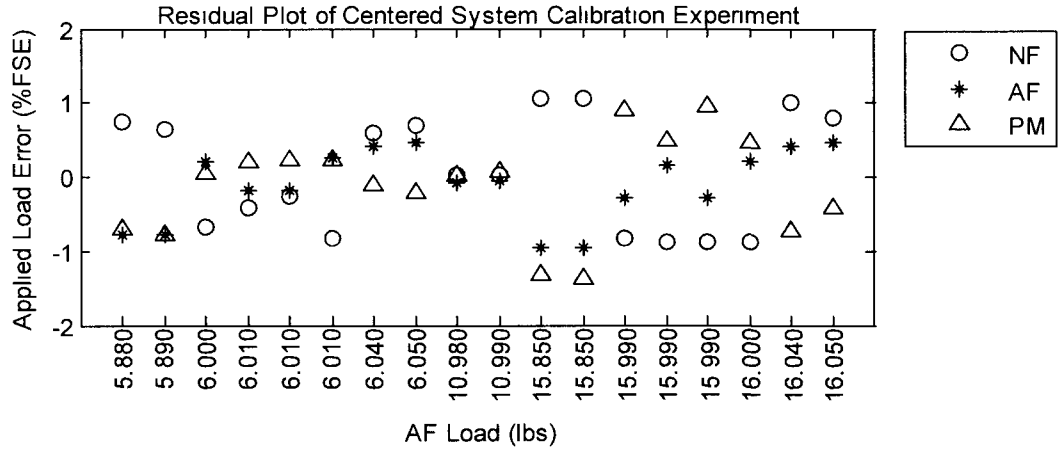

Figure 35. Centered System Axial Force vs. Applied Load Error

Similar to the NF load versus applied load error plot, figure 36 also shows strong correlations.

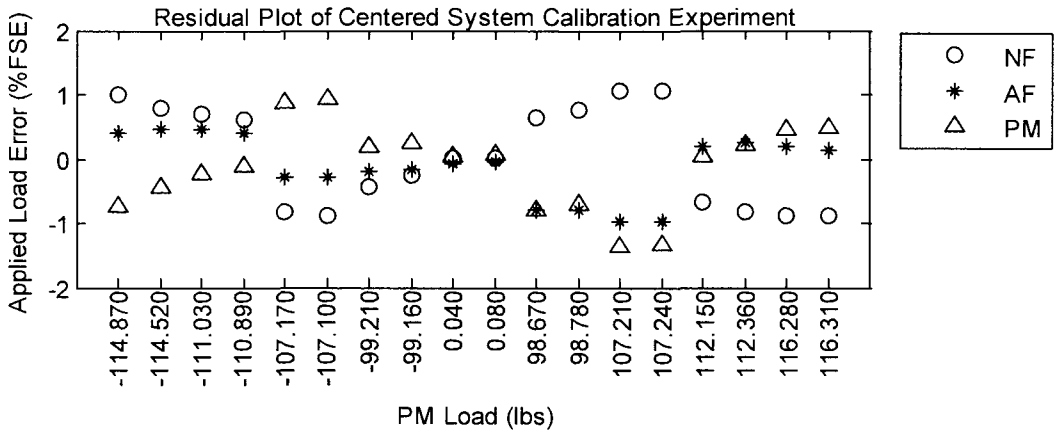

Figure 36. Centered System Pitching Moment vs. Applied Load Error

Figure 37 shows that pure error is somewhat correlated with applied pitching moment for the centered system.

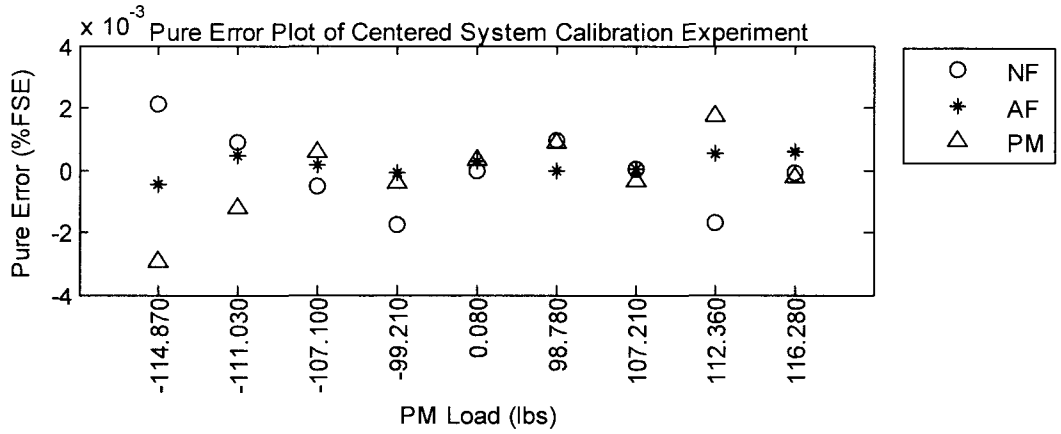

Figure 37. Centered System Pitching Moment vs. Pure Error

5.6 Off-Center System Residuals

The off-center system uses two wedge blocks that each have a particular value of *L*, which specifies the distance from the balance moment center to the table surface. In figure 38, it appears that neither wedge causes an increase in applied load error compared to the other.

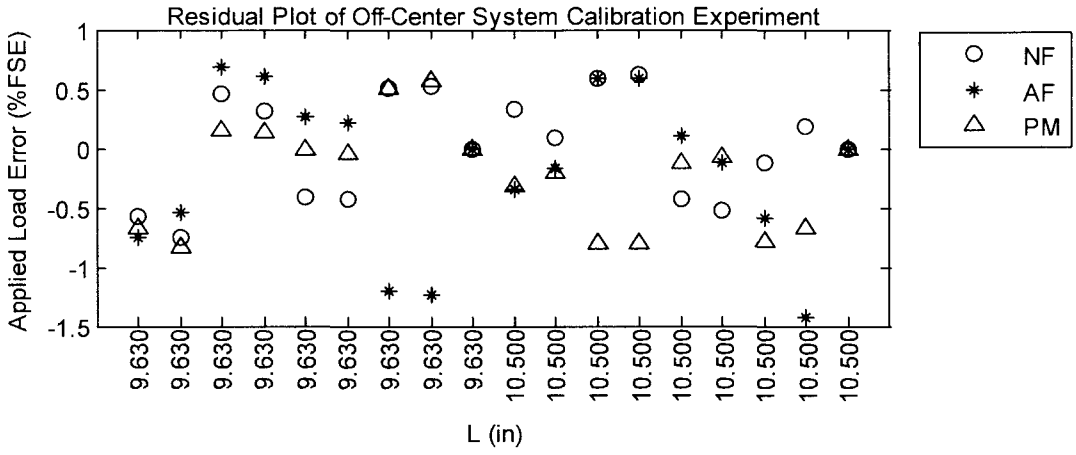

Figure 38. Off-Center System L distance vs. Applied Load Error

In figure 39, it appears that no strong correlation exists. This contradicts the center system result which showed a strong correlation between applied load error and calculated deflection angle.

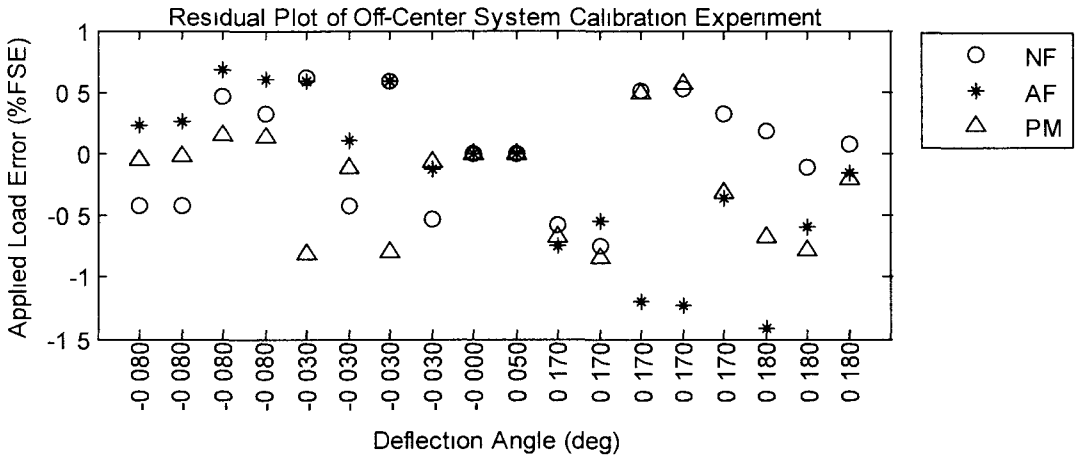

Figure 39. Off-Center System Deflection Angle vs. Applied Load Error

Figure 40 plots the applied load error versus total angle. The total angle is the wedge angle summed with the calculated deflection angle.

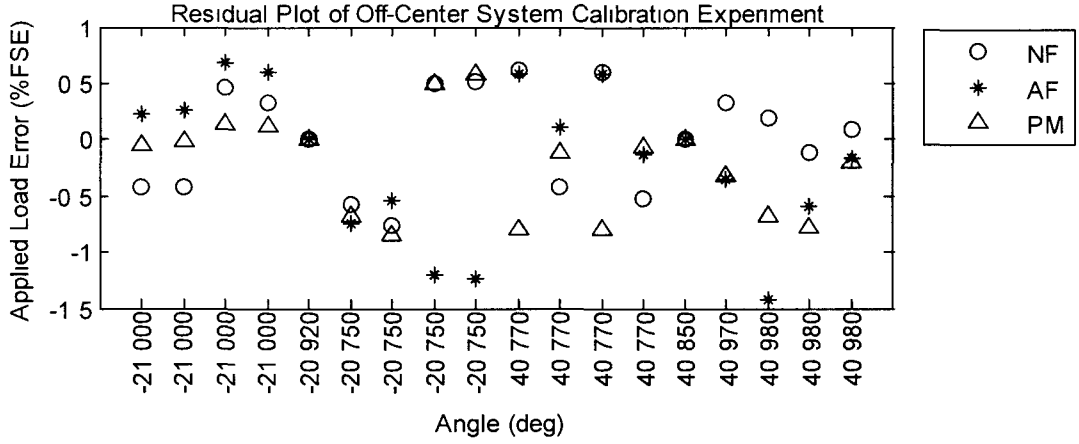

Figure 40. Off-Center System Total Angle vs. Applied Load Error

Additional residual plots for both the off-center and centered system are shown in appendix K.

6 DISCUSSION

Not all applied load error observations fell within the predicted total uncertainty intervals. These outliers suggest that unidentified error sources were present during the calibration experiments. To examine this possibility, potential additional causes of error are discussed.

Firstly, it is possible that the outliers are due to chance. The center system displayed an 80% capture rate, while the off-center system had a 96% capture rate. An additional experiment for the centered system, detailed in appendix L, showed a 100% capture rate. The total uncertainty intervals were constructed based on 95% confidence. With more observations, it could be possible that the capture rate would rise above the 95% threshold. If the intervals were based on a 99% (3σ) confidence, then all applied load error observations would have fallen in the interval.

There are several reasons why the centered system did not perform as expected. First of all, the centered system contains several more independent variables than the off-center system. This required several additional measurements to determine the nominal independent variables settings and the corresponding uncertainties, which increases the risk of human error. Also, the centered system used almost all originally fabricated parts, while the off-center system borrowed components from other calibration hardware. The original parts were fabricated with limited resources; therefore, quality assurance was limited. On the other hand, the pre-existing parts were fabricated within very tight tolerances, which greatly helped the off-center system.

A major assumption in the governing equations was that all loads were applied in one plane, meaning that it was a two-dimensional problem. This assumption was made

for simplifying purposes; however, loads out of plane, such as rolling moment, yawing moment, and side force, may have had an effect. Table 30 shows the mean and two-sigma standard deviation for the out of plane loads for each system's calibration experiment. These are delta loads, meaning the tare load has been subtracted from the total load.

Table 30. Summary of Out of Plane Loads

Centered System Factorial Experiment			
	RM (in-lbs)	YM (lbs)	SF (in-lbs)
Mean	-0.05	-0.24	-0.03
2σ	0.20	0.31	0.12
Centered System Augmented Experiment			
	RM (in-lbs)	YM (lbs)	SF (in-lbs)
Mean	-0.03	-0.28	-0.04
2σ	0.17	0.64	0.09
Off-Center System Factorial Experiment			
	RM (in-lbs)	YM (lbs)	SF (in-lbs)
Mean	0.02	-0.02	-0.04
2σ	0.09	1.72	0.46

The center system shows smaller out of plane loads than the off-center system. Since these are loads measured using the UT-36 and the previously acquired calibration coefficients, it is possible that these loads are due to error in the calibration model, caused by poorly estimated interaction effects. Since these are delta loads, it reasonable to assume that most of the aerodynamic effects have been tared out. As described in the tare section, the tare is run at the same angular velocity as the calibration run; therefore, most aerodynamic effects due to the balance and fixtures have been removed. The exception is that the added volume and surface area from the attached weight during the

calibration run could cause an aerodynamic load that is not tared out. Using the simple drag equation, the expected drag caused by an added mass for a particular run of the centered system is calculated using equation (41).

$$D = \frac{1}{2}\rho V^2 S C_D \tag{41}$$

The assumed drag coefficient of the attached mass is one. The calculated frontal surface area for a two pound, one pound and half pound attached weight is 3.5 in^2, 1.75 in^2, and 1 in^2 respectively. The drag, acting in the side force load direction, is calculated for each run in the centered system experiment. It is assumed the velocity can be calculated by multiplying the angular velocity with the arm radius. This analysis also assumes the attached weight is in a uniform free stream, where the free stream direction seen by arms one, two, and three is in the opposing direction of the free stream seen by arms four, five, and six. A case where an equal amount of weight is attached on opposing sides negates sides force. Table 31 compares the balance measured side force with the side force calculated using the simple drag equation for each run in the centered system calibration experiment.

Table 31. Centered System Side Force

Std Run#	Measured (lbs)	Calculated (lbs)
1	-0.03	0.01
2	-0.03	0.01
3	-0.03	-0.01
4	-0.03	-0.01
5	0.00	0.01
6	0.00	0.01
7	-0.11	-0.01
8	-0.12	-0.01
9	0.07	0.01
10	0.07	0.01
11	-0.08	-0.01
12	-0.08	-0.01
13	0.06	0.01
14	0.07	0.01
15	-0.09	-0.01
16	-0.08	-0.01

In table 31, the polarity of the calculated drag relates closely to the polarity of the measured force although the magnitudes are dissimilar. This indicates that drag may indeed have an effect that is not tared out. Discrepancies in magnitudes can be attributed to the over simplification of the aerodynamics problem setup.

To remove the aerodynamic forces applied to the balance, the following solutions are proposed. The system could be placed in a vacuum or low-density gas chamber. This approach is used by spin tables used to measure inertia properties of rigid bodies. The more practical approach may be to simply cover the balance, fixture and attached mass in a shroud. The shroud would be fixed to the table and should mold as closely to the balance as possible. By fixing the shroud to the table, the balance would be shielded from the aerodynamic loads imparted on the shroud. Minimizing the volume of air

between the shroud and balance would limit the aerodynamic effects of the air within the shroud.

The next potential cause of error could come from the previous calibration of the UT-36. This calibration was performed in 1995. There is usually no reason to believe a balance has gone out of calibration unless it has been damaged; however, a history of use for this balance is non-existent, so a recalibration may have been required. Unfortunately, the funds for this recalibration were not available. Furthermore, the balance was designed and calibrated for larger loads than what were applied during the VACS calibration experiments, meaning that the balance is less sensitive and therefore less accurate in the lower load range.

Another unaccounted for error source could be due to the dynamic loading of the balance during calibration runs. The governing equations assume the balance is rigidly fixed to the table during rotation. This assumption means that the balance is statically loaded, and it experiences negligible vibration. Due to the inadequate sampling frequency of the Agilent meters used for the calibration experiments, a different data acquisition system is used to take data to investigate the validity the of static loading assumption. A National Instruments PXI-4462 data acquisition module is used because it has quick and accurate sampling characteristics, as shown in table 32.

Table 32. National Instruments PXI-4462 Specifications

Bus	PXI, PCI
Analog Inputs	4
Input Resolution	24 bits
Sampling Rate	204.8 kS/s
Input Range	±316mV to 42.4 V

Three centered system runs are investigated with varying rotational speeds and 6 lbs loaded on arm two. 300,000 samples are collected in each run at a sampling rate of 10 kHz, giving 30 seconds of data. For the first run, figure 41 shows a time series of data, while the table is at rest. The vertical axis shows the UT-36 balance output in units of mV/5V.

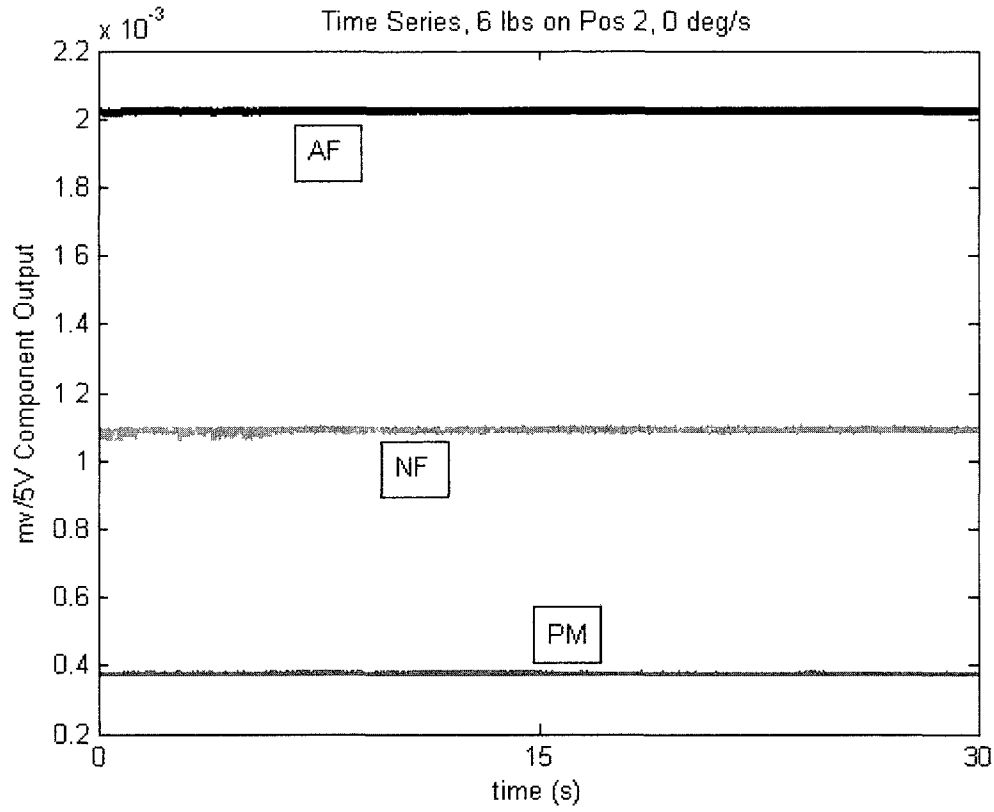

Figure 41. Centered System Time Series, No Rotation

Figure 42 shows an auto power spectrum corresponding to the time series data shown in figure 41. While the table is at rest, we see the noise is dominated by alternating current 60 Hz noise and multiples thereof.

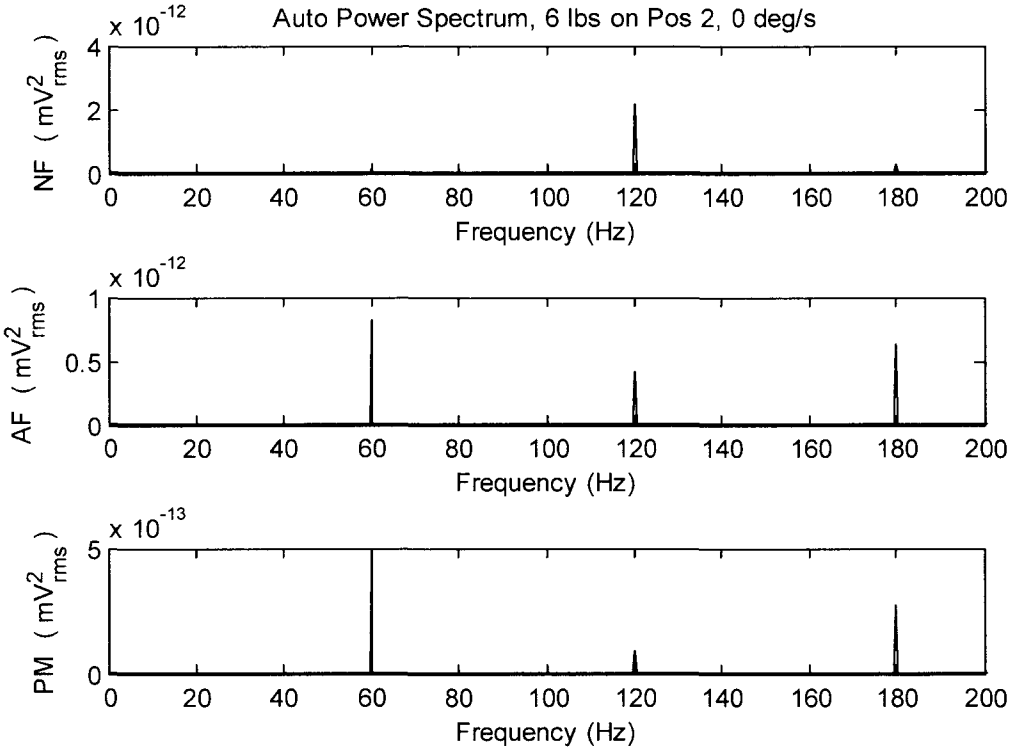

Figure 42. Centered System Auto Power Spectrum, No Rotation

At a low rotation rate, figure 43 shows that the amplitude of the axial force component becomes quite large compared to when the table was at rest. The normal force amplitude increases modestly while the pitching moment amplitude increases the least.

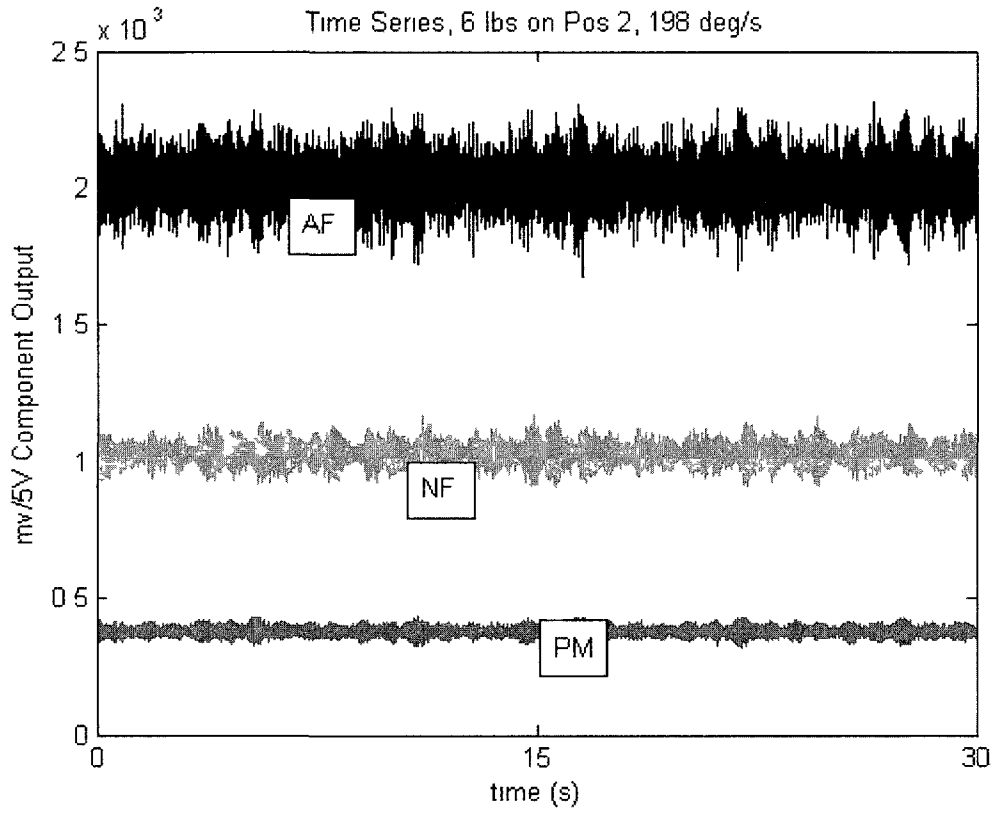

Figure 43. Centered System Time Series, 198 deg/s Rotation

The corresponding auto power spectrum for this case shows that the dominant frequency is no longer 60 Hz or a multiple, as seen in figure 44. The new dominant frequency is about 82 Hz. This implies that vibration of either the table or the balance is affecting the balance output.

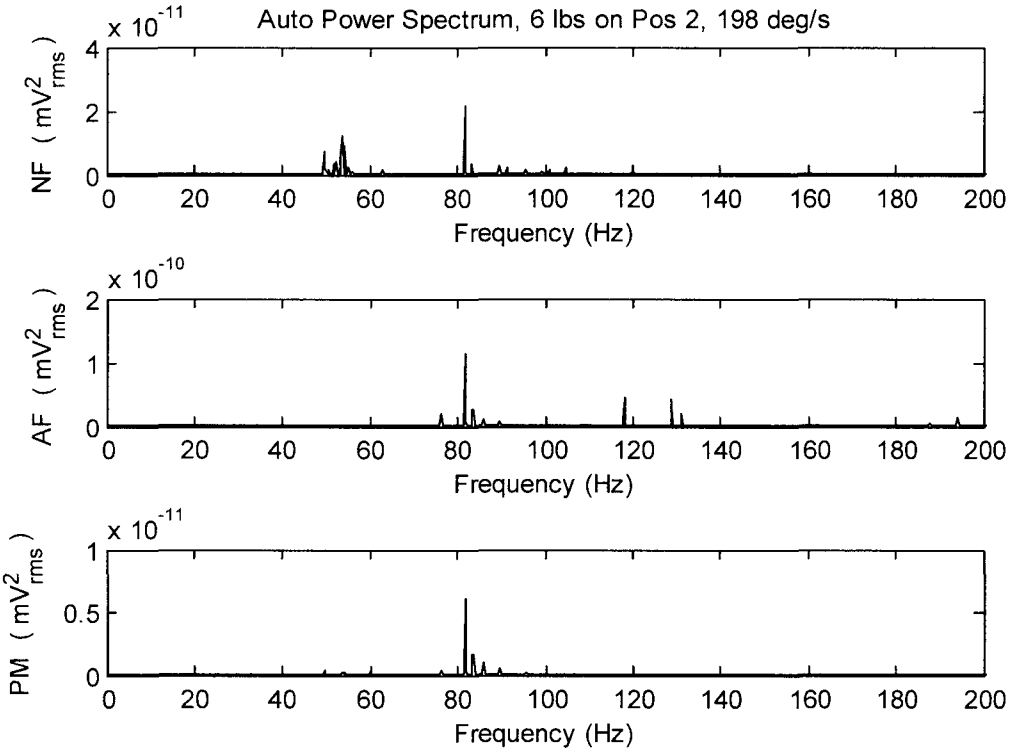

Figure 44. Centered System Auto Power Spectrum, 198 deg/s Rotation

As the table speed increase further, the component amplitudes become even larger, especially for axial force, as shown in figure 45. The peak to peak amplitude of the axial force output is slightly larger than 1 mV/5V. Since the axial force component has a sensitivity of about 58 lbs/mV/V, the peak to peak axial force amplitude is approximately equal to 11 lbs, which accounts for about 18% of the full scale load.

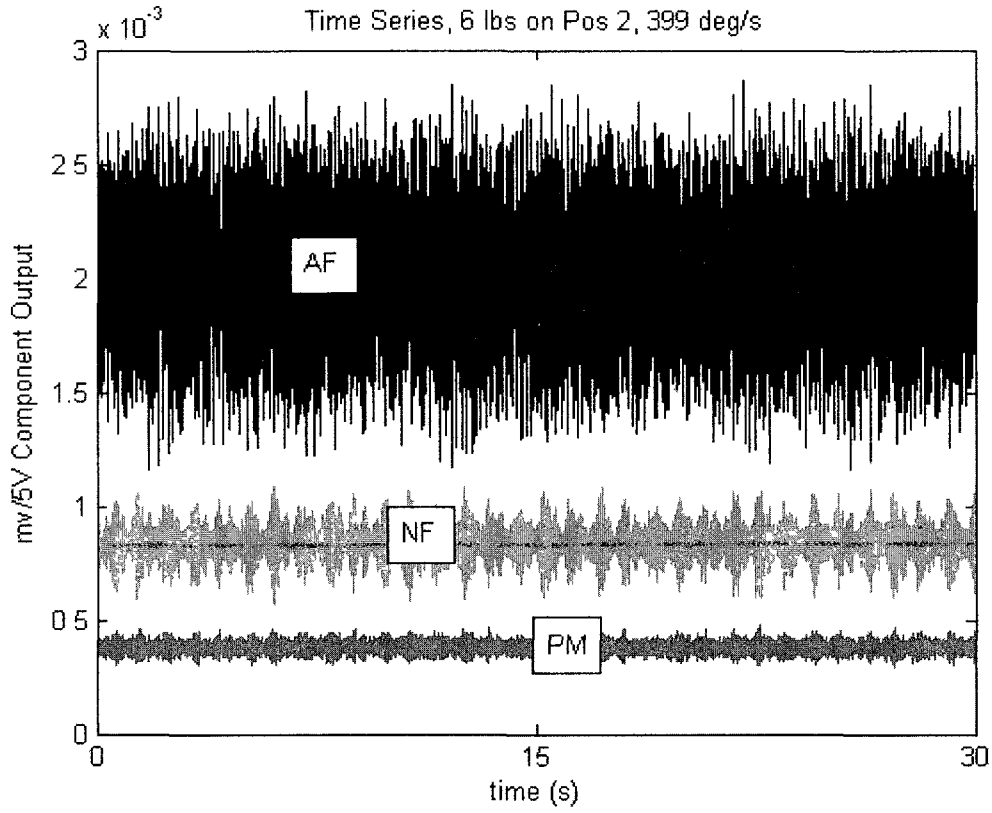

Figure 45. Centered System Time Series, 399 deg/s Rotation

The spectral components of this case are similar to before. The 82 Hz frequency is once again dominant, but now other higher frequencies are also significant. The normal force and pitching moment outputs display similar spectral qualities, which is expected, since the components are gauged in the same cage section on the balance.

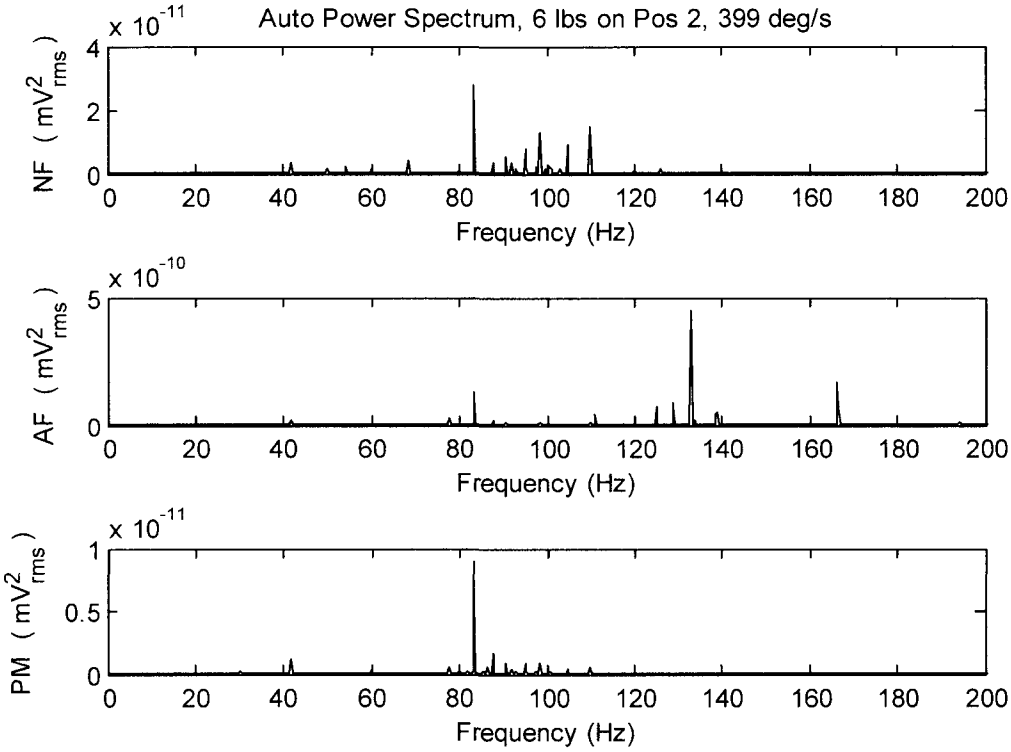

Figure 46. Centered System Auto Power Spectrum, 399 deg/s Rotation

While the balance is at rest, 60 Hz noise dominates; however, while the table is spinning, the balance flexure vibration modes become pronounced. The large amplitude of the axial force component may be a cause for balance safety concern since the axial force component could be unintentionally overloaded during calibration. The dynamic nature of the calibration loads could be beneficial since the loads experienced in a wind tunnel are also dynamic. This could provide researchers with more information about balance output behavior than what is typically provided by static calibrations. This could lead to improved dynamic loads estimated during wind tunnel tests.

A final error source contributing to applied load error outliers is due to the method used to calculated balance deflection angle. The deflection angle was approximated

using the deflection constants acquired from the previous calibration of the UT-36. It was assumed the balance deflection was linear, when in reality the balance probably deflected like a cantilevered beam. The uncertainty of using the deflections constants method was roughly approximated as half of the maximum calculated deflection angle. This approximation is not traceable back to any standard and should not be used in future systems. It was also shown that a multi-axis accelerometer package is ineffective at measuring deflection angles due to the coupling of the acceleration components. Two alternative methods to measure balance deflection angle could be to use photogrammetry, or gyroscopes. The photogrammetry method would use multiple high resolution video cameras to determine the location of reflective targets placed on the balance. The photogrammetry system would be fixed to the ground and would track the targets, on the balance, from a fixed frame. An advantage of a photogrammetric system is that it is non-intrusive. The disadvantage is cost. Alternatively, a gyroscope could be used. The gyro rate output could be integrated to provide an angle. The uncertainty of the resultant angle is dominated by the angular random walk (ARW) specification provided by the gyroscope manufacturer. The angular random walk uncertainty is proportional to the square root of time; therefore, the duration of the VACS calibration run should not be too long. The angular random walk specification for numerous gyroscopes is provided in table 33. These are commercial grade instruments that are not too expensive.

Table 33. ARW of Various Gyroscopes

Gyroscope	ARW $\left(\frac{deg}{\sqrt{sec}}\right)$	ARW $\left(\frac{deg}{\sqrt{hr}}\right)$
ADXRS623	0.040	2.400
ADIS16334	0.033	2.000
MEMSENSE nano-IMU	0.070	4.200
Sensonar SAR150	0.013	0.800
Sensonar SAR100	0.030	1.800
Sensonar STIM202	0.003	0.200
KVH-5000	0.001	0.083

Equation (42) is used to calculate the standard error of an angle measured using the KVH-5000 gyroscope. It is assumed the duration of the calibration run is fifteen seconds.

$$\sigma_\theta = 0.001 \frac{deg}{\sqrt{sec}} \times \sqrt{15 sec} \approx \pm 0.004\ deg \tag{42}$$

Additional potential of the VACS can be realized by measurement or knowledge of the independent variable uncertainties used in the propagation of error analysis. As previously shown, the uncertainties were defined by the quality of the proof-of-concept system. A future production system requires a superior applied load error, which should be less than 0.05% FSE if it is to have comparable performance to existing systems. Table 34 presents the independent variable uncertainties required for such a system. These uncertainties represent expensive, yet achievable accuracy by today's standards. The propagation of error analysis was repeated using the improved uncertainties shown in Table 34. The predicted applied load error (U_{pred}) was computed for each run in the calibration experiment for each system.

Table 34. Ideal Independent Variable Uncertainties

Variable	Uncertainty	Units
u_ω	0.0001	rev/s
u_R	0.0001	in
u_D	0.0001	in
u_{T_x}	0.0001	in
u_L	0.0001	in
u_θ	0.0040	deg
u_φ	0.0040	deg
u_α	0.0005	deg
u_m	0.0005	lbs

The angular velocity uncertainty, length dimensions uncertainty and mass uncertainty are expensive, yet attainable by today's standards. The arm deflection uncertainty and balance deflection uncertainty reflect the values calculated for the KVH-5000 gyroscope. Table 35 shows the resultant predicted applied load error averaged over each experiment.

Table 35. Predicted Applied Load Uncertainty for the Ideal System

	NF (%FSE)	AF (%FSE)	PM (%FSE)
Centered System	0.034	0.022	0.050
Off-Center System	0.028	0.031	0.030

7 CONCLUSIONS

Considering the limited resources that were available, the proof-of-concept systems performed very well. Both prototypes successfully demonstrated the variable acceleration load application method. They also successfully performed factorial calibration experiments with an applied load error on the order of 1%FSE. The applied load error of the calibration experiments were all nearly within predicted intervals, suggesting that the largest sources of error for the systems were accounted for. The calibration accuracy using both systems is about one order of magnitude poorer than current accepted levels; however, a propagation of uncertainty analysis, using improved independent variable uncertainties, shows the feasibility of a production quality VACS. In the uncertainty analysis, prediction error dominated the pure error and calibration error. Angular velocity uncertainty and balance angle uncertainty seemed to have the largest effect out of all of the independent variable uncertainties. Numerous errors that went unaccounted for in the calibration experiments were discussed and solutions were proposed.

In terms of procurement, a few suggestions are made. The rate table used in this research was outdated. The table was manufactured in 1984, and the slip rings used to record data were unreliable. A future system could do without slip rings by either using a data logger or wireless telemetry; however, an additional solution to supply power to the balance and gyroscopes would be required. Investment in a new table would be expensive yet defendable since the table could also be used for accelerometer and gyroscope calibration research. Other rotation methods should be investigated as an alternative to rate tables. A robotic arm with rotating shaft could be beneficial because

the arm could be used to orient the axis of rotation with great flexibility. Investment in quality assurance of mechanically design components is also recommended for future research. The vernier caliper used in this research was acceptable for proof-of-concept; however, future improvements will benefit from the needed 0.005" coordinate measurement uncertainty.

Next, a comparison is made between both systems. The applied load error of the off-center system fell within predicted intervals 96% of the time, compared to 80% for the centered system. Additionally, the pure error demonstrated by the centered system was superior to that of the off-center system since fewer hardware changes were required using the multiple arm approach. The off-center system suffered from a large tare load to applied load ratio compared to the centered system. The tare load of the off-center system was about 40% of the full scale load while the tare load for the centered system was approximately 5%. It is easier to calculate the required independent variable settings based on the prescribed calibration loads for the off-center system compared to the centered system. Calculating the required independent variable settings from the calibration loads is a closed form solution for the off-center system. For the centered system, the calculations are performed numerically and are non-unique. This is a disadvantage for the centered system because a calibration system benefits from a methodology that is teachable and easily reproduced. The multiple arm load scheme used by the centered system contributes an unnecessary amount of uncertainty; however, it is an efficient method for attaching and detaching weight. The centered system was superior to the off-center system in terms of calibration time requirements. Based on the comparison of systems, the author recommends abandoning the center system concept.

Even though the centered system demonstrated superior time savings over the off-center system, the additional problems associated with loading multiple arms simultaneously were too detrimental.

The next stage of development of the off-center system should investigate how to reduce the large tare load to calibration load ratio. While using lighter fixture materials will provide an improvement, a methodology is needed that will better position the balance so that the center of gravity of the balance weight and fixture weight are closer to the axis of rotation for all runs during the calibration experiment. The methodology should be unique, so that given a balance with certain load ranges, the independent variables can be uniquely calculated for each run in the calibration experiment. This method should then be extended for six degree of freedom (6DOF) calibrations. A benefit of the off-center system loading method is that it uses a single load vector approach, similar to the SVS. This is beneficial because the SVS is a proven technology, which has already demonstrated 6DOF calibrations; therefore, 6DOF calibrations using the off-center system should be possible.

In the near future, the balance deflection angle measurement method, that uses a gyroscope, should be investigated. Balance deflection angle was clearly the most difficult independent variable to measure. All other independent variable measurements can be improved via procurement; however, the angle measurement technique needs time to mature. This angle measurement technique could also be used for attitude measurement of wind tunnel test articles. Both the VACS balance deflection problem and wind tunnel test article problem address angle measurement in the presence of forced oscillation. Forced oscillations impose a linear acceleration effect on a gyroscope

response. This type of error must be accounted for in the gyroscope calibration process. There are two objectives of the proposed research. The first is to develop a defendable method to validate the uncertainty of the gyro angle measurement in the presence of forced oscillation. The second is to demonstrate a ±0.004 degrees, or better, standard error in the gyro angle measurement.

A major selling point of the variable acceleration system is that it greatly improves the required calibration time of large capacity balances. While this may be true, it is now the author's belief that this benefit alone does not justify the investments that will be needed to move this research forward unless there is an unexpected increase in calibration demand. Calibrations systems are inherently expensive, and VACS is no exception. A large balance calibration should still be a targeted research objective; however, VACS needs to have a larger impact on wind tunnel measurement technology to justify its price tag. As previously mentioned, the procurement of a robotically controlled rotating shaft could be justified since it could also be used for gyroscope and accelerometer calibration. To achieve a greater impact on wind tunnel measurement technology, a balance, accelerometer and gyroscope could be integrated into a single measurement device, which could be calibrated using the rotating shaft. A new balance design could allow for the gyroscopes and accelerometers to be rigidly and orthogonally attached directly to the balance. Using the newly procured rate table, the integrated instrument could be calibrated in a single experiment. This could advance balance technology and provide superior physical insight into wind tunnel experimentation. The integrated instrument could be delivered to wind tunnels as a turn-key solution since all

components would be calibrated and maintained by a single laboratory, thereby streamlining the calibration process of wind tunnel instrumentation.

REFERENCES

[1] Rhew, R. D. (1999). *NASA LaRC Strain Gage Balance Design Concepts, 1st International Symposium on Strain Gauge Balances, Pt. 2.* (pp. 525-541). Hampton, VA.

[2] AIAA. (2003). *Calibration and Use of Internal Strain Gage Balances with Application to Wind Tunnel Testing, Recommended Practice.* AIAA R-091-2003.

[3] Hoffman, K. (1989). *An Introduction to Measurements using Strain Gages.* Germany: HBM.

[4] Parker, P. A., Morton, M., Draper, N., & Line, W. (2001). *A Single-Vector Force Calibration Method Featuring the Modern Design of Experiments*, AIAA-2001-0170, 39th AIAA Aerospace Sciences Meeting & Exhibit. Reno, NV.

[5] Hufnagel, K., & Quade, M. (2007). *The 2nd Generation Balance Calibration Machine of Darmstadt University of Technology (TUD).* AIAA 2007-148, 45th AIAA Aerospace Sciences Meeting and Exhibit. Reno, NV.

[6] Booth, D. (2008). *ABCS Calibration Load Schedule for Force Type Balances*, AIAA 2008-844.

[7] Booth, D., & King, D. (2006). *Automatic Balance Calibration System (ABCS) Upgrades*, AIAA 2006-516, 44th AIAA Aerospace Sciences Meeting and Exhibit. Reno, NV.

[8] Bergman, R., & Philipsen, I. (2010). *An Experimental Comparison of Different Load Tables for Balance Calibration, 7th International Symposium on Strain Gauge Balances.*

[9] Montgomery, D. C. (2005). *Design and Analysis of Experiments (*6th ed., pp. 434). NY: John Wiley & Sons.

[10] Meyers, R. H., & Montgomery, D. C. (2002). *Response Surface Methodology*, (2nd ed., pp. 760, 402). NY: John Wiley & Sons.

[11] Box, G. E. P., Hunter, W. G., Hunter, J. S., & Hunter, W. G. (1978). *Statistics for Experimenters: An introduction to Design, Data Analysis, and Model Building.* John Wiley and Sons.

[12] Landman, D., & Simpson, J. (2007). *A Wind Tunnel External Balance Calibration using Design of Experiments.* AIAA-2007-1604, US Air Force T&E Days. Destin, FL.

[13] Landman, D., Simpson, J., Vicroy, D., & Parker, P. (2007). *Design for Aircraft Wind-Tunnel Testing using Response Surface Methodologies* (Vol. 44, No. 4). AIAA Journal of Aircraft.

[14] Stewart, G. W. (1987). *Collinearity and Least Squares Regression, Statistical Science* (Vol 2, No 1, pg 68-100).

[15] Draper, N., & Smith, H. (1998). *Applied Regression Analysis* (3rd ed., Wiley Series in Probability and Statistics, pp. 25, 299-317). NY: John Wiley & Sons.

[16] Ulbrich, N., & Volden, T. (2008). *Predictive Capabilities of Regression Models used for Strain-Gage Balance Calibration Analysis*. AIAA Paper 2008-4028.

[17] Parker, P. A., & Liu, T. (2002). *Uncertainty Analysis of the Single-Vector Force Balance Calibration System*. AIAA-2002-2792, 22nd AIAA Aerodynamic Measurement Technology and Ground Testing Conference. St. Louis, MO.

[18] Bergmann, R., & Philipsen, I. (2010). *The evaluation of balance calibration data and the regression procedure at DNW.* AIAA-2010-4205, 27th AIAA Aerodynamic Measurement Technology and Ground Testing Conference. Chicago, IL.

[19] Coleman, H. W., & Steele, W.G. (1999). *Experimentation and Uncertainty Analysis for Engineers* (2nd Ed., 275 pp.). NY. John Wiley and Sons.

[20] Simpson, J., Landman, D., Giroux, R., Zeisset, M., Hall, B., & Rhew, R. (2005). *Calibrating Large Capacity Aerodynamic Force Balances using Response Surface Methods*. AIAA 2005-7601.

[21] Johnson, T. H., Parker, P. A., Landman, D. (2010). *Calibration Modeling of Nonmonolithic Wind-Tunnel Force Balances*. AIAA Journal of Aircraft, Vol. 47, No. 6, pp. 1860-1866, doi: 10.2514/1.46356, AIAA-46356-110

[22] Guarino, J. (1964). *Calibration and Evaluation of Multi-component Strain-Gage Balances.* NASA Interlaboratory Force Measurements Meeting, Jet Propulsion Laboratory.

[23] Montgomery, D. C., Peck, E. A., & Vining, G. G. (2006). *Introduction to Linear Regression Analysis* (4th Ed). NY: John Wiley & Sons.

[24] Ulbrich, N. (2009). *Regression Model Optimization for the Analysis of Experimental Data*. AIAA 2009-1344.

[25] Landman, D., Simpson, J., & Vicroy, D. (2006). *Efficient Methods for Complex Aircraft Configuration Aerodynamic Characterization using Response Surface Methodologies*. 44th AIAA Aerospace Sciences Meeting and Exhibit, Reno, NV.

[26] DeLoach, R. (2009). *The Role of Hierarchy in Response Surface Modeling of Wind Tunnel Data.* AIAA 2009-931.

[27] Moore, T. C. (2004). *Recommended Strain Gage Application Procedures for Various Langley Research Center Balance and Test Articles.* NASA TM-2004-213017.

APPENDIXES

A. Model Quality Metrics

Before performing a calibration experiment, the quality of the design and associated model is evaluated. The goal of this evaluation is to verify the adequacy of the design in estimating all of the required coefficients in the proposed calibration model. This phase does not require experimental data; rather, it is an evaluation of the design itself. There are a number of measures that provide insight into the design including: the Pearson correlation matrix, variance inflation factors and the distribution of normalized prediction variance.

For a given design matrix, with y being a column of responses and x a column of factors, the Pearson correlation coefficient $\boldsymbol{r_{xy}}$ describes the degree of the linearity between columns in the design [15] .

$$r_{xy} = \frac{\sum xy - \frac{\sum x \sum y}{N}}{\sqrt{(\sum x^2 - \frac{(\sum x)^2}{N})(\sum y^2 - \frac{(\sum y)^2}{N})}} \tag{43}$$

It can be shown that the range of r_{xy} is:

$$-1 \leq r_{xy} \leq 1 \quad . \tag{44}$$

Generally, values of r_{xy} near 1 indicate a strong positive linear association between x and y whereas values of r_{xy} near -1 indicate a strong negative linear association. Values of r_{xy} near 0 indicate little linear association between x and y. Computing the Pearson

correlation coefficient between each column in a design leads to a symmetrical correlation matrix $\boldsymbol{R}$ shown below.

$$\boldsymbol{R} = \begin{bmatrix} 1 & r_{12} & r_{13} & r_{14} & r_{15} & r_{16} \\ & 1 & r_{23} & r_{24} & r_{25} & r_{26} \\ & & 1 & r_{34} & r_{35} & r_{36} \\ & & & 1 & r_{45} & r_{46} \\ & sym & & & 1 & r_{56} \\ & & & & & 1 \end{bmatrix} \tag{45}$$

Variance inflation factors (VIF) are commonly used in place of correlation coefficients because of their more compact description of multi-collinearity in a design [14]. The variance inflation factor measures how much the variance of the model is increased by the lack of orthogonality in the design. True orthogonality guarantees that each regression coefficient estimate is independent of any other. Each term in the model (excluding the intercept) has a calculated VIF, where a VIF of one indicates orthogonality. As a variance inflation factor increases, the collinearity of that term with others in the model also increases. The variance inflation factors of a design are computed as the diagonal component of the inverse of the Pearson correlation matrix. A general rule of thumb is that a variance inflation factor greater than ten is an indication that multicollinearity may be unduly influencing the least squares estimates. Some believe this rule may be too lenient and suggest that a VIF should not exceed five [15] . A limitation to the use of VIFs is that they cannot distinguish between several simultaneous multicollinearities [21]. When high VIFs are encountered it is useful to refer back to the Pearson correlation matrix to determine which factors in particular are correlated.

The consequence of highly correlated model terms is large prediction variance estimates in the design space. The variance of a predicted value is a function of the model matrix and is calculated as follows [10]:

$$Var[R(x)] = x^{(m)'}(X'X)^{-1}x^{(m)} \cdot \sigma^2 \tag{46}$$

where $x^{(m)}$ is a function of location in the design space and also a function of the model, X is the model matrix, and σ^2 is the mean squared error. For comparative purposes, it is typical to let σ^2 equal one; therefore in terms of standard error of prediction, equation (47) becomes

$$\sqrt{Var[R(x)]} = \sqrt{x^{(m)'}(X'X)^{-1}x^{(m)}} \quad . \tag{47}$$

B. Typical SVS Calibration Design

Table 36. SVS Calibration Design

Run#	Block#	NF	AF	PM	RM	YM	SF	Run#	Block#	NF	AF	PM	RM	YM	SF
1	1	0 0	0 0	0 0	0 0	0 0	0 0	33	1	-0 6	0 4	-0 6	0 6	0 6	0 2
2	1	-0 6	-0 4	0 6	-0 6	0 6	-0 2	34	1	0 3	0 4	0 3	-0 3	-0 3	-0 5
3	1	-0 3	-0 4	0 3	0 3	0 3	-0 5	35	1	0 3	0 4	-0 3	-0 3	-0 3	0 5
4	1	-0 6	-0 4	-0 6	0 6	-0 6	-0 2	36	1	0 3	-0 4	0 3	0 3	-0 3	-0 5
5	1	0 6	-0 4	-0 6	-0 6	-0 6	0 2	37	1	0 0	0 0	0 0	0 0	0 0	0 0
6	1	-0 6	0 4	0 6	0 6	0 6	-0 2	38	2	0 0	0 0	0 0	0 0	0 0	0 0
7	1	-0 3	0 4	-0 3	0 3	-0 3	-0 5	39	2	1 0	0 0	0 0	0 0	0 0	-0 9
8	1	0 3	-0 4	-0 3	0 3	-0 3	0 5	40	2	0 0	0 0	0 0	0 0	0 0	1 0
9	1	-0 3	0 4	-0 3	-0 3	0 3	0 5	41	2	0 0	0 0	0 0	0 0	1 0	1 0
10	1	0 6	0 4	0 6	0 6	-0 6	-0 2	42	2	-1 0	0 0	0 0	0 0	0 0	0 0
11	1	-0 6	-0 4	0 6	0 6	-0 6	0 2	43	2	0 0	1 0	0 0	0 0	0 0	0 0
12	1	-0 6	0 4	-0 6	-0 6	-0 6	-0 2	44	2	-1 0	0 0	-1 0	0 0	0 0	0 0
13	1	0 0	0 0	0 0	0 0	0 0	0 0	45	2	0 0	0 0	0 0	0 0	0 0	0 0
14	1	-0 3	-0 4	-0 3	-0 3	-0 3	-0 5	46	2	-1 0	0 0	0 0	0 0	0 0	0 9
15	1	0 0	0 0	0 0	0 0	0 0	0 0	47	2	1 0	0 0	1 0	0 0	0 0	0 0
16	1	0 3	0 4	-0 3	0 3	0 3	-0 5	48	2	1 0	0 0	0 0	-1 0	0 0	0 0
17	1	-0 3	0 4	0 3	0 3	-0 3	0 5	49	2	-1 0	0 0	0 0	1 0	0 0	0 0
18	1	-0 3	-0 4	-0 3	0 3	0 3	0 5	50	2	0 0	0 0	0 0	0 0	0 0	0 0
19	1	0 6	0 4	-0 6	0 6	-0 6	0 2	51	2	-1 0	0 0	0 0	0 0	0 0	-0 9
20	1	0 3	-0 4	0 3	-0 3	0 3	0 5	52	2	0 0	0 0	0 0	0 0	0 0	-1 0
21	1	0 3	-0 4	-0 3	-0 3	0 3	-0 5	53	2	1 0	0 0	0 0	0 0	0 0	0 9
22	1	0 6	-0 4	-0 6	0 6	0 6	-0 2	54	2	1 0	0 0	-1 0	0 0	0 0	0 0
23	1	0 6	-0 4	0 6	-0 6	-0 6	-0 2	55	2	0 0	0 0	0 0	0 0	-1 0	1 0
24	1	0 6	0 4	0 6	-0 6	0 6	0 2	56	2	-1 0	0 0	0 0	-1 0	0 0	0 0
25	1	-0 3	-0 4	0 3	-0 3	-0 3	0 5	57	2	0 0	0 0	0 0	0 0	1 0	-1 0
26	1	0 6	0 4	-0 6	-0 6	0 6	-0 2	58	2	-1 0	0 0	1 0	0 0	0 0	0 0
27	1	0 0	0 0	0 0	0 0	0 0	0 0	59	2	0 0	-1 0	0 0	0 0	0 0	0 0
28	1	0 6	-0 4	0 6	0 6	0 6	0 2	60	2	0 0	0 0	0 0	0 0	0 0	0 0
29	1	-0 3	0 4	0 3	-0 3	0 3	-0 5	61	2	0 0	0 0	0 0	0 0	-1 0	-1 0
30	1	-0 6	0 4	0 6	-0 6	-0 6	0 2	62	2	1 0	0 0	0 0	0 0	0 0	0 0
31	1	0 3	0 4	0 3	0 3	0 3	0 5	63	2	1 0	0 0	0 0	1 0	0 0	0 0
32	1	-0 6	-0 4	-0 6	-0 6	0 6	0 2	64	2	0 0	0 0	0 0	0 0	0 0	0 0

C. Governing Equations Derivation

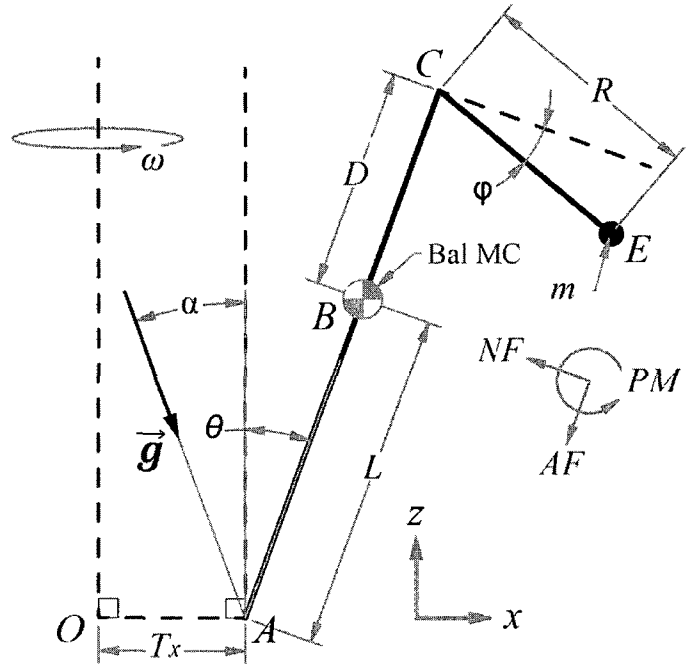

Figure 47. Generic VACS Representation

Let the inertial reference frame $\mathcal{F}$ be fixed to the earth. Let reference frame $\mathcal{B}$ be fixed to the rate table having an identical coordinate system as frame $\mathcal{F}$ at time $t = 0$. Let line segment AC represent the force balance, where point A is the sting end attachment point to the table and point B is the moment center of the balance. Line segment OA represents the surface of the table. The mass is attached to the balance at point E where the acceleration at that point is calculated as

$$^{\mathcal{F}}\boldsymbol{a}_E = {}^{\mathcal{F}}\boldsymbol{a}_O + {}^{\mathcal{B}}\boldsymbol{a}_{E/O} + \left[{}^{\mathcal{F}}\boldsymbol{\alpha}^{\mathcal{B}} \times {}^{\mathcal{B}}\boldsymbol{\rho}_{E/O}\right] + \left[2\,{}^{\mathcal{F}}\boldsymbol{\omega}^{\mathcal{B}} \times {}^{\mathcal{B}}\boldsymbol{v}_{E/O}\right]$$
$$+ \left[{}^{\mathcal{F}}\boldsymbol{\omega}^{\mathcal{B}} \times \left({}^{\mathcal{F}}\boldsymbol{\omega}^{\mathcal{B}} \times {}^{\mathcal{B}}\boldsymbol{\rho}_{E/O}\right)\right]$$

$^{\mathcal{F}}\boldsymbol{a}_E$ = linear acceleration of point E in reference frame $\mathcal{F}$

$^{\mathcal{F}}\boldsymbol{a}_O$ = linear acceleration of point O in reference frame $\mathcal{F}$

${}^{\mathcal{B}}\boldsymbol{a}_{E/O}$ = linear acceleration of point E relative to point O as observed in reference frame $\mathcal{B}$

${}^{\mathcal{F}}\boldsymbol{\alpha}^{\mathcal{B}}$ = angular acceleration of reference frame $\mathcal{B}$ with respect to reference frame $\mathcal{F}$

${}^{\mathcal{B}}\boldsymbol{\rho}_{E/O}$ = position of point E relative to point O in reference frame $\mathcal{B}$ coordinates

${}^{\mathcal{F}}\boldsymbol{\omega}^{\mathcal{B}}$ = angular velocity of reference frame $\mathcal{B}$ with respect to reference frame $\mathcal{F}$

${}^{\mathcal{B}}\boldsymbol{v}_{E/O}$ = linear velocity of E relative to point O as observed in reference frame $\mathcal{B}$

${}^{\mathcal{F}}\boldsymbol{\alpha}^{\mathcal{B}} \times {}^{\mathcal{B}}\boldsymbol{\rho}_{E/O}$ = Euler Acceleration

$2\,{}^{\mathcal{F}}\boldsymbol{\omega}^{\mathcal{B}} \times {}^{\mathcal{B}}\boldsymbol{v}_{E/O}$ = Coriolis Acceleration

${}^{\mathcal{F}}\boldsymbol{\omega}^{\mathcal{B}} \times \left({}^{\mathcal{F}}\boldsymbol{\omega}^{\mathcal{B}} \times {}^{\mathcal{B}}\boldsymbol{\rho}_{E/O}\right)$ =Centripetal Acceleration

${}^{\mathcal{F}}\boldsymbol{g}$ = Gravitational acceleration observed in reference frame $\mathcal{F}$

Since the base of the table is fixed in the lab, the linear acceleration ${}^{\mathcal{F}}\boldsymbol{a}_O$ is equal to the gravitational acceleration, ${}^{\mathcal{F}}\boldsymbol{g}$. For each run in the experiment, the mass is rigidly fixed to the balance, and the balance is rigidly fixed to the table; therefore, the linear acceleration ${}^{\mathcal{B}}\boldsymbol{a}_{E/O}$ and linear velocity ${}^{\mathcal{B}}\boldsymbol{v}_{E/O}$ are equal to zero. Furthermore, since the table rotates with constant angular velocity, the angular acceleration term ${}^{\mathcal{F}}\boldsymbol{\alpha}^{\mathcal{B}}$ is also equal to zero. All that remains is the centripetal and gravitational acceleration as shown below.

$$ {}^{\mathcal{F}}\boldsymbol{a}_E = {}^{\mathcal{F}}\boldsymbol{\omega}^{\mathcal{B}} \times \left({}^{\mathcal{F}}\boldsymbol{\omega}^{\mathcal{B}} \times {}^{\mathcal{B}}\boldsymbol{\rho}_{E/O}\right) + {}^{\mathcal{F}}\boldsymbol{g} $$

From Newton's second law, the resulting force imparted by the attached mass is

$$ \boldsymbol{F} = m\left[{}^{\mathcal{F}}\boldsymbol{\omega}^{\mathcal{B}} \times \left({}^{\mathcal{F}}\boldsymbol{\omega}^{\mathcal{B}} \times {}^{\mathcal{B}}\boldsymbol{\rho}_{E/O}\right) + {}^{\mathcal{F}}\boldsymbol{g}\right] \quad . $$

Or more generically,

$$ \boldsymbol{F} = m[\boldsymbol{\omega} \times (\boldsymbol{\omega} \times \boldsymbol{r}) + \boldsymbol{g}] \quad . $$

This equation can be further simplified by assuming the problem is two dimensional, and that all forces act in the X and Z directions. The following points are defined before and after deflections (both balance and arm deflections).

Table 37. Variables of Governing Equation After Deflection

	Before Deflections	After Deflections
Unit NF direction	$\begin{bmatrix}-1\\0\\0\end{bmatrix}$	$\begin{bmatrix}-cos\theta\\0\\sin\theta\end{bmatrix}$
Unit AF direction	$\begin{bmatrix}0\\0\\-1\end{bmatrix}$	$\begin{bmatrix}-sin\theta\\0\\-cos\theta\end{bmatrix}$
Unit Centrifugal Force Direction	$\begin{bmatrix}1\\0\\0\end{bmatrix}$	$\begin{bmatrix}1\\0\\0\end{bmatrix}$
Unit Gravity Force Direction	$\begin{bmatrix}0\\0\\-1\end{bmatrix}$	$\begin{bmatrix}-sin\alpha\\0\\-cos\alpha\end{bmatrix}$ at $t_0 = 0$, $\begin{bmatrix}sin\alpha\\0\\-cos\alpha\end{bmatrix}$ after ½ revolution
Point O	$\begin{bmatrix}0\\0\\0\end{bmatrix}$	$\begin{bmatrix}0\\0\\0\end{bmatrix}$
Point A	$\begin{bmatrix}T_x\\0\\0\end{bmatrix}$	$\begin{bmatrix}T_x\\0\\0\end{bmatrix}$
Point C	$\begin{bmatrix}T_x\\0\\L+D\end{bmatrix}$	$\begin{bmatrix}(L+D)sin\theta+T_x\\0\\(L+D)cos\theta\end{bmatrix}$
Point E	$\begin{bmatrix}R+T_x\\0\\L+D\end{bmatrix}$	$\begin{bmatrix}(L+D)sin\theta+T_x+Rcos\phi cos\theta-Rsin\phi sin\theta\\0\\(L+D)cos\theta-Rsin\phi cos\theta-Rcos\phi sin\theta\end{bmatrix}$

The centrifugal force is

$$\boldsymbol{F}_{cent} = [m\tilde{R}\omega^2, 0, 0]$$

where $\tilde{R}$ is the x-component of the distance between points O and E.

$$\tilde{R} = (L + D)sin\theta + T_x + Rcos\phi cos\theta - Rsin\phi sin\theta$$

Then the amount of centrifugal force along the unit normal direction is

$$NF_{cent} = \boldsymbol{F}_{cent} \cdot \boldsymbol{NF}_{unit}$$

$$NF_{cent} = -m\omega^2\{(L + D)sin\theta + T_x + Rcos\phi cos\theta - Rsin\phi sin\theta\}cos\theta \quad .$$

Similarly, the amount of centrifugal force along the axial direction is

$$AF_{cent} = -m\omega^2\{(L + D)sin\theta + T_x + Rcos\phi cos\theta - Rsin\phi sin\theta\}sin\theta \quad .$$

Before the table begins to rotate (t_0), the gravity vector is defined as

$$\boldsymbol{F}_{grav,t_0} = \begin{bmatrix} -sin\alpha \\ 0 \\ -cos\alpha \end{bmatrix} \quad .$$

After the table makes a half revolution the gravity vector is defined as

$$\boldsymbol{F}_{grav,t_1} = \begin{bmatrix} sin\alpha \\ 0 \\ -cos\alpha \end{bmatrix} \quad .$$

Then the normal force component of gravity at t_0 and t_1 are

$$NF_{grav,t_0} = \boldsymbol{F}_{grav,t_0} \cdot \boldsymbol{NF}_{unit}$$

$$NF_{grav,t_1} = \boldsymbol{F}_{grav,t_1} \cdot \boldsymbol{NF}_{unit}$$

or

$$NF_{grav,t_0} = mg(sin\alpha cos\theta - cos\alpha sin\theta)$$

$$NF_{grav,t_1} = -mg(sin\alpha cos\theta + cos\alpha sin\theta) \quad .$$

The actual experiment will average the loads over multiple revolutions; therefore, for this analysis we are interested in the normal force gravity component averaged over one complete revolution, i.e.

$$NF_{grav} = \frac{NF_{grav,t_0} + NF_{grav,t_1}}{2}$$

$$NF_{grav} = -mgcos\alpha sin\theta$$

Similarly, the axial force gravity component is calculated as

$$AF_{grav} = mgcos\alpha cos\theta \quad .$$

Next, the total forces are calculated as

$$NF = NF_{cent} + NF_{grav}$$

$$AF = AF_{cent} + AF_{grav}$$

or

$$NF = -m\omega^2[T_x + sin(\theta)(L + D) + cos(\phi)cos(\theta)R - sin(\phi)sin(\theta)R]cos(\theta) - mgcos(\alpha)sin(\theta)$$

$$AF = -m\omega^2[T_x + sin(\theta)(L + D) + cos(\phi)cos(\theta)R - sin(\phi)sin(\theta)R]sin(\theta) + mgcos(\alpha)cos(\theta) \quad .$$

Finally, pitching moment is calculated as

$$\boldsymbol{M} = \boldsymbol{\rho}_{E/O} \times \boldsymbol{F}$$

where

$$\boldsymbol{\rho}_{E/O} = \begin{bmatrix} Rcos\phi + Dsin\phi \\ 0 \\ -Rsin\phi + Dcos\phi \end{bmatrix}$$

and

$$\boldsymbol{F} = \begin{bmatrix} NF \\ 0 \\ AF \end{bmatrix} \quad .$$

Thus, pitching moment is

$$PM = [cos(\phi)D - sin(\phi)R]NF + [sin(\phi)D + cos(\phi)R]AF \quad .$$

D. Centered System CAD Drawings

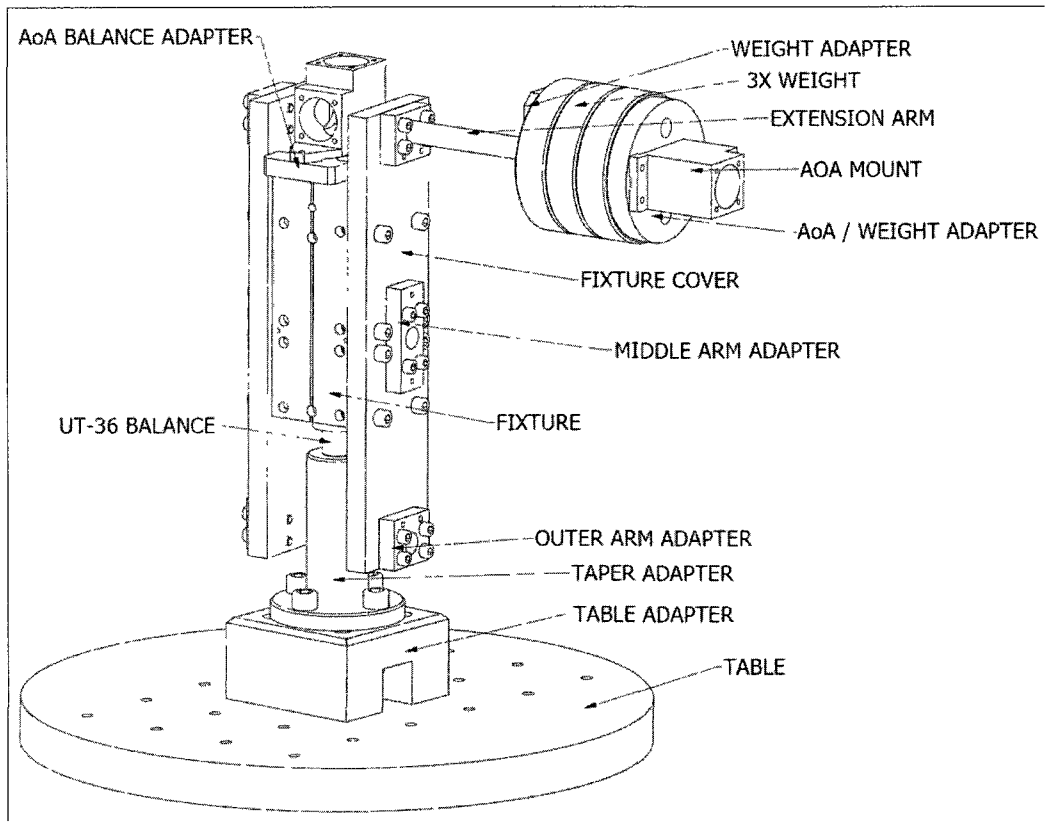

Figure 48. Centered System

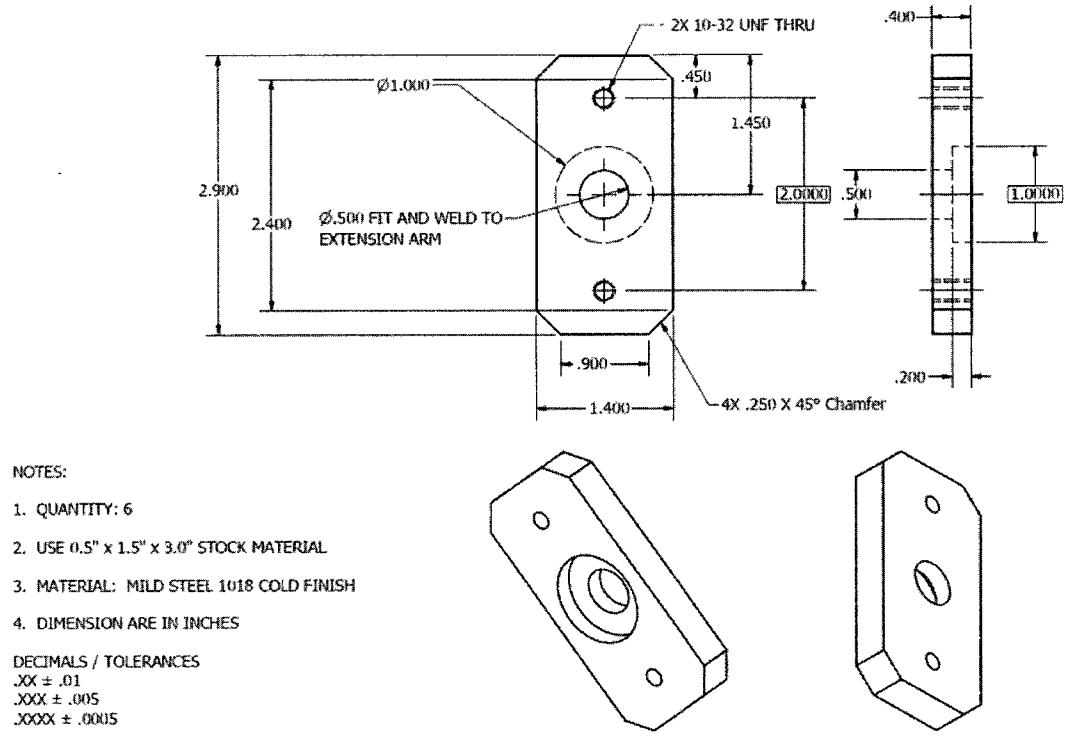

Figure 49. Centered System Weight Adapter CAD Drawing

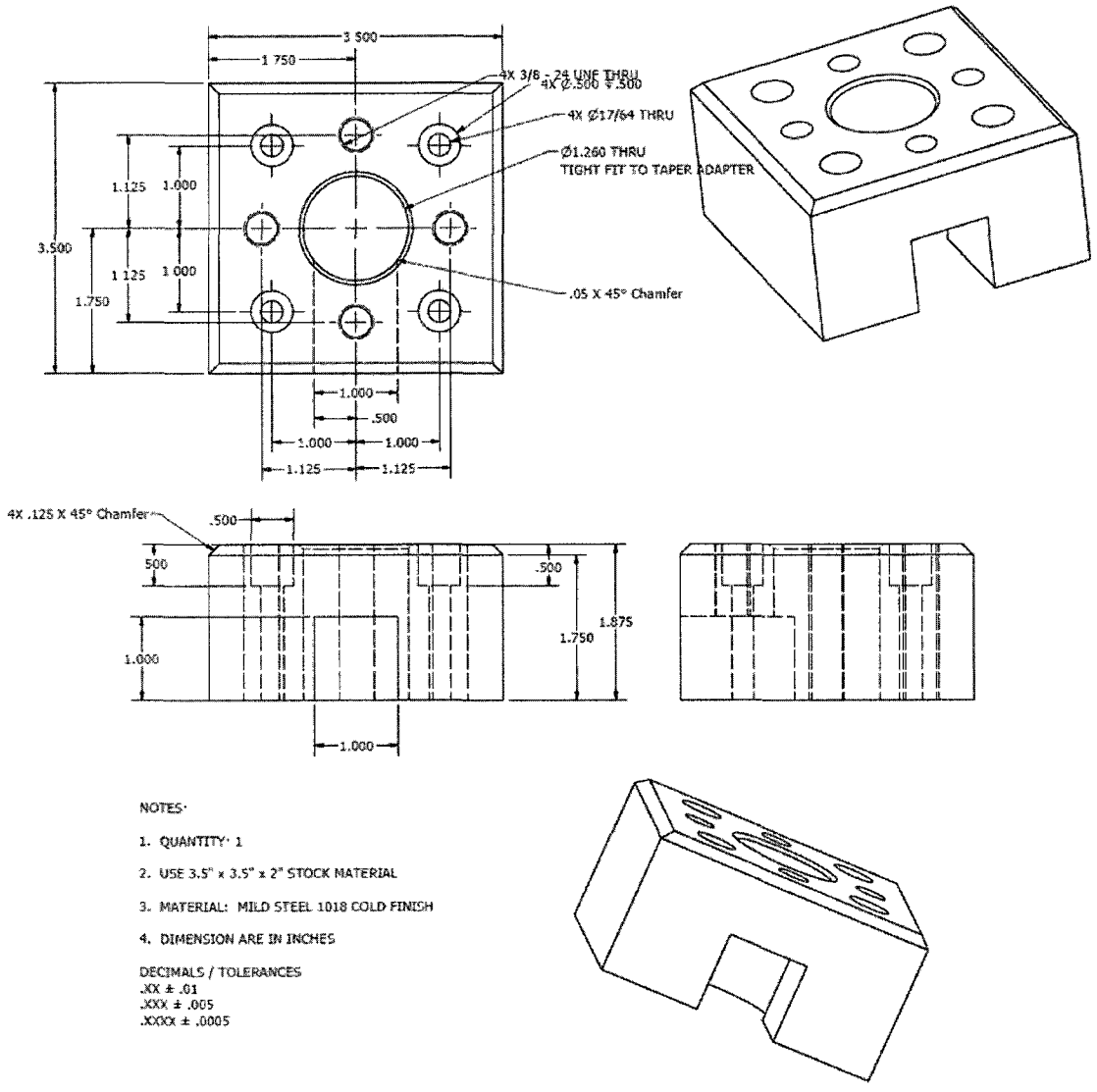

Figure 50. Centered System Table Adapter CAD Drawing

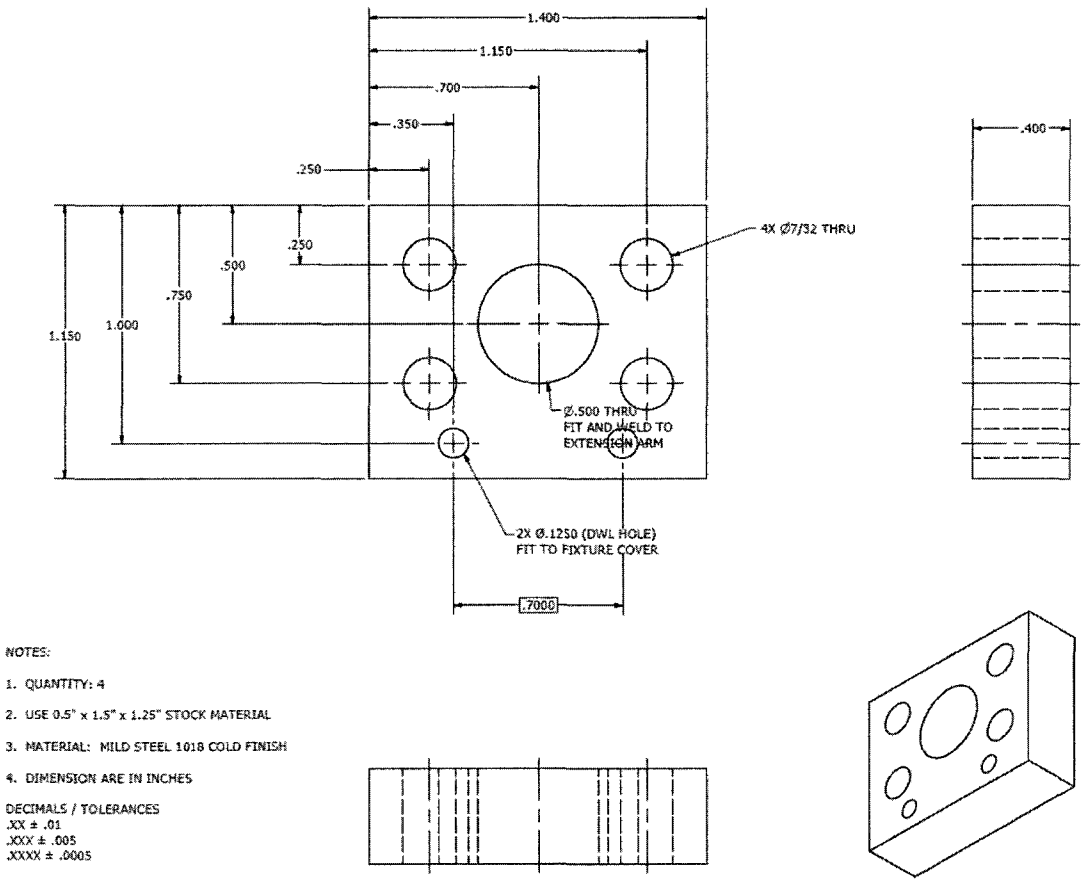

Figure 51. Centered System Outer Arm Adapter CAD Drawing

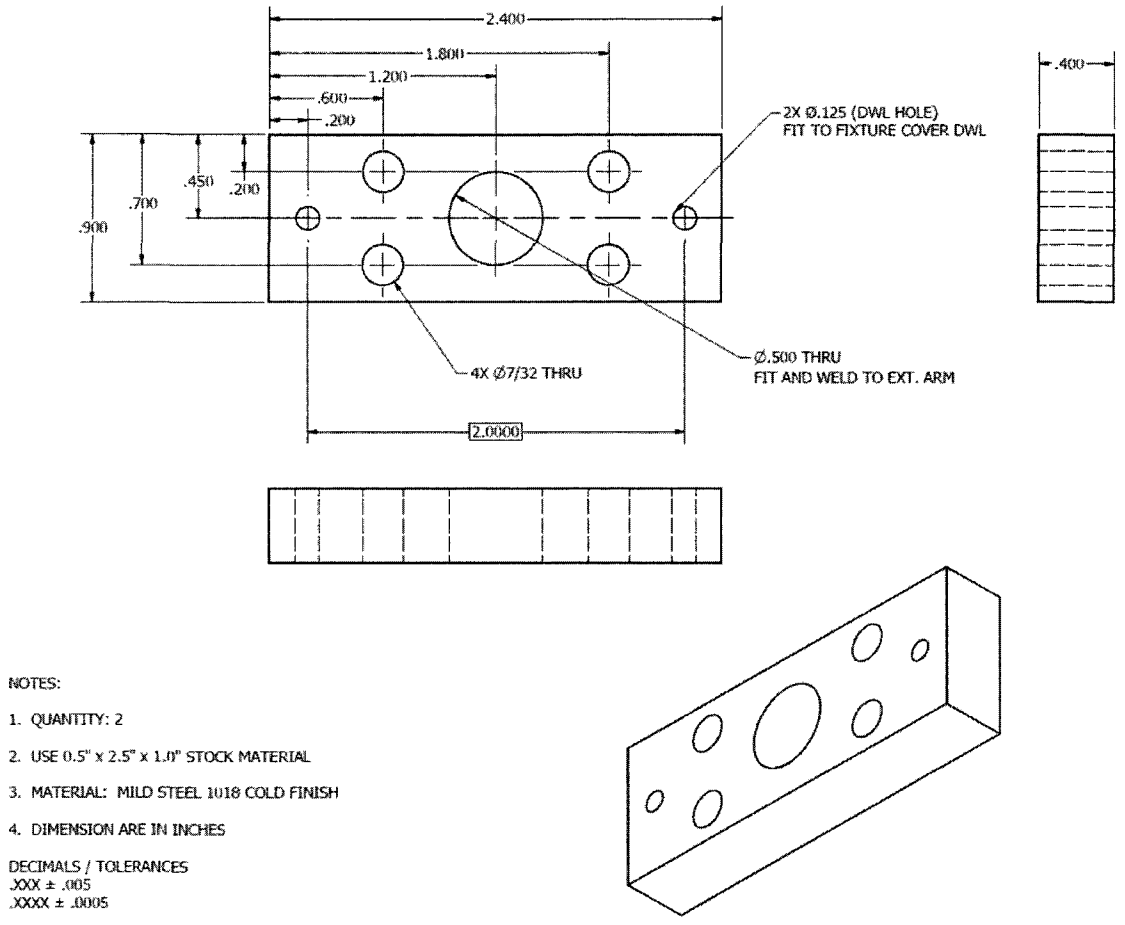

Figure 52. Centered System Middle Arm Adapter CAD Drawing

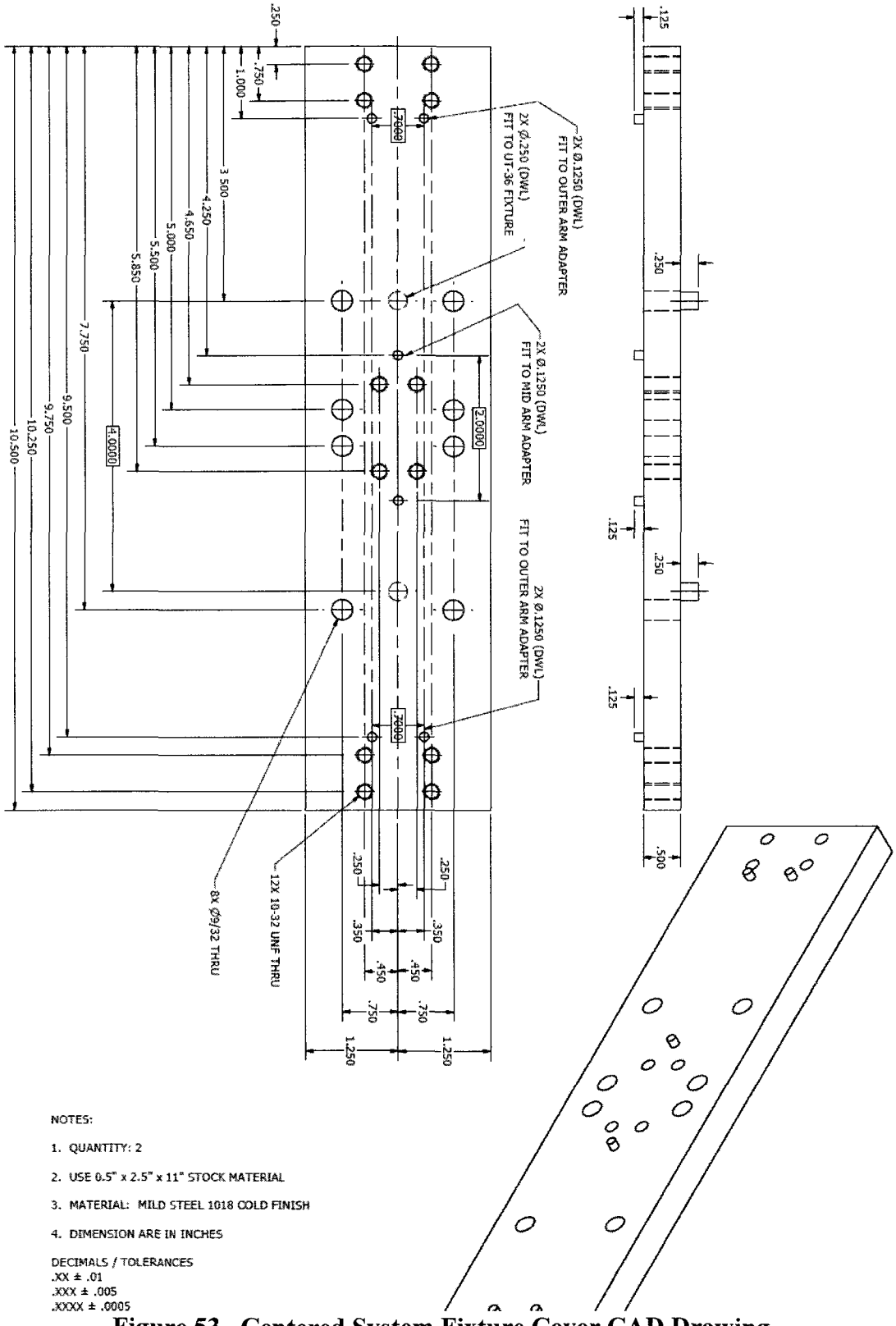

Figure 53. Centered System Fixture Cover CAD Drawing

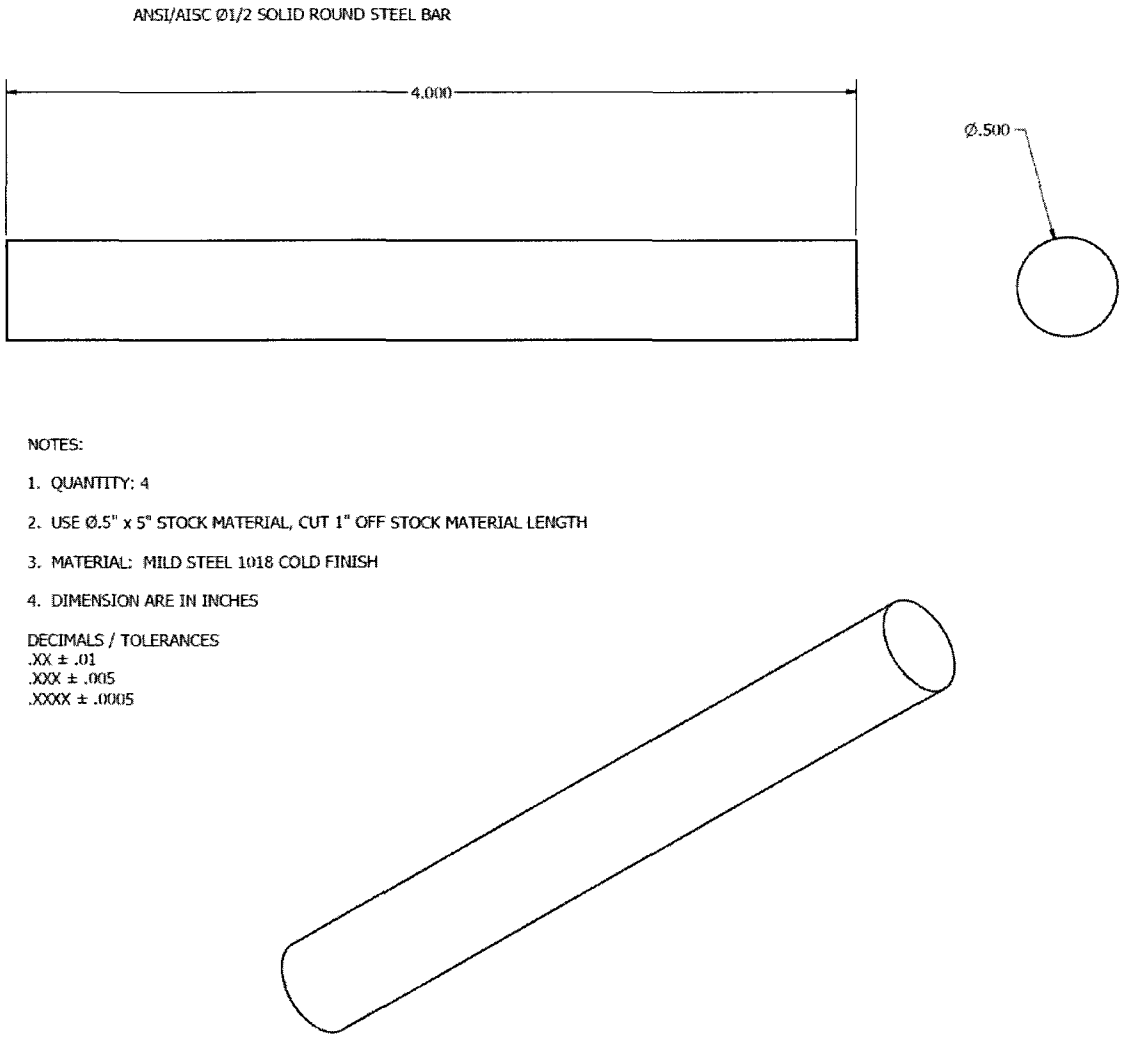

Figure 54. Centered System Arm CAD Drawing

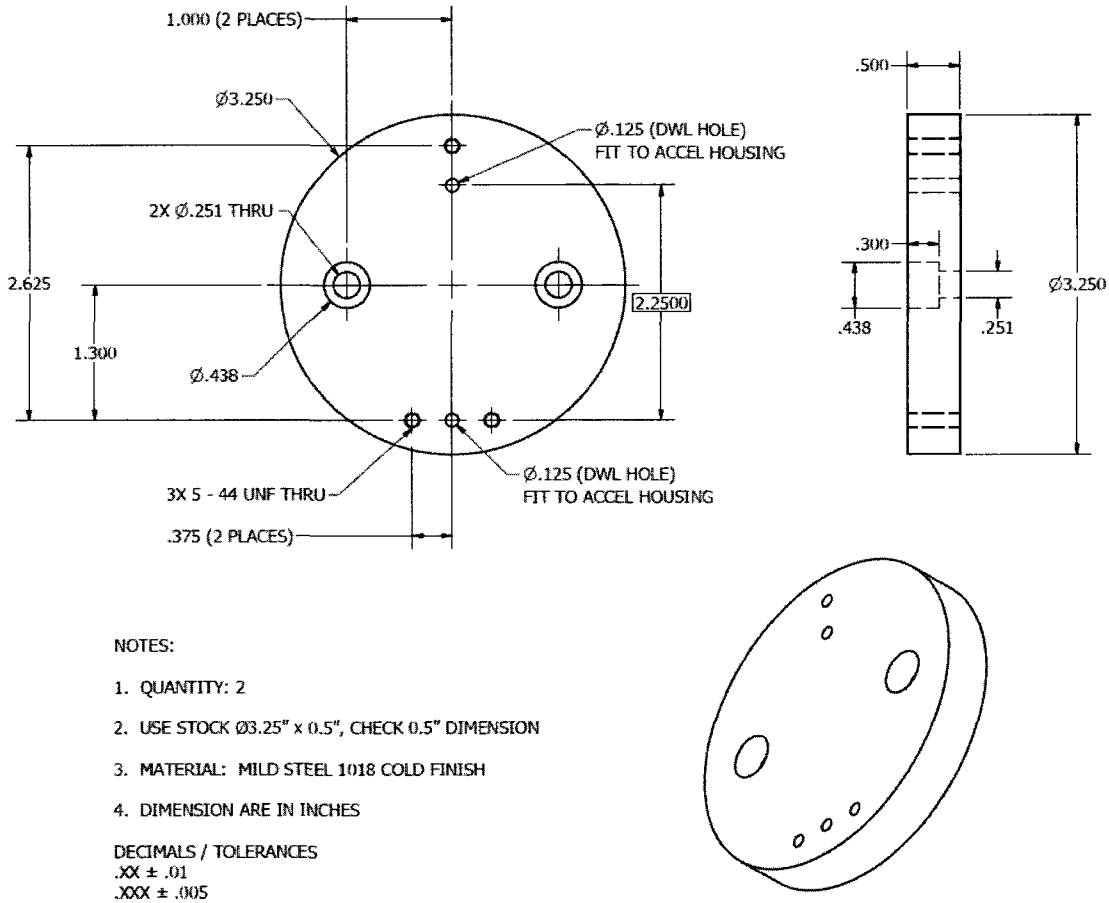

Figure 55. Centered System Arm Accelerometer Adapter CAD Drawing

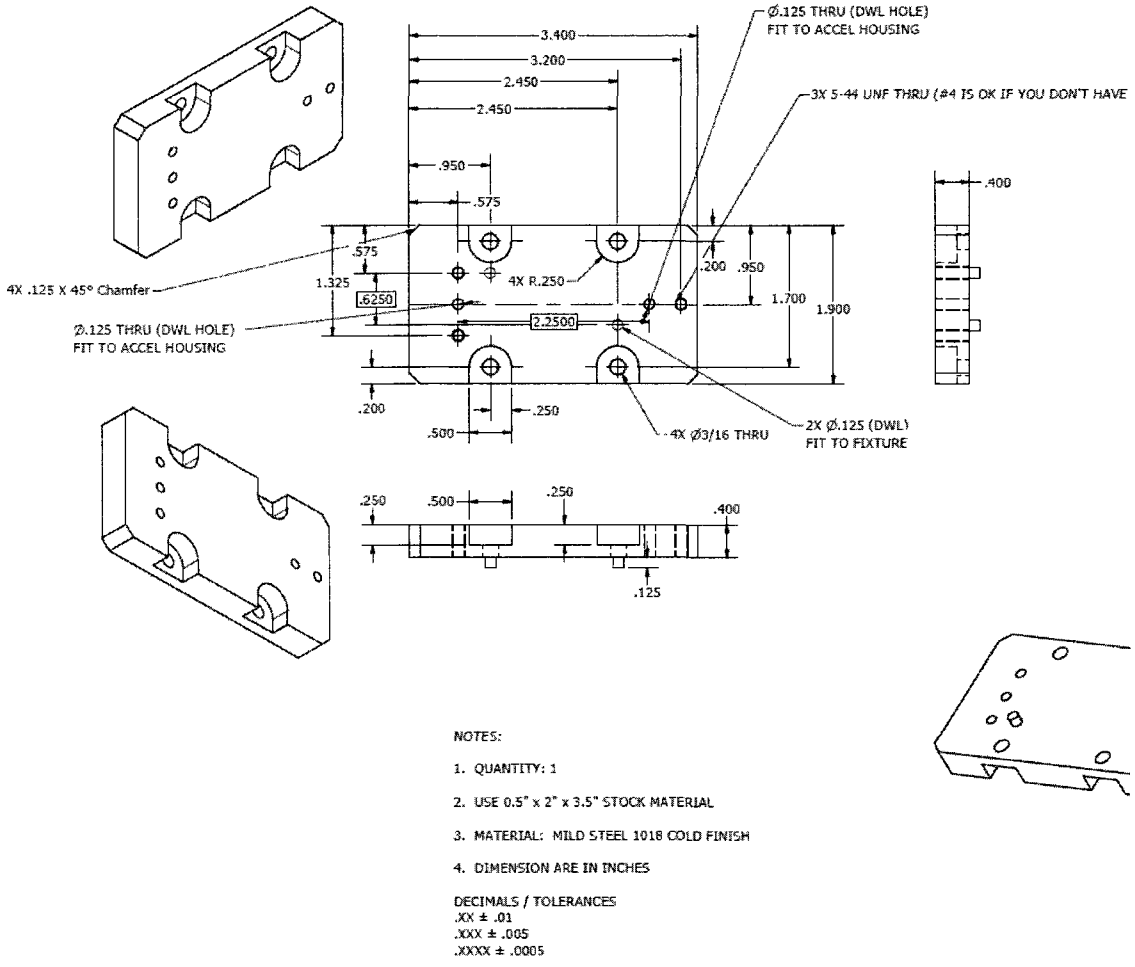

Figure 56. Centered System Accelerometer Adapter CAD Drawing

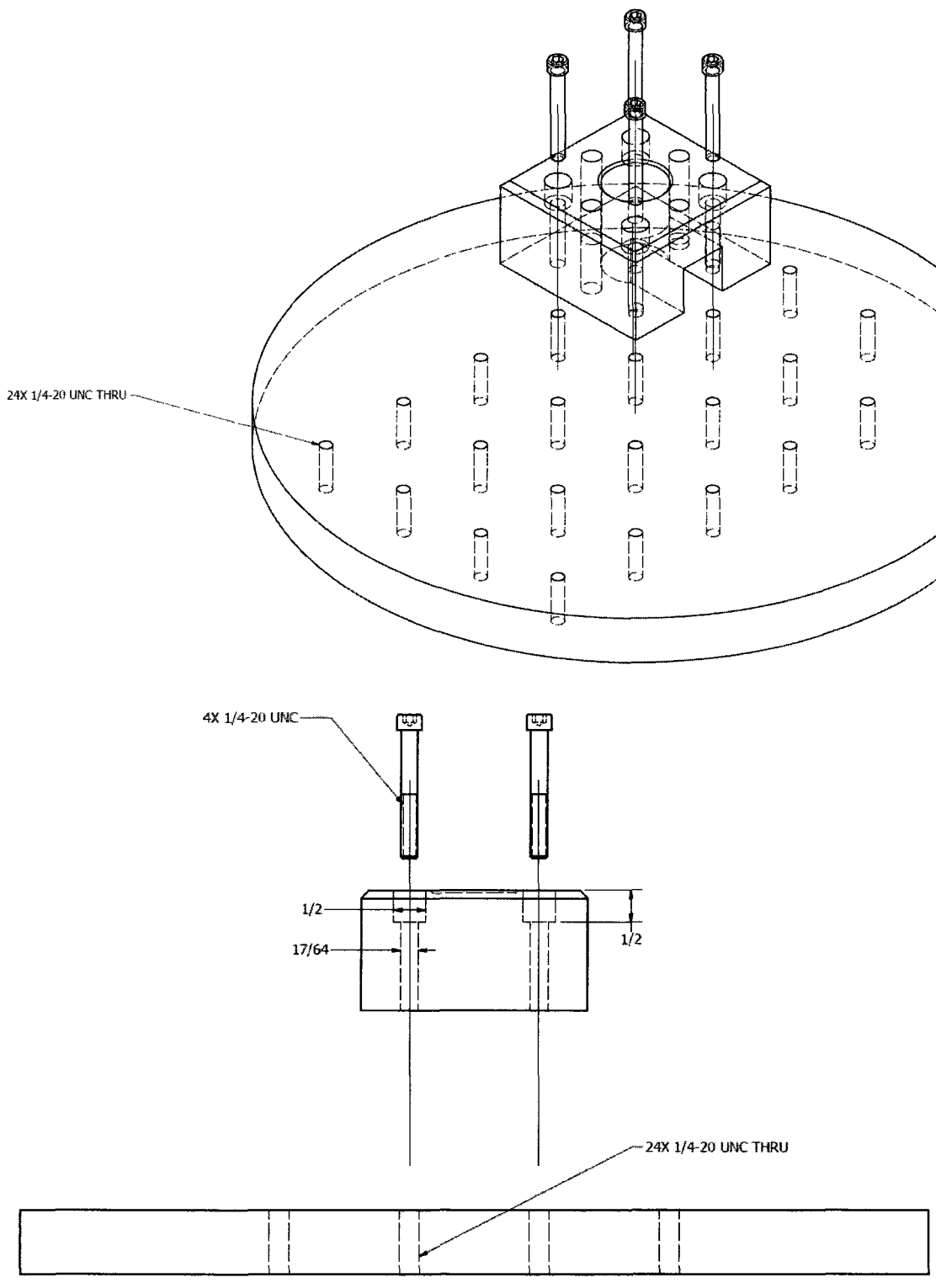

Figure 57. Centered System Table Adapter Assembly

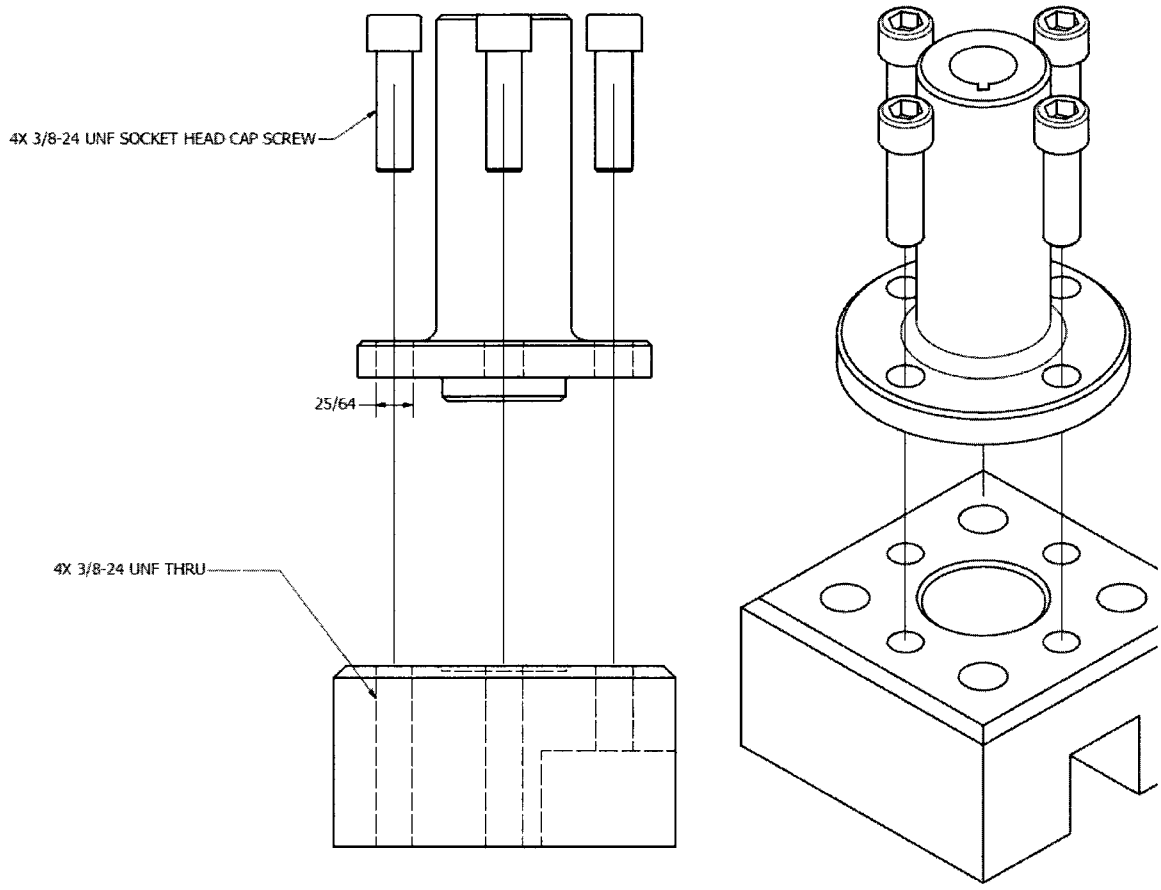

Figure 58. Centered System Taper Adapter Assembly

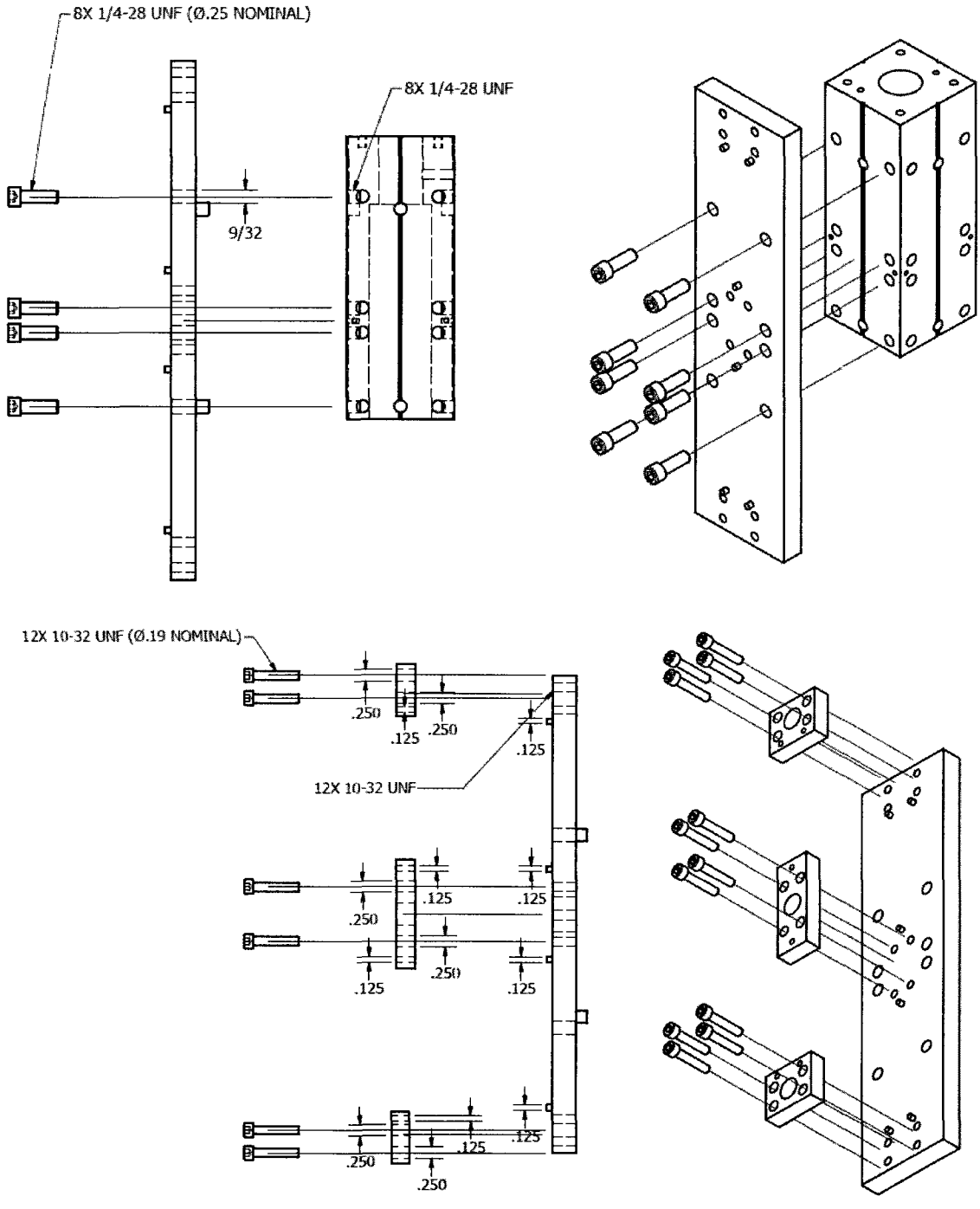

Figure 59. Centered System Fixture Cover Assembly

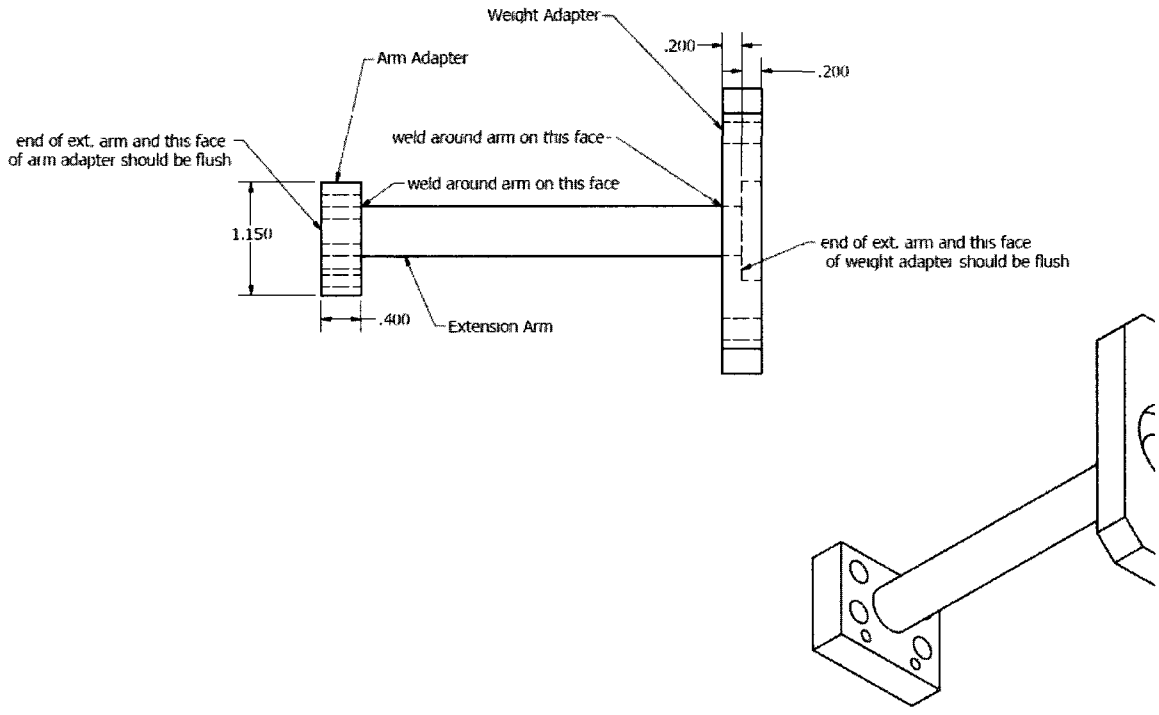

Figure 60. Centered System Arm Assembly

E. Three Axis Accelerometer Calibration

The three-axis accelerometer calibration experiment is shown in table 38.

Table 38. Three Axis Accelerometer Package Calibration Experiment

	Factor Settings (deg)		Factor Settings (g's)			Responses (Volts)		
Run #	Pitch	Roll	Gx	Gy	Gz	Vx	Vy	Vz
1	0	-90	0.000	1.000	0.000	0.006	1.284	0.006
2	180	-90	0.000	-1.000	0.000	0.007	-1.272	0.005
3	-145	-135	-0.574	-0.579	0.579	-0.732	-0.735	0.752
4	145	-45	0.574	-0.579	-0.579	0.746	-0.734	-0.742
5	35	-45	0.574	0.579	0.579	0.746	0.747	0.753
6	-35	-45	-0.574	0.579	0.579	-0.733	0.746	0.753
7	0	-90	0.000	1.000	0.000	0.006	1.284	0.006
8	145	-135	0.574	-0.579	0.579	0.747	-0.734	0.752
9	-145	-45	-0.574	-0.579	-0.579	-0.734	-0.734	-0.741
10	0	-180	0.000	0.000	-1.000	0.005	0.007	-1.284
11	0	-90	0.000	1.000	0.000	0.006	1.284	0.006
12	-35	-135	-0.574	0.579	-0.579	-0.735	0.747	-0.741
13	-90	-90	-1.000	0.000	0.000	-1.283	0.006	0.006
14	180	-90	0.000	-1.000	0.000	0.007	-1.272	0.005
15	0	0	0.000	0.000	1.000	0.008	0.006	1.295
16	180	-90	0.000	-1.000	0.000	0.007	-1.272	0.005
17	90	-90	1.000	0.000	0.000	1.296	0.007	0.006
18	180	-90	0.000	-1.000	0.000	0.007	-1.272	0.005
19	35	-135	0.574	0.579	-0.579	0.745	0.747	-0.741
20	0	-90	0.000	1.000	0.000	0.006	1.284	0.006

The confirmation experiment for the calibration is shown in table 39. The calibration accuracy is the two-standard deviation using the calibration and confirmation points.

Table 39. Three Axis Accelerometer Package Confirmation Experiment

	Factor Settings (deg)		Factor Settings (g's)			Responses (Volts)		
Run #	Pitch	Roll	Gx	Gy	Gz	Vx	Vy	Vz
1	144	-80	0.588	-0.797	-0.140	0.765	-1.012	-0.176
2	-50	144	-0.766	-0.378	-0.520	-0.982	-0.477	-0.665
3	40	-28	0.643	0.360	0.676	0.836	0.466	0.878
4	-60	-179	-0.866	0.009	-0.500	-1.111	0.017	-0.639
5	-8	17	-0.139	-0.290	0.947	-0.172	-0.365	1.227
6	-163	128	-0.292	0.754	0.589	-0.371	0.969	0.765
7	-115	149	-0.906	0.218	0.362	-1.162	0.284	0.473
8	97	-7	0.993	-0.015	-0.121	1.286	-0.012	-0.150
9	-106	-45	-0.961	-0.195	-0.195	-1.233	-0.243	-0.246
10	-179	-126	-0.017	-0.809	0.588	-0.015	-1.028	0.763
11	-71	-178	-0.946	0.011	-0.325	-1.214	0.020	-0.414
12	37	-126	0.602	0.646	-0.469	0.781	0.833	-0.600
13	-115	178	-0.906	0.015	0.422	-1.162	0.024	0.550
14	-160	107	-0.342	0.899	0.275	-0.435	1.154	0.360
15	-15	99	-0.259	-0.954	-0.151	-0.327	-1.213	-0.190
16	-141	69	-0.629	0.726	-0.279	-0.806	0.933	-0.353
17	137	-20	0.682	-0.250	-0.687	0.885	-0.313	-0.881
18	19	-89	0.326	0.945	0.017	0.426	1.215	0.027
19	93	-46	0.999	-0.038	-0.036	1.294	-0.041	-0.041
20	-61	-10	-0.875	0.084	0.477	-1.121	0.113	0.621

Reverse regression was used, meaning the g vectors were directly modeled as a function of accelerometer output voltages.

Table 40. Three Axis Accelerometer Package Calibration Equations

Gx	=	Gy	=	Gz	=
-0.0213		-0.1115		-0.0147	
0.7752	* Vx	-0.0012	* Vx	0.0000	* Vx
0.0004	* Vy	0.7816	* Vy	-0.0003	* Vy
-0.0008	* Vz	-0.0003	* Vz	0.7754	* Vz
0.0000	* Vx * Vy	0.0000	* Vx * Vy	0.0000	* Vx * Vy
0.0000	* Vx * Vz	-0.0001	* Vx * Vz	0.0000	* Vx * Vz
0.0000	* Vy * Vz	0.0000	* Vy * Vz	0.0000	* Vy * Vz
0.0098	* Vx^2	0.0641	* Vx^2	0.0062	* Vx^2
0.0100	* Vy^2	0.0653	* Vy^2	0.0063	* Vy^2
0.0098	* Vz^2	0.0642	* Vz^2	0.0063	* Vz^2

The following equations can be used to calculate pitch and roll angle. The second pitch equation is preferred over the first since it provides a stable answer over a 90 degree pitch.

$$Pitch\ (deg) = sin^{-1}(G_X)$$

$$Pitch\ (deg) = tan^{-1}\left(\frac{G_X}{\sqrt{G_Y^2 + G_z^2}}\right)$$

$$Roll\ (deg) = tan^{-1}\left(\frac{G_Y}{\sqrt{G_X^2 + G_z^2}}\right)$$

Table 41. Results of the Confirmation Experiment, Predicted Minus Actual

	Gx	Gy	Gz	Mean
2sigma (g's)	2.19E-05	1.75E-05	2.06E-05	2.00E-05
2sigma (deg)	1.26E-03	1.01E-03	1.18E-03	1.15E-03

F. UT-36 Manual Stand Calibration Summary

* * * * * * * * * * * * * * * * * * * N A S A * * * * * * * * * * * * * * * * * *
* * * * * * * * * * * * * * * Langley Research Center * * * * * * * * * * * * * * * *

STRAIN GAGE BALANCE CALIBRATION RESULTS

FINAL **FINAL**

Balance: **UT36** Engineer: RHEW
Calibration Date: **01/22/96**

Component	Calibration Range		Full Scale Output	Sensitivity Constant		Accuracy
	(lb or in-lb)	(N or Nm)	(mV/V)	(lb/mV/V) or (in-lb/mV/V)	(N/mV/V) or (Nm/mV/V)	% F.S. (±2σ)
1 NORMAL	100.0	444.822	0.977	102.3420	455.2400	0.04
	-100.0	-444.822				
2 AXIAL	60.0	266.893	1.025	58.5210	260.3144	0.06
	0.0	0.000				
3 PITCH	800.0	90.388	1.273	628.3670	70.9959	0.04
	-800.0	-90.388				
4 ROLL	50.0	5.649	0.775	64.5150	7.2892	0.29
	-50.0	-5.649				
5 YAW	200.0	22.597	1.093	183.0380	20.6805	0.08
	-200.0	-22.597				
6 SIDE	100.0	444.822	1.050	95.2390	423.6442	0.06
	-100.0	-444.822				

MOMENT CENTER =2.950 INCHES AFT OF CENTERLINE OF FORWARD DOWEL
BALANCE VOLTAGE = 5 VOLTS
DELTA W -.436E-02
SPECIAL REMARKS

Figure 61. UT36 8 Page Calibration Summary, 1 of 8

* N A S A * * * * * * * * * * * * * * * * * * *
* * * * * * * * * * * * * * * * Langley Research Center * * * * * * * * * * * * * * * * * *

STRAIN GAGE BALANCE CALIBRATION RESULTS

Balance: **UT36** Engineer: RHEW
Calibration Date: **01/22/96**

	Normal	Axial	Pitch	Roll	Yaw	Side
(1) Nominal Bridge Resistance(Ohms)	120	120	120	120	120	120
(2) Color Codes						
A- Pos. Input	Red	Red	Red	Red	Red	Red
B- Neg. Output	White	White	White	White	White	White
C- Neg. Input	Black	Black	Black	Black	Black	Black
D- Pos. Output	Yellow	Green	Orange	Brown	Purple	Blue
(3) Deflection constants (min/lb or min/in-lb)	0.0200	0.0000	0.0425	0.3600	0.0600	0.0200
(4) Deflection constants (min/N or min/Nm)	0.0045	0.0000	0.3762	3.1863	0.5310	0.0045

LEADS LENGTH = 10 FT
PARALLEL VOLTAGE

Figure 62. UT36 8 Page Calibration Summary, 2 of 8

* * * * * * * * * * * * * * * * * * * N A S A * * * * * * * * * * * * * * * * *
* * * * * * * * * * * * * * Langley Research Center * * * * * * * * * * * * * * *

STRAIN GAGE BALANCE CALIBRATION RESULTS

NORMAL **NORMAL**

Balance: **UT36** Engineer: RHEW
Calibration Date: **01/22/96**

Card Sequence	Components Operated On	Value English	Value S.I.U.	Effect % of Full Scale
	Linear Interaction Coefficients:			
1	normal	1.0000E+00	1.0000E+00	100.00
2	axial			
3	pitch	-5.3797E-03	-2.1180E-01	-4.30
4	roll	-1.6760E-02	-6.5983E-01	-0.84
5	yaw	-4.8829E-04	-1.9224E-02	-0.10
6	side	-1.9670E-03	-1.9670E-03	-0.20
	Nonlinear Coefficients:			
7	normal squared			
8	normal x axial	1.7635E-05	3.9646E-06	0.11
9	normal x pitch			
10	normal x roll			
11	normal x yaw	2.9488E-06	2.6099E-05	0.06
12	normal x side			
13	axial squared			
14	axial x pitch	-4.9870E-06	-4.4139E-05	-0.24
15	axial x roll			
16	axial x yaw			
17	axial x side			
18	pitch squared	-1.1902E-07	-4.1472E-05	-0.08
19	pitch x roll			
20	pitch x yaw			
21	pitch x side			
22	roll squared			
23	roll x yaw	-5.4120E-05	-1.8858E-02	-0.54
24	roll x side	-4.4917E-05	-3.9755E-04	-0.22
25	yaw squared			
26	yaw x side			
27	side squared			

Figure 63. UT36 8 Page Calibration Summary, 3 of 8

* * * * * * * * * * * * * * * * * * * N A S A * * * * * * * * * * * * * * * * * *
* * * * * * * * * * * * * * * Langley Research Center * * * * * * * * * * * * * * * *

STRAIN GAGE BALANCE CALIBRATION RESULTS

AXIAL **AXIAL**

Balance: **UT36** Engineer: RHEW
Calibration Date: **01/22/96**

Card Sequence	Components Operated On	Value English	Value S.I.U.	Effect % of Full Scale
	Linear Interaction Coefficients:			
28	normal	1.6307E-03	1.6307E-03	0.27
29	axial	1.0000E+00	1.0000E+00	100.00
30	pitch	-4.5378E-03	-1.7865E-01	-6.05
31	roll	1.5920E-03	6.2676E-02	0.13
32	yaw	-5.4107E-04	-2.1302E-02	-0.18
33	side	-3.4716E-04	-3.4716E-04	-0.06
	Nonlinear Coefficients:			
34	normal squared	-8.5723E-06	-1.9271E-06	-0.14
35	normal x axial	4.4866E-05	1.0086E-05	0.45
36	normal x pitch	5.2647E-06	4.6597E-05	0.70
37	normal x roll			
38	normal x yaw			
39	normal x side			
40	axial squared	1.9795E-05	4.4501E-06	0.12
41	axial x pitch	1.0477E-06	9.2727E-06	0.08
42	axial x roll			
43	axial x yaw			
44	axial x side	-1.0084E-05	-2.2670E-06	-0.10
45	pitch squared	1.6100E-06	5.6099E-04	1.72
46	pitch x roll			
47	pitch x yaw			
48	pitch x side			
49	roll squared			
50	roll x yaw	-1.3886E-05	-4.8388E-03	-0.23
51	roll x side			
52	yaw squared			
53	yaw x side	7.5488E-06	6.6812E-05	0.25
54	side squared	-1.0223E-05	-2.2982E-06	-0.17

Figure 64. UT36 8 Page Calibration Summary, 4 of 8

* * * * * * * * * * * * * * * * * * * N A S A * * * * * * * * * * * * * * * * * *
* * * * * * * * * * * * * * Langley Research Center * * * * * * * * * * * * * * *

STRAIN GAGE BALANCE CALIBRATION RESULTS

PITCH **PITCH**

Balance: **UT36** Engineer: RHEW
Calibration Date: **01/22/96**

Card Sequence	Components Operated On	Value English	Value S.I.U.	Effect % of Full Scale
	Linear Interaction Coefficients:			
55	normal	-5.4956E-03	-1.3959E-04	-0.07
56	axial	-9.3639E-03	-2.3784E-04	-0.07
57	pitch	1.0000E+00	1.0000E+00	100.00
58	roll	-1.7104E-02	-1.7104E-02	-0.11
59	yaw			
60	side			
	Nonlinear Coefficients:			
61	normal squared			
62	normal x axial			
63	normal x pitch	5.7412E-06	1.2907E-06	0.06
64	normal x roll			
65	normal x yaw			
66	normal x side			
67	axial squared	1.4238E-04	8.1298E-07	0.06
68	axial x pitch	-1.0917E-05	-2.4541E-06	-0.07
69	axial x roll			
70	axial x yaw			
71	axial x side			
72	pitch squared			
73	pitch x roll			
74	pitch x yaw			
75	pitch x side			
76	roll squared			
77	roll x yaw	-4.8938E-05	-4.3314E-04	-0.06
78	roll x side			
79	yaw squared			
80	yaw x side			
81	side squared			

Figure 65. UT36 8 Page Calibration Summary, 5 of 8

* * * * * * * * * * * * * * * * * * * N A S A * * * * * * * * * * * * * * * * * *
* * * * * * * * * * * * * * Langley Research Center * * * * * * * * * * * * * * * * *

STRAIN GAGE BALANCE CALIBRATION RESULTS

ROLL **ROLL**

Balance: **UT36** Engineer: RHEW
Calibration Date: **01/22/96**

Card Sequence	Components Operated On	Value English	Value S.I.U.	Effect % of Full Scale
	Linear Interaction Coefficients:			
82	normal			
83	axial			
84	pitch			
85	roll	1.0000E+00	1.0000E+00	100.00
86	yaw	6.8140E-03	6.8140E-03	2.73
87	side	-5.9245E-03	-1.5048E-04	-1.18
	Nonlinear Coefficients:			
88	normal squared			
89	normal x axial			
90	normal x pitch	-4.5960E-07	-1.0332E-07	-0.07
91	normal x roll	6.6530E-06	1.4956E-06	0.07
92	normal x yaw	-4.1224E-06	-9.2676E-07	-0.16
93	normal x side	-5.3581E-06	-3.0595E-08	-0.11
94	axial squared			
95	axial x pitch	-4.7293E-06	-1.0632E-06	-0.45
96	axial x roll	1.5345E-05	3.4497E-06	0.09
97	axial x yaw			
98	axial x side			
99	pitch squared	1.2328E-07	1.0912E-06	0.16
100	pitch x roll			
101	pitch x yaw	-1.9724E-06	-1.7457E-05	-0.63
102	pitch x side	1.0685E-05	2.4020E-06	1.71
103	roll squared			
104	roll x yaw			
105	roll x side			
106	yaw squared			
107	yaw x side			
108	side squared	-4.5348E-06	-2.5894E-08	-0.09

Figure 66. UT36 8 Page Calibration Summary, 6 of 8

* * * * * * * * * * * * * * * * * * * N A S A * * * * * * * * * * * * * * * * * *
* * * * * * * * * * * * * * * Langley Research Center * * * * * * * * * * * * * * * *

STRAIN GAGE BALANCE CALIBRATION RESULTS

YAW **YAW**

Balance: **UT36** Engineer: RHEW
Calibration Date: **01/22/96**

Card Sequence	Components Operated On	Value English	Value S.I.U.	Effect % of Full Scale
	Linear Interaction Coefficients:			
109	normal	1.6691E-03	4.2394E-05	0.08
110	axial			
111	pitch			
112	roll	1.0836E-02	1.0836E-02	0.27
113	yaw	1.0000E+00	1.0000E+00	100.00
114	side	-1.7342E-02	-4.4049E-04	-0.87
	Nonlinear Coefficients:			
115	normal squared			
116	normal x axial			
117	normal x pitch			
118	normal x roll	5.9565E-05	1.3391E-05	0.15
119	normal x yaw			
120	normal x side			
121	axial squared	6.9387E-05	3.9621E-07	0.12
122	axial x pitch			
123	axial x roll			
124	axial x yaw	-1.9674E-05	-4.4229E-06	-0.12
125	axial x side			
126	pitch squared			
127	pitch x roll	4.9087E-05	4.3445E-04	0.98
128	pitch x yaw	-8.0273E-07	-7.1047E-06	-0.06
129	pitch x side			
130	roll squared			
131	roll x yaw			
132	roll x side			
133	yaw squared			
134	yaw x side			
135	side squared			

Figure 67. UT36 8 Page Calibration Summary, 7 of 8

* N A S A * * * * * * * * * * * * * * * * * * *
* * * * * * * * * * * * * * * * Langley Research Center * * * * * * * * * * * * * * * * * *

STRAIN GAGE BALANCE CALIBRATION RESULTS

SIDE **SIDE**

Balance: **UT36** Engineer: RHEW
Calibration Date: **01/22/96**

Card Sequence	Components Operated On	Value English	Value S.I.U.	Effect % of Full Scale
	Linear Interaction Coefficients:			
136	normal	4.8717E-03	4.8717E-03	0.49
137	axial			
138	pitch	-3.0045E-04	-1.1829E-02	-0.24
139	roll	1.2785E-03	5.0333E-02	0.06
140	yaw	-6.2753E-03	-2.4706E-01	-1.26
141	side	1.0000E+00	1.0000E+00	100.00
	Nonlinear Coefficients:			
142	normal squared			
143	normal x axial			
144	normal x pitch			
145	normal x roll	4.7951E-05	4.2440E-04	0.24
146	normal x yaw			
147	normal x side			
148	axial squared	1.9919E-05	4.4780E-06	0.07
149	axial x pitch			
150	axial x roll			
151	axial x yaw	-7.9635E-06	-7.0483E-05	-0.10
152	axial x side	1.8295E-05	4.1128E-06	0.11
153	pitch squared			
154	pitch x roll	3.7858E-05	1.3192E-02	1.51
155	pitch x yaw	-3.3899E-07	-1.1812E-04	-0.05
156	pitch x side			
157	roll squared			
158	roll x yaw			
159	roll x side			
160	yaw squared			
161	yaw x side			
162	side squared			

Figure 68. UT36 8 Page Calibration Summary, 8 of 8

G. Off-Center System CAD Drawings

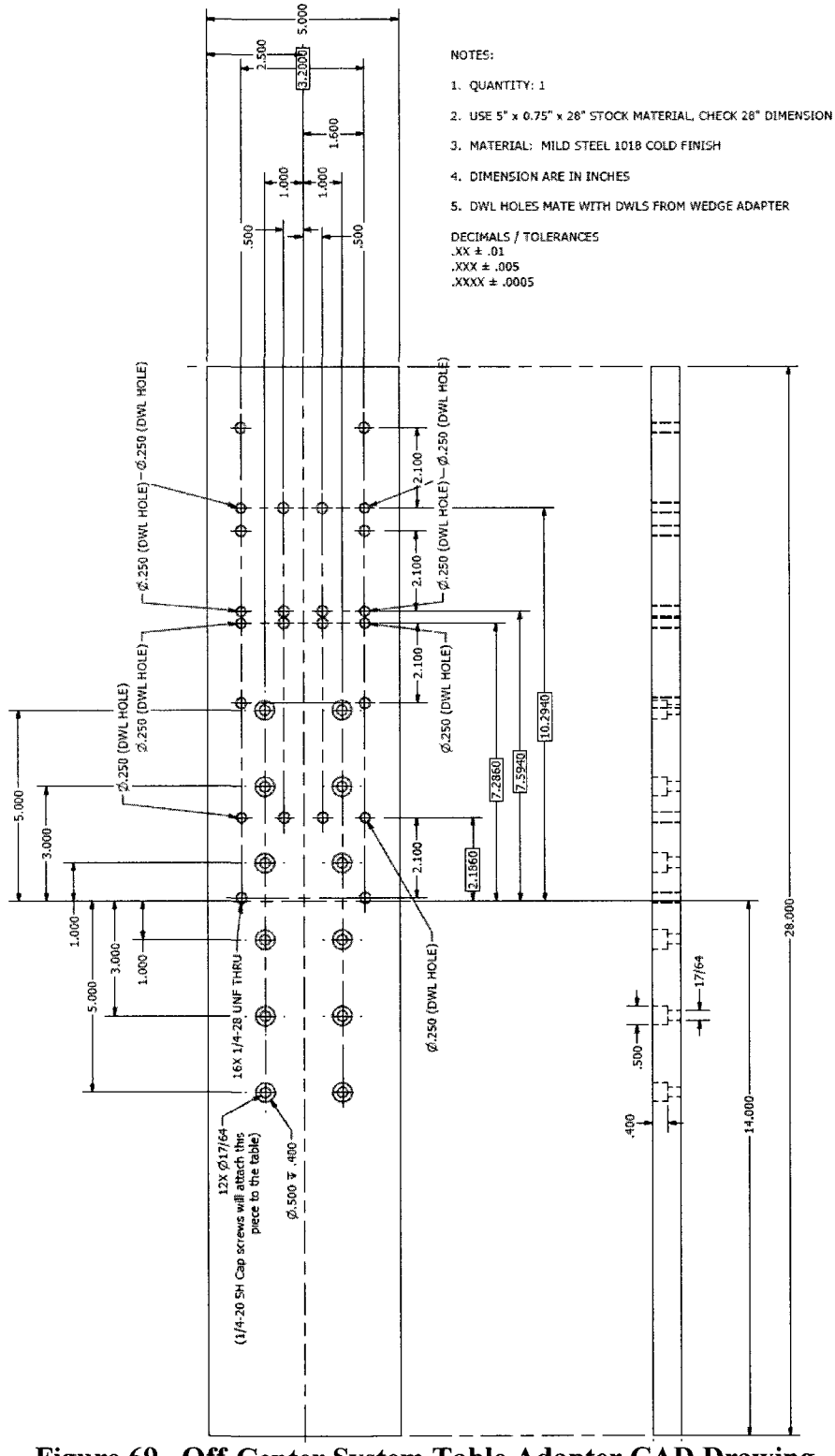

Figure 69. Off-Center System Table Adapter CAD Drawing

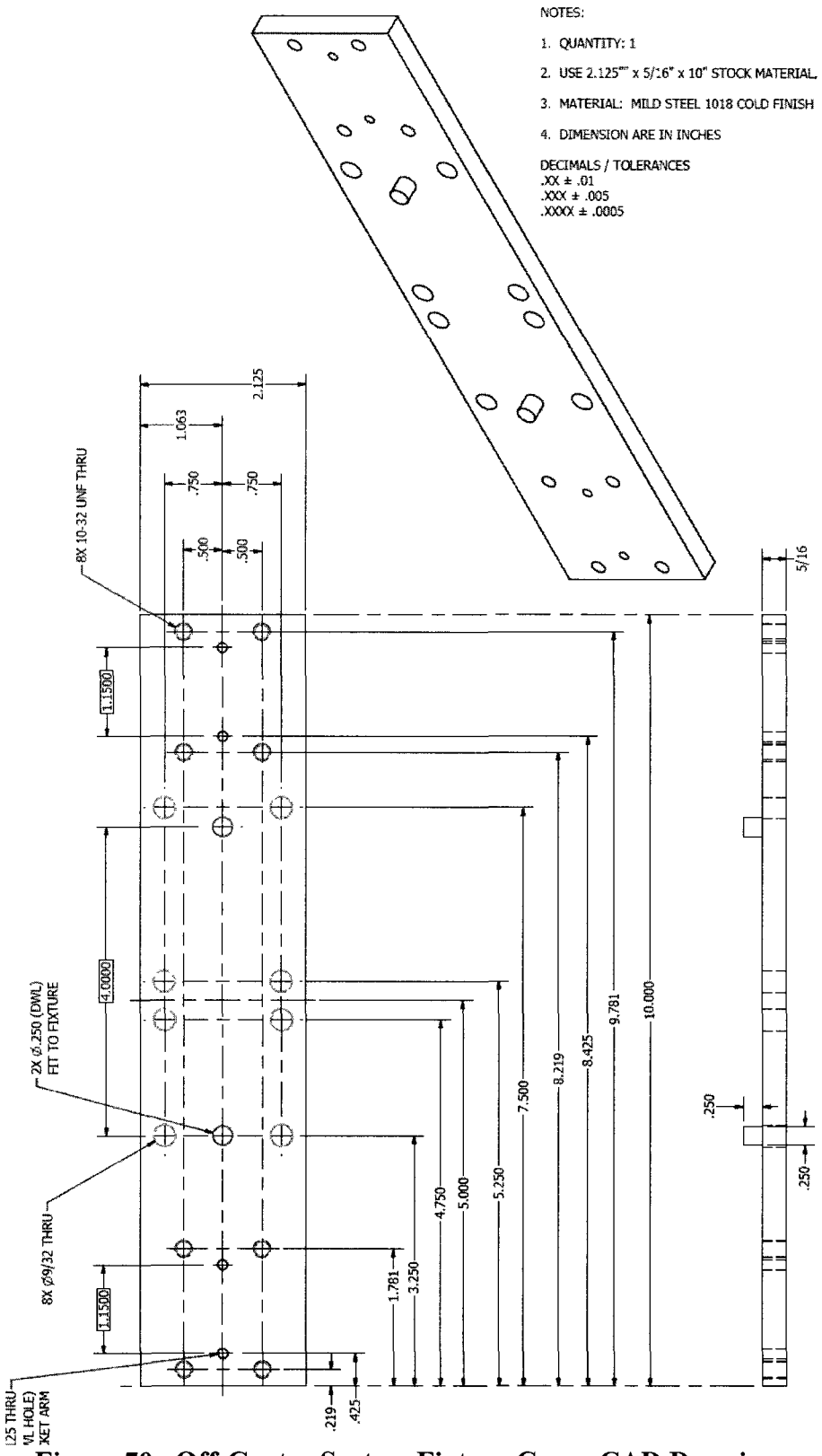

Figure 70. Off-Center System Fixture Cover CAD Drawing

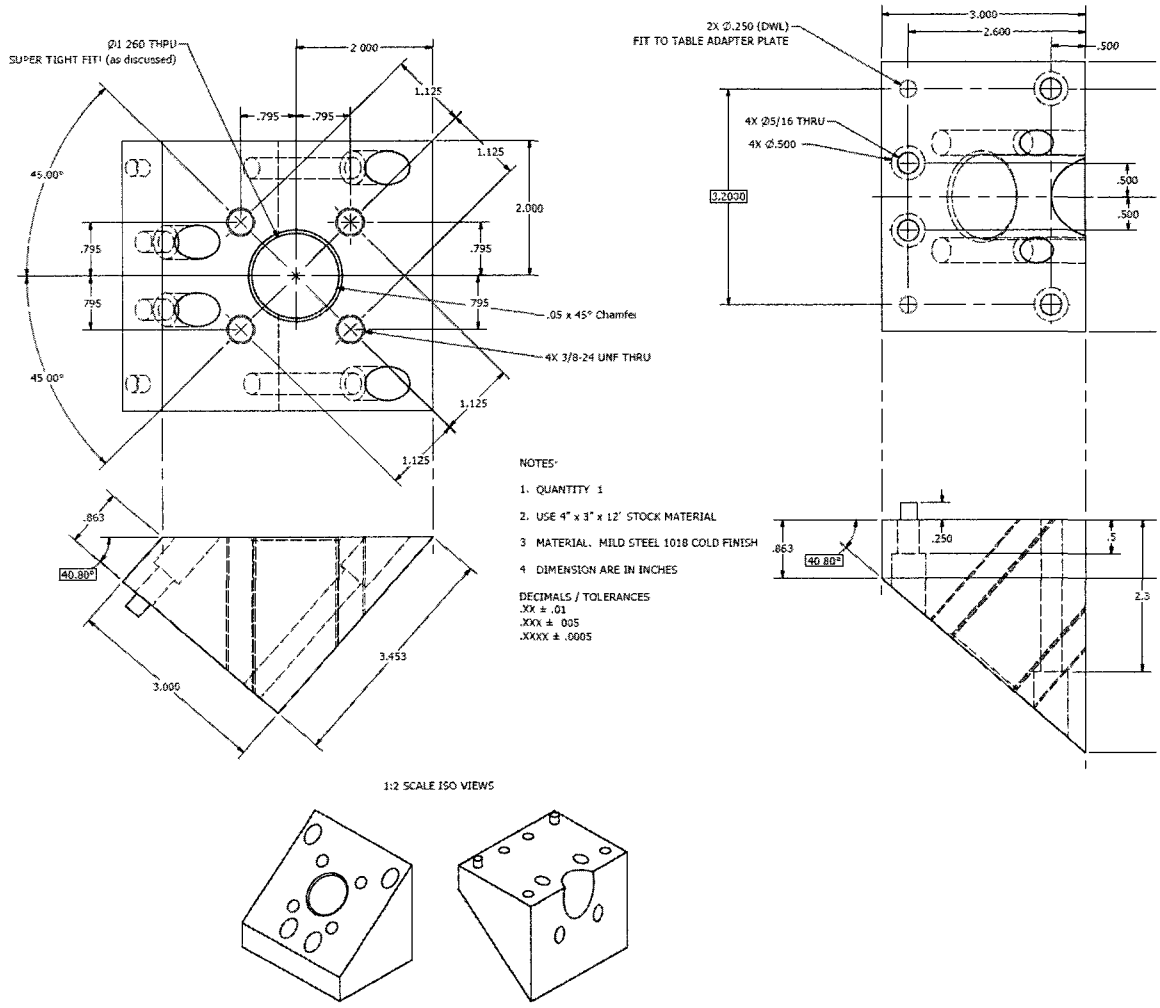

Figure 71. Off-Center System Wedge Adapter CAD Drawing, 1 of 2

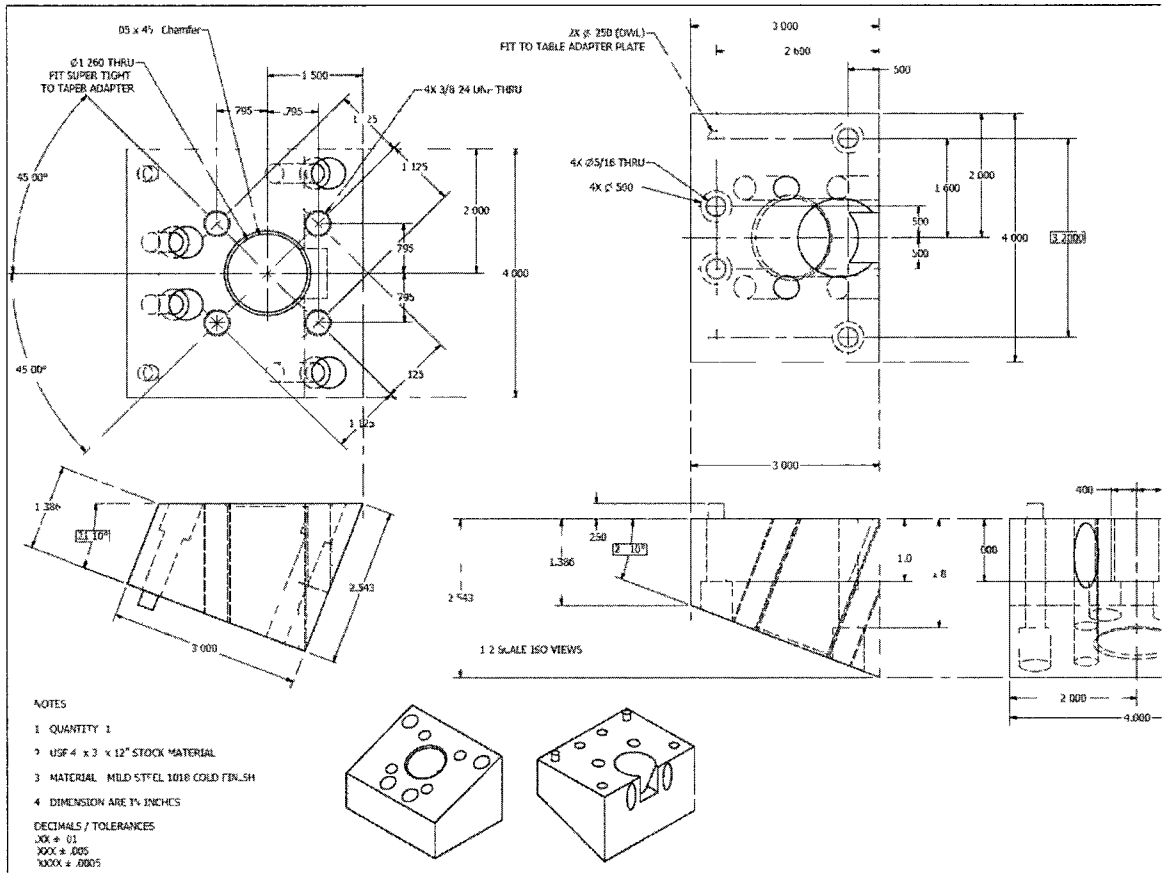

Figure 72. Off-Center System Wedge Adapter CAD Drawing, 2 of 2

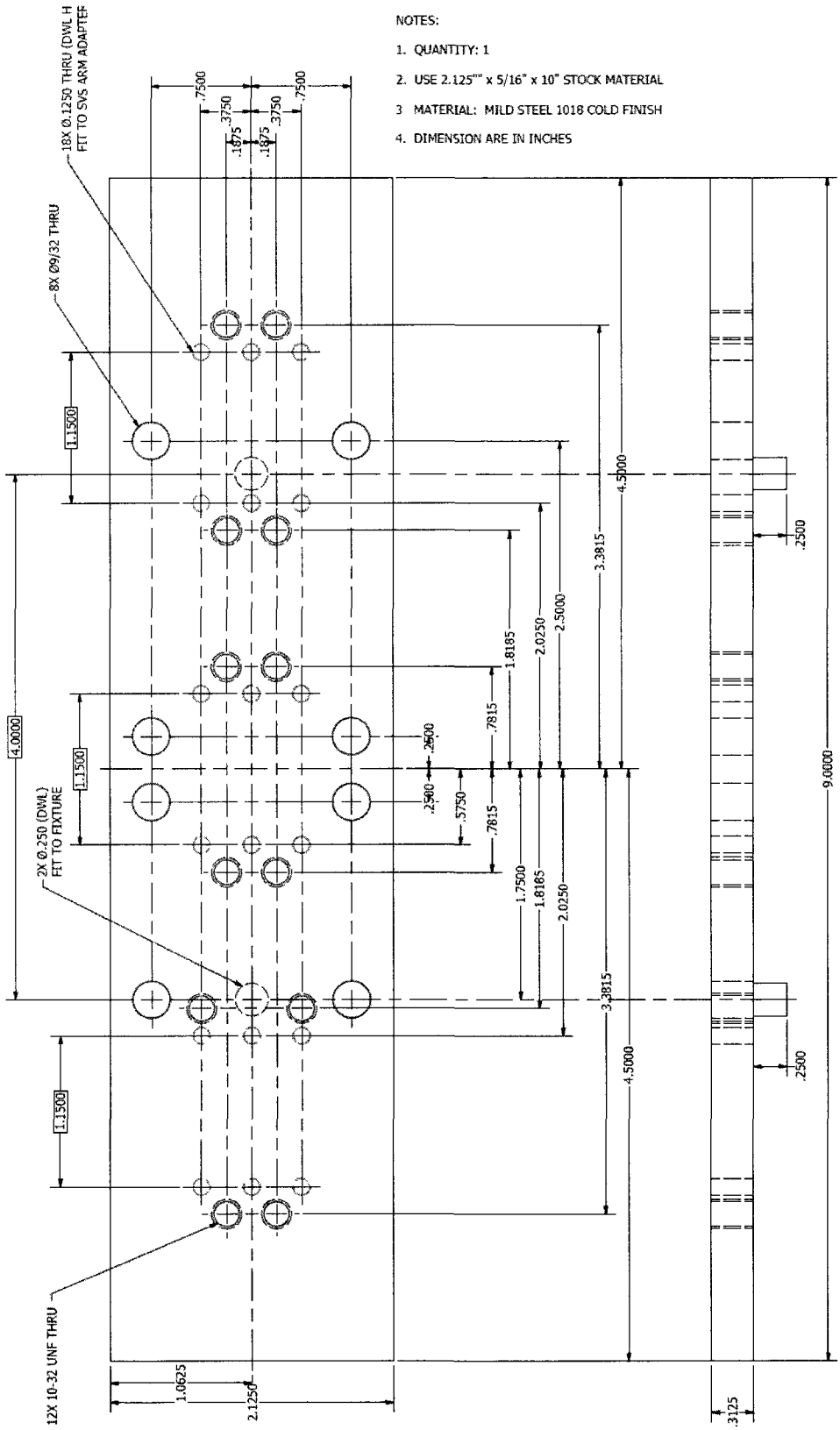

Figure 73. UT36 SVS Load Template CAD Drawing

H. Iterative Inverse Prediction Method

A forward model traditionally models bridge output as a function of applied loads; however, for practical applications, a researcher requires the applied loads as a function of bridge output. The method required to swap this functional relationship is called the classical iterative inverse prediction method. While there are other methods, the iterative inverse method is the preferred technique used at NASA LaRC and is therefore adopted in this research. To demonstrate this method consider a two component force balance with a forward model that predicts bridge output (y_{NF} , y_{AF}) as a function of normal force or axial force (x_{NF} , x_{AF}) shown in equations (48) and (49).

$$y_{NF} = \beta_{0,NF} + \beta_{1,NF}x_{NF} + \beta_{2,NF}x_{AF} + \beta_{11,NF}x_{NF}^2 + \beta_{22,NF}x_{AF}^2 + \beta_{12,NF}x_{NF}x_{AF} + \epsilon_{NF} \tag{48}$$

$$y_{AF} = \beta_{0,AF} + \beta_{1,AF}x_{NF} + \beta_{2,AF}x_{AF} + \beta_{11,AF}x_{NF}^2 + \beta_{22,AF}x_{AF}^2 + \beta_{12,AF}x_{NF}x_{AF} + \epsilon_{AF} \tag{49}$$

Here, y_{NF} is primarily a function of x_{NF}; therefore, $\beta_{1,NF}$ is the dominant coefficient, often referred to as the sensitivity. To estimate x_{NF} and x_{AF} we invert the forward equations to obtain equations (50) and (51).

$$\hat{x}_{NF} = \frac{y_{NF} - \hat{\beta}_{0,NF} - \hat{\beta}_{2,NF}x_{AF} - \hat{\beta}_{11,NF}x_{NF}^2 - \hat{\beta}_{22,NF}x_{AF}^2 - \hat{\beta}_{12,NF}x_{NF}x_{AF}}{\hat{\beta}_{1,NF}} \tag{50}$$

$$\hat{x}_{AF} = \frac{y_{AF} - \hat{\beta}_{0,AF} - \hat{\beta}_{1,AF}x_{NF} - \hat{\beta}_{11,AF}x_{NF}^2 - \hat{\beta}_{22,AF}x_{AF}^2 - \hat{\beta}_{12,AF}x_{NF}x_{AF}}{\hat{\beta}_{2,AF}} \quad (51)$$

Therefore, we see that a simultaneous iterative solution of the two inverse equations is required. In general, an iterative solution is employed as follows.

$$Corrected\ Load = Uncorrected\ Load - \sum(Interactions) \quad (52)$$

Let subscript u and c denote uncorrected and corrected load, respectively, with the hat notation omitted for clarity as shown in equations (53) and (54).

$$x_{NFu} = \frac{y_{NF} - \hat{\beta}_{0,NF}}{\hat{\beta}_{1,NF}} \quad (53)$$

$$x_{AFu} = \frac{y_{AF} - \hat{\beta}_{0,AF}}{\hat{\beta}_{2,AF}} \quad (54)$$

To begin the iteration at step zero, the sum of the interactions for each component are shown in equations (55) through (58).

$$\sum(Interactions)_{NF} = \frac{\hat{\beta}_{2,NF}x_{AFu} - \hat{\beta}_{11,NF}x_{NFu}^2 - \hat{\beta}_{22,NF}x_{AFu}^2 - \hat{\beta}_{12,NF}x_{NFu}x_{AFu}}{\hat{\beta}_{1,NF}} \quad (55)$$

$$\sum(Interactions)_{AF} = \frac{\hat{\beta}_{1,AF}x_{NFu} - \hat{\beta}_{11,AF}x_{NFu}^2 - \hat{\beta}_{22,AF}x_{AFu}^2 - \hat{\beta}_{12,AF}x_{NFu}x_{AFu}}{\hat{\beta}_{2,AF}} \quad (56)$$

$$x_{NFc} = x_{NFu} - \sum(Interactions)_{NF} \quad (57)$$

$$x_{AFc} = x_{AFu} - \sum(Interactions)_{AF} \quad (58)$$

Then, for iteration step one to convergence, the sum of interactions are shown in equations (59) and (60).

$$\sum(Interactions)_{NF} = \frac{\hat{\beta}_{2,NF}x_{AFc} - \hat{\beta}_{11,NF}x_{NFc}^2 - \hat{\beta}_{22,NF}x_{AFc}^2 - \hat{\beta}_{12,NF}x_{NFc}x_{AFc}}{\hat{\beta}_{1,NF}} \quad (59)$$

$$\sum(Interactions)_{AF} = \frac{\hat{\beta}_{1,AF}x_{NFc} - \hat{\beta}_{11,AF}x_{NFc}^2 - \hat{\beta}_{22,AF}x_{AFc}^2 - \hat{\beta}_{12,AF}x_{NFc}x_{AFc}}{\hat{\beta}_{2,AF}} \quad (60)$$

For balance applications, convergence is usually obtained within five iterations. This theoretical example was extended so that the UT-36 balance loads were calculated using

the 27 x 6 calibration matrix shown in table 42. The code written to implement the inverse prediction method is shown below.

```
function [loads] = quad_calc_ut36_loadsB(sigs)
    FSL=[100 60 800 50 200 100];%[NF AF PM RM YM SF]
    sens=[102.3420 58.5210 628.3670 64.5150 183.0380
95.2390];%lb/(mV/V)
    cmat=xlsread('\UT36calmat.xls');%coefficients from cal summary
    for i=1:6
        cmat(i,i)=0;%get rid of diagonal 1's
    end
    for i=1:27
        cm(i,:)=cmat(i,:).*FSL./sens;%normalize cal matrix
    end
    sigs=sigs/1E3;
    [q w]=size(sigs);
    for i=1:q
        uncldS = sens .* sigs(i,:);
        tom=1;
        for j = 1:8                    % performs 8 iterations
            if j==1; corlds = uncldS; end;
            em = quad_expdesmat(corlds);
            intcor = em * cm;
            corlds = uncldS - intcor;
        end;
        loads(i,:) = corlds;
    end
end
```

Table 42. 27 x 6 UT36 Calibration Matrix

Term #	NF	AF	PM	RM	YM	SF
1	1.000E+00	1.631E-03	-5.496E-03	0.000E+00	1.669E-03	4.872E-03
2	0.000E+00	1.000E+00	-9.364E-03	0.000E+00	0.000E+00	0.000E+00
3	-5.380E-03	-4.538E-03	1.000E+00	0.000E+00	0.000E+00	-3.005E-04
4	-1.676E-02	1.592E-03	-1.710E-02	1.000E+00	1.084E-02	1.279E-03
5	-4.883E-04	-5.411E-04	0.000E+00	6.814E-03	1.000E+00	-6.275E-03
6	-1.967E-03	-3.472E-04	0.000E+00	-5.925E-03	-1.734E-02	1.000E+00
7	0.000E+00	-8.572E-06	0.000E+00	0.000E+00	0.000E+00	0.000E+00
8	1.764E-05	4.487E-05	0.000E+00	0.000E+00	0.000E+00	0.000E+00
9	0.000E+00	5.265E-06	5.741E-06	-4.596E-07	0.000E+00	0.000E+00
10	0.000E+00	0.000E+00	0.000E+00	6.653E-06	5.957E-05	4.795E-05
11	2.949E-06	0.000E+00	0.000E+00	-4.122E-06	0.000E+00	0.000E+00
12	0.000E+00	0.000E+00	0.000E+00	-5.358E-06	0.000E+00	0.000E+00
13	0.000E+00	1.980E-05	1.424E-04	0.000E+00	6.939E-05	1.992E-05
14	-4.987E-06	1.048E-06	-1.092E-05	-4.729E-06	0.000E+00	0.000E+00
15	0.000E+00	0.000E+00	0.000E+00	1.535E-05	0.000E+00	0.000E+00
16	0.000E+00	0.000E+00	0.000E+00	0.000E+00	-1.967E-05	-7.964E-06
17	0.000E+00	-1.008E-05	0.000E+00	0.000E+00	0.000E+00	1.830E-05
18	-1.190E-07	1.610E-06	0.000E+00	1.233E-07	0.000E+00	0.000E+00
19	0.000E+00	0.000E+00	0.000E+00	0.000E+00	4.909E-05	3.786E-05
20	0.000E+00	0.000E+00	0.000E+00	-1.972E-06	-8.027E-07	-3.390E-07
21	0.000E+00	0.000E+00	0.000E+00	1.069E-05	0.000E+00	0.000E+00
22	0.000E+00	0.000E+00	0.000E+00	0.000E+00	0.000E+00	0.000E+00
23	-5.412E-05	-1.389E-05	-4.894E-05	0.000E+00	0.000E+00	0.000E+00
24	-4.492E-05	0.000E+00	0.000E+00	0.000E+00	0.000E+00	0.000E+00
25	0.000E+00	0.000E+00	0.000E+00	0.000E+00	0.000E+00	0.000E+00
26	0.000E+00	7.549E-06	0.000E+00	0.000E+00	0.000E+00	0.000E+00
27	0.000E+00	-1.022E-05	0.000E+00	-4.535E-06	0.000E+00	0.000E+00

I. VACS Calibration Models

Table 43 shows the calibration matrix calculated from the factorial calibration experiments. The seven by three calibration matrix represents three calibration models with seven model terms each. The rows of the matrix indicate the type of coefficient. The calibration models are forward models, meaning that they estimate the balance electrical output as a function of applied loads. In this case, the applied loads are the loads predicted using the governing equations. Each entry in the matrix is a coefficient for the normal force, axial force or pitching moment model. The calibration coefficients are in units of $(\frac{\mu V}{V})/(load)$, where $load$ is the amount of NF, AF or PM applied in coded units (-1 to +1), and $load$ is a unitless quantity.

Table 43. Forward Calibration Matrices for Each System

	Centered System			Off-Center System		
	NF	AF	PM	NF	AF	PM
Int	0.176	219.484	-0.263	0.044	-0.003	-0.012
NF	291.806	1.413	-1.511	290.315	0.647	-0.212
AF	-0.019	118.242	0.002	-0.249	337.740	-0.016
PM	-6.125	-9.129	187.877	-6.254	-9.047	188.892
NF*AF	0.661	0.206	-0.637	0.819	2.017	0.650
NF*PM	0.253	-1.240	-0.162	0.000	-0.590	-0.001
AF*PM	0.268	0.000	-0.223	0.242	0.000	0.062

The sensitivities are calculated from the calibration models and compared to the sensitivities estimated from the previous calibration of the UT-36 using a manual stand system.

Table 44. Comparison of Sensitivities

	NF (lbs/mV/V)	AF (lbs/mV/V)	PM (inlbs/mV/V)
Centered System	103.34	59.20	638.72
Off-Center System Sensitivities	102.28	59.22	635.23
1995 Sensitivities	102.34	58.52	628.37

Table 45 compares the full scale effects of the calibration coefficients. The full scale effects show the percent contribution of each model term compared to the primary sensitivities. Similar to the results seen from the previous UT-36 calibration, axial force shows the most interaction with other components, while pitching moment shows least interaction. The similarities between the calculated calibration models and the calibration model estimated from the previous calibration are encouraging; however, the applied load error is too large for the new calibration models to be effective. The centered system pitching moment interaction in the axial force model is markedly different than the off-center system pitching moment interaction in the axial force model (-7.72 $(\frac{\mu V}{V})/(load)$ vs. -2.679 $(\frac{\mu V}{V})/(load)$). This may be due to the large tare load experienced by the off-center system, meaning that these interactions are estimated at different locations in balance load space.

Table 45. Centered System Comparison of Full Scale Effects

	Centered System			1995 Coefficients		
	NF	AF	PM	NF	AF	PM
NF	100.00	1.20	-0.80	100.00	0.27	-0.07
AF	-0.01	100.00	0.00	0.00	100.000	-0.07
PM	-2.10	-7.72	100.00	-4.30	-6.05	100.000
NF*AF	0.23	0.17	-0.34	0.11	0.45	0.00
NF*PM	0.09	-1.05	-0.09	0.00	0.70	0.06
AF*PM	0.09	0.00	-0.12	-0.24	0.08	-0.07

Table 46. Off-Center System Comparison of Full Scale Effects

	Off-Center System			1995 Coefficients		
	NF	AF	PM	NF	AF	PM
NF	100.000	0.192	-0.112	100.00	0.27	-0.07
AF	-0.086	100.000	-0.008	0.00	100.000	-0.07
PM	-2.154	-2.679	100.000	-4.30	-6.05	100.000
NF*AF	0.282	0.597	0.344	0.11	0.45	0.00
NF*PM	0.000	-0.175	0.000	0.00	0.70	0.06
AF*PM	0.083	0.000	0.033	-0.24	0.08	-0.07

J. Finite Element Analysis of Centered System Arm Assembly

The structure investigated is a simplified representation of the fixture cover and arm assembly for the centered system. This structure represents the upper portion of the fixture cover. Approximately 9000 nodes and 1700 elements were used to construct the mesh shown in figure 74. The bottom face of the fixture cover has a fixed support boundary condition as shown in figure 75. The bottom face represents the location where the fixture cover is bolted to the balance fixture. It is assumed that only the section above the fasteners is subject to deflection; hence, the section below the fasteners is not modeled. The force is applied on the face of the end of the cylindrical arm. The force applied represents the worst case loading scenario, which is 30 lbs of centrifugal force combined with 8 lbs of gravitational force, as shown in figure 75. As expected, it is shown that the maximum principal stress is far below the yield strength of steel, as shown in figure 76. From the deflection results shown in figure 77, the maximum uncertainty angle u_ϕ is calculated as the inverse tangent of the max deflection distance, divided by the un-deformed length of the arm, which is approximately 0.05 degrees.

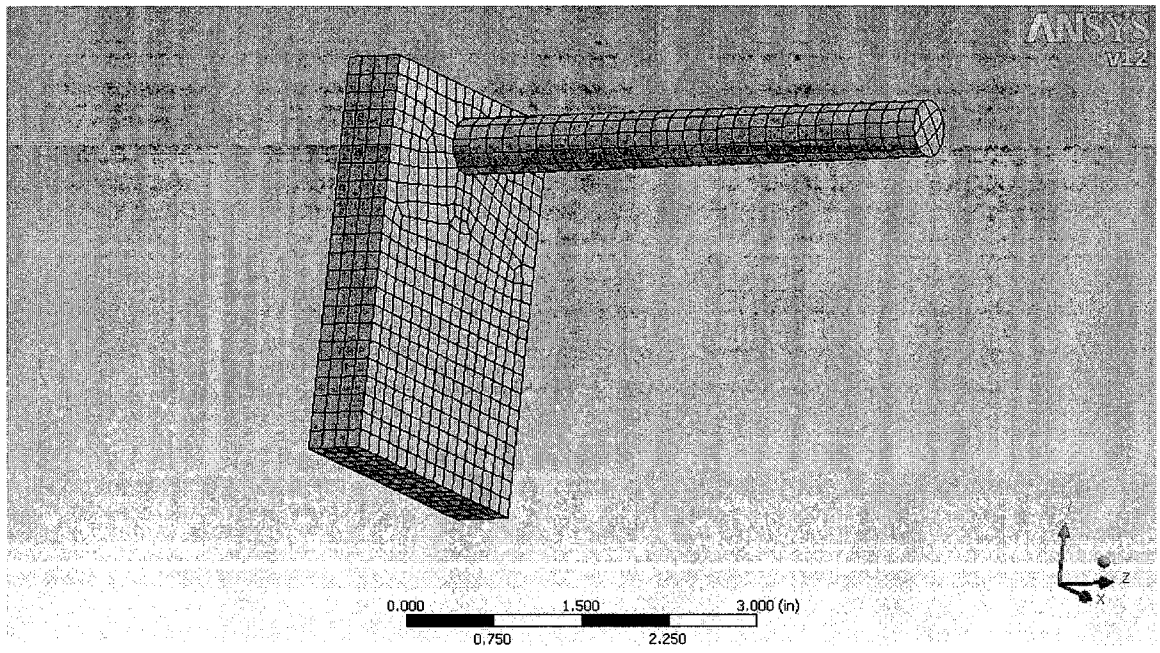

Figure 74. Mesh for the FEA Sizing Analysis

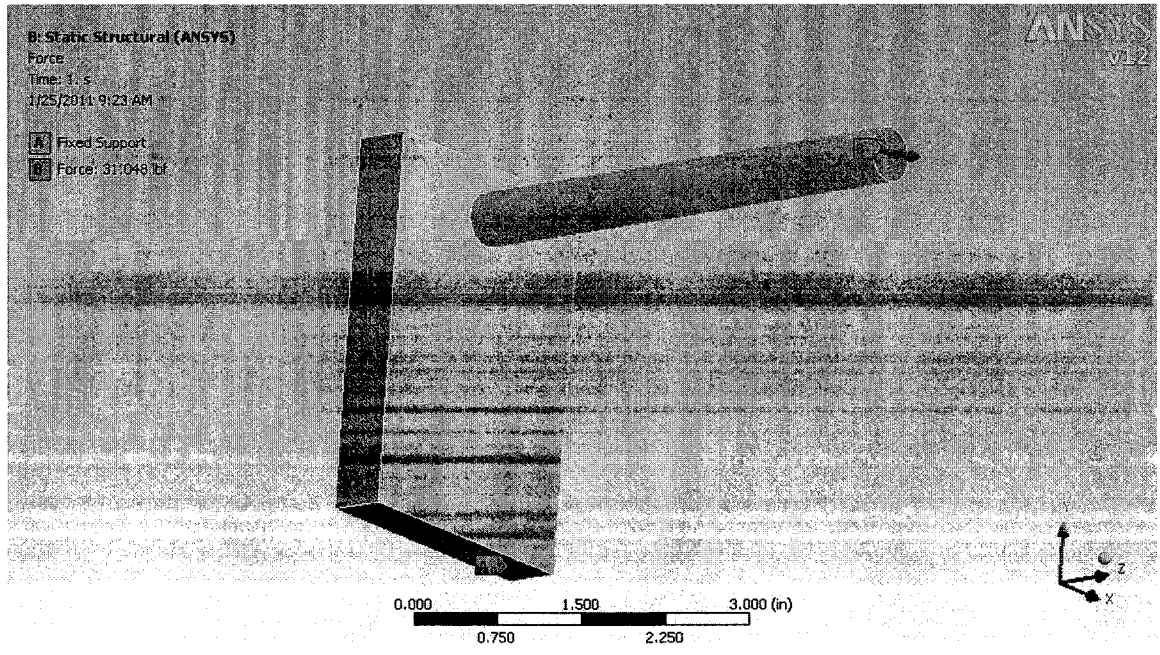

Figure 75. Boundary Conditions

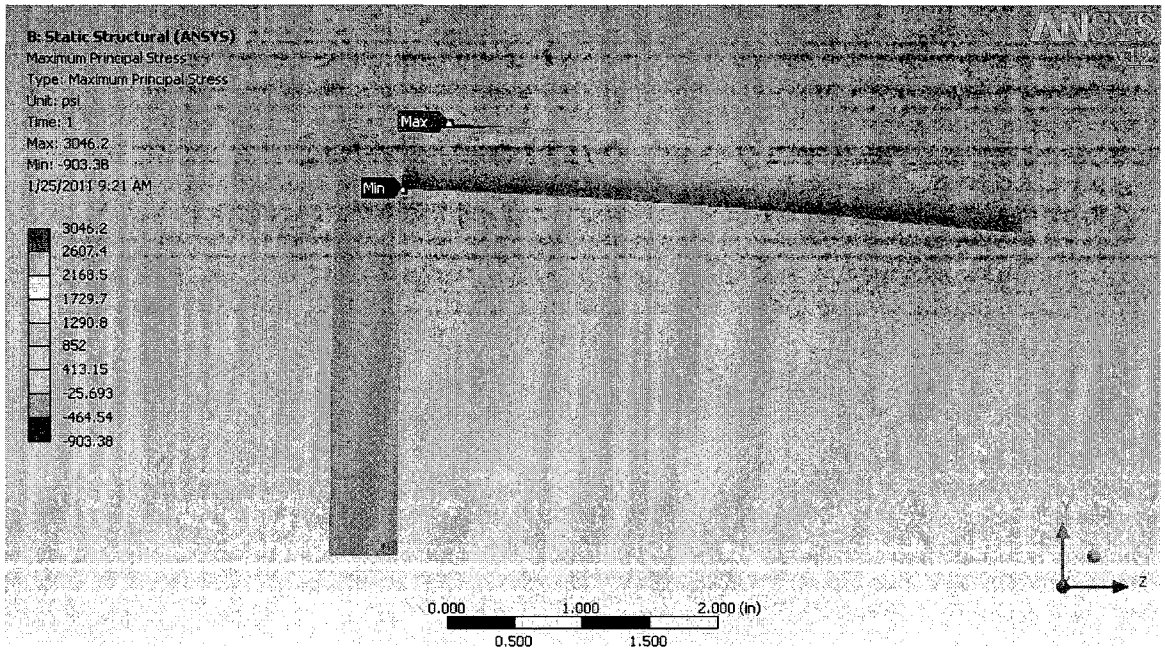

Figure 76. Maximum Principal Stress

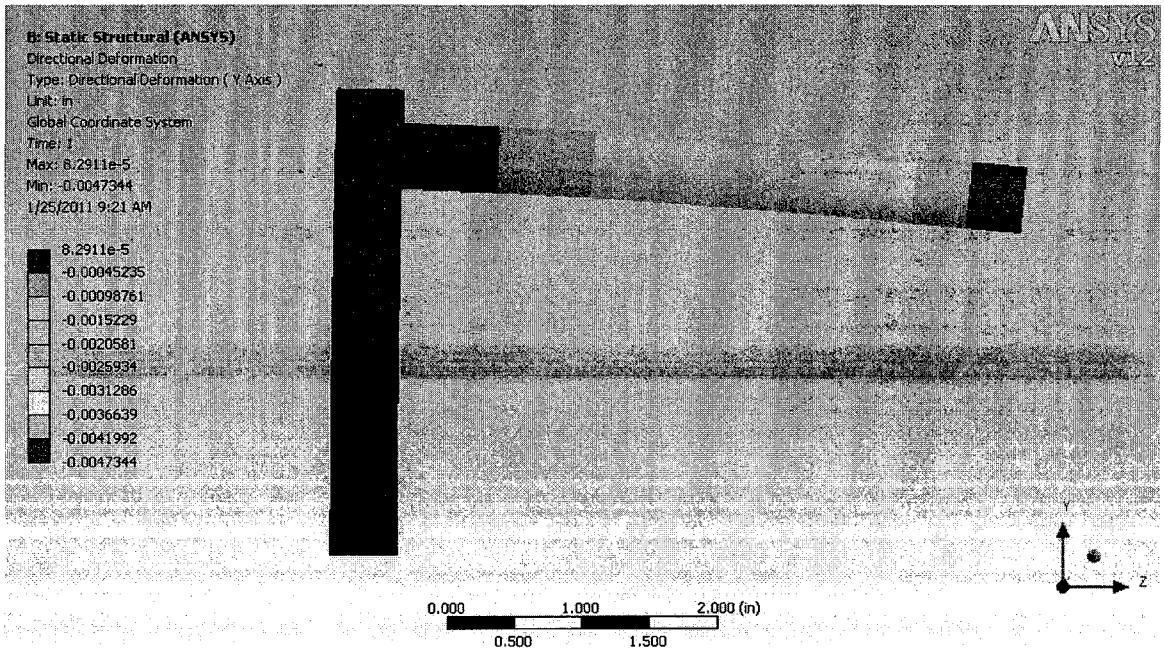

Figure 77. Directional Deformation (Y Axis)

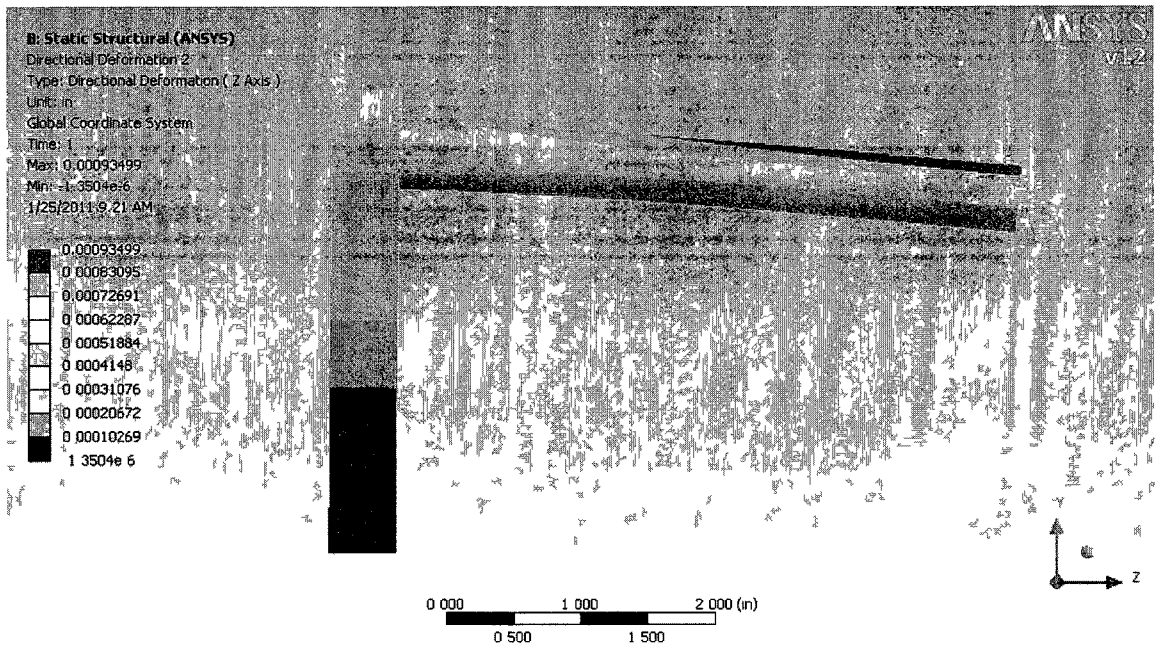

Figure 78. Directional Deformation (Z Axis)

K. Additional Residual Plots

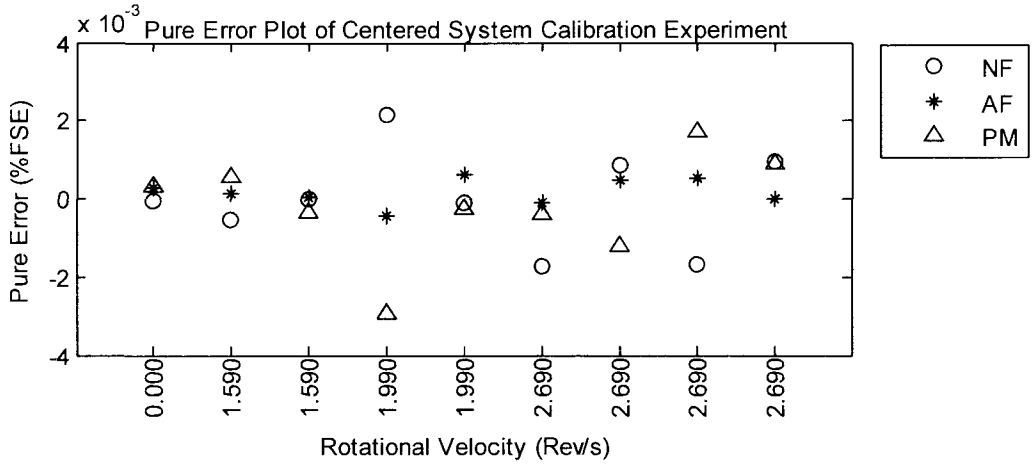

Figure 79. Centered System Rotational Velocity vs. Pure Error

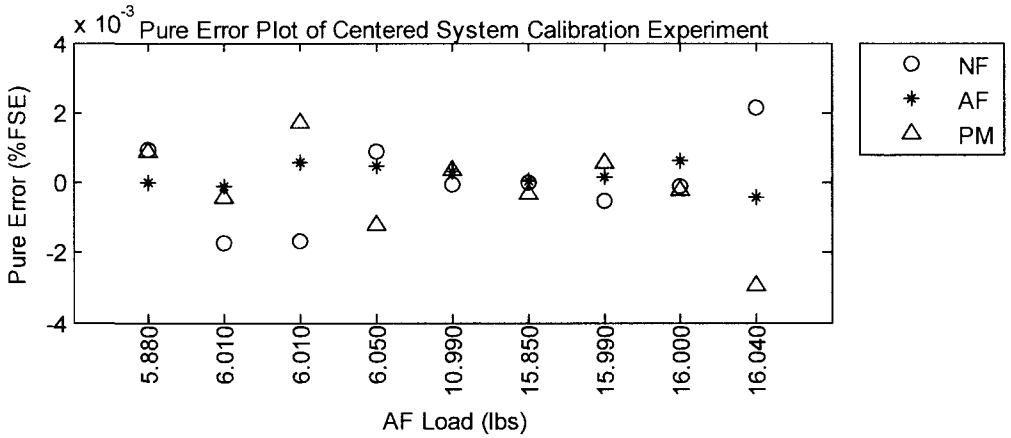

Figure 80. Centered System Axial Force vs. Pure Error

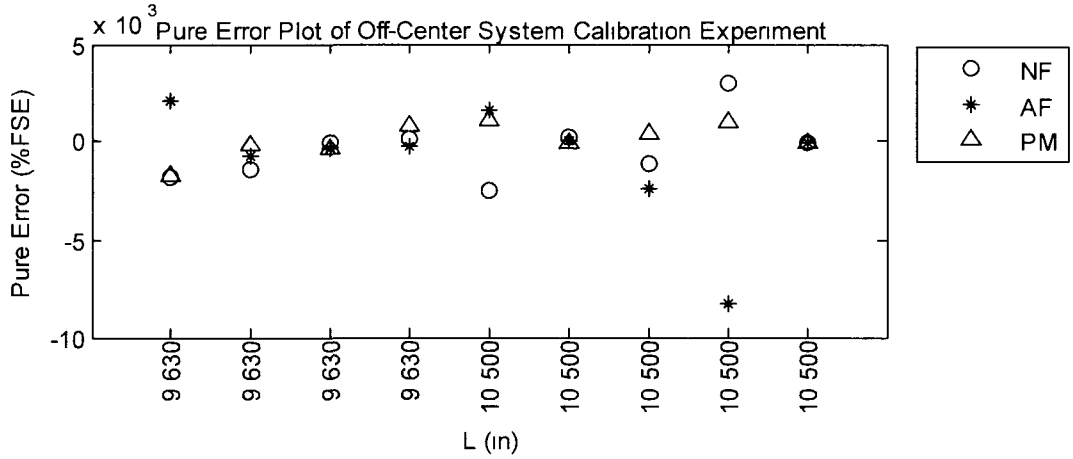

Figure 81. Off-Center System L distance vs. Pure Error

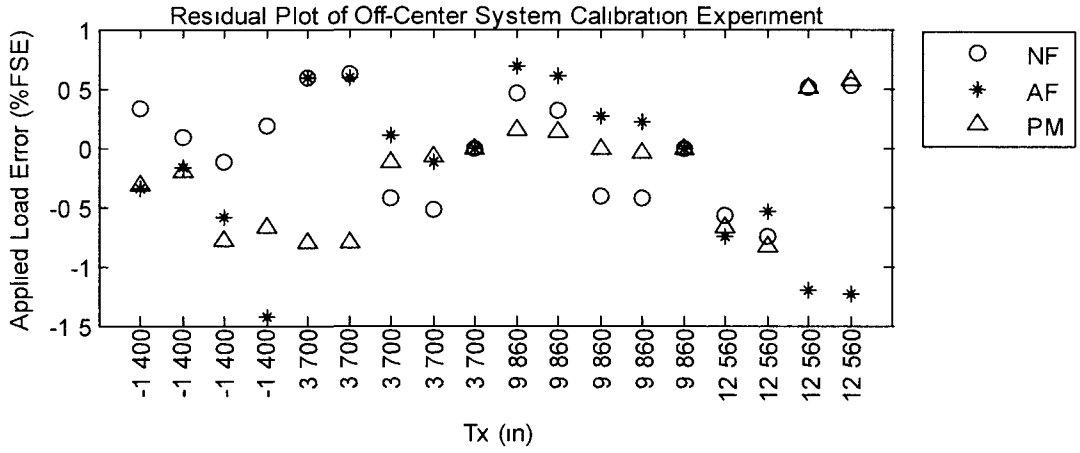

Figure 82. Off-Center System Tx Distance vs. Applied Load Error

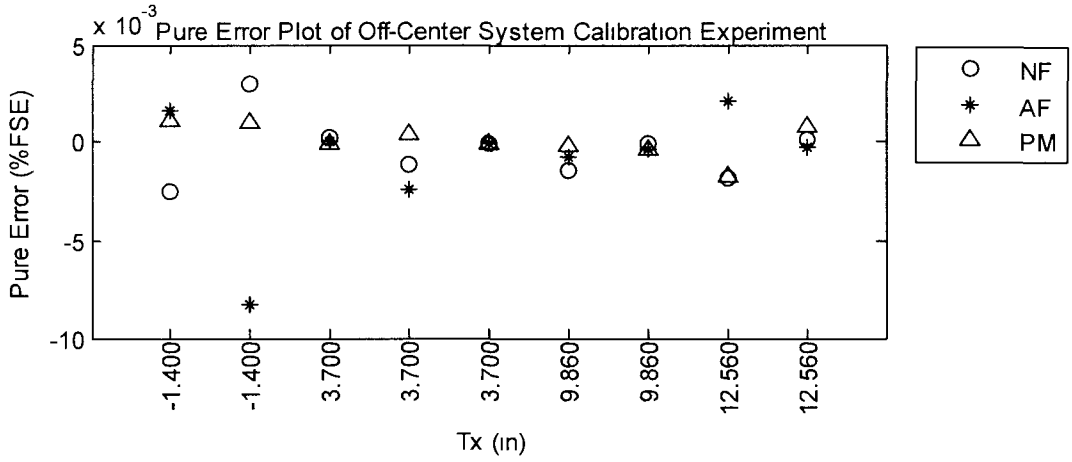

Figure 83. Centered System Tx Distance vs. Pure Error

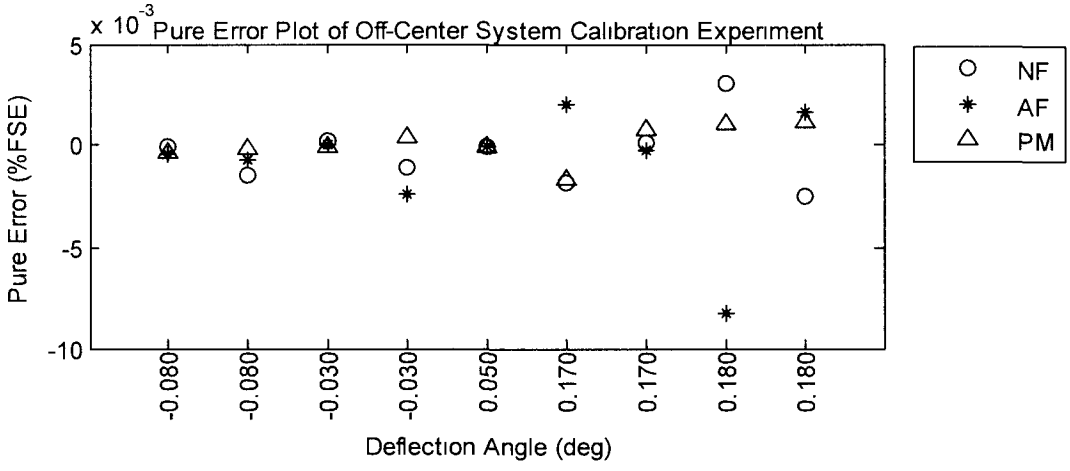

Figure 84. Off-Center System Deflection Angle vs. Pure Error

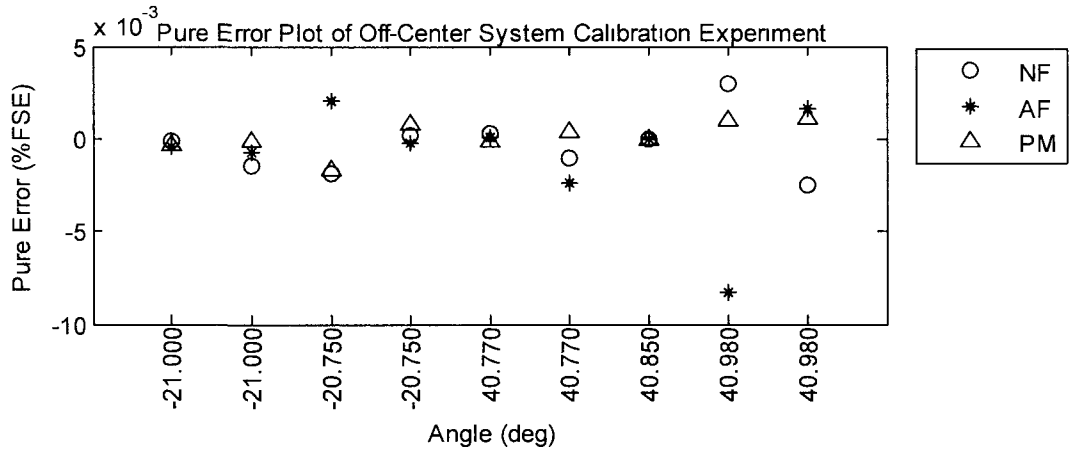

Figure 85. Off-Center System Total Angle vs. Pure Error

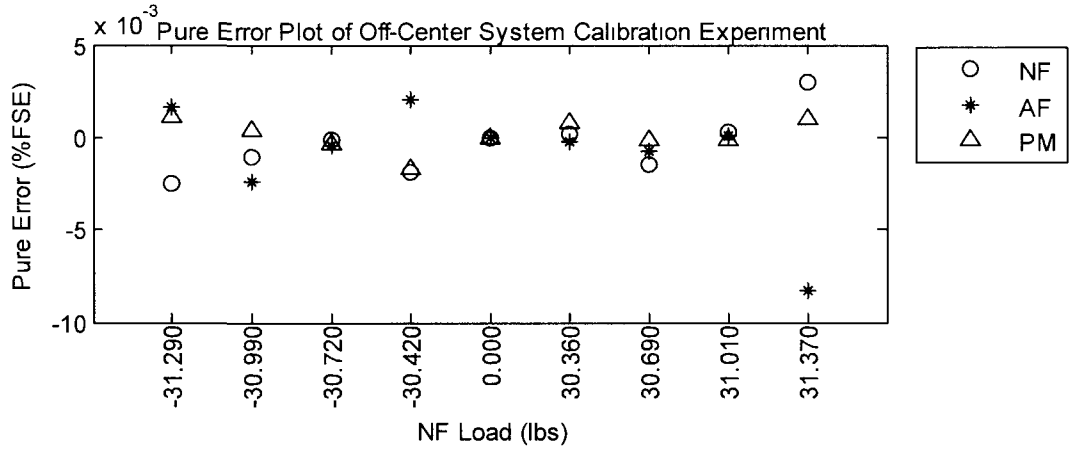

Figure 86. Off-Center System Normal Force vs. Applied Load Error

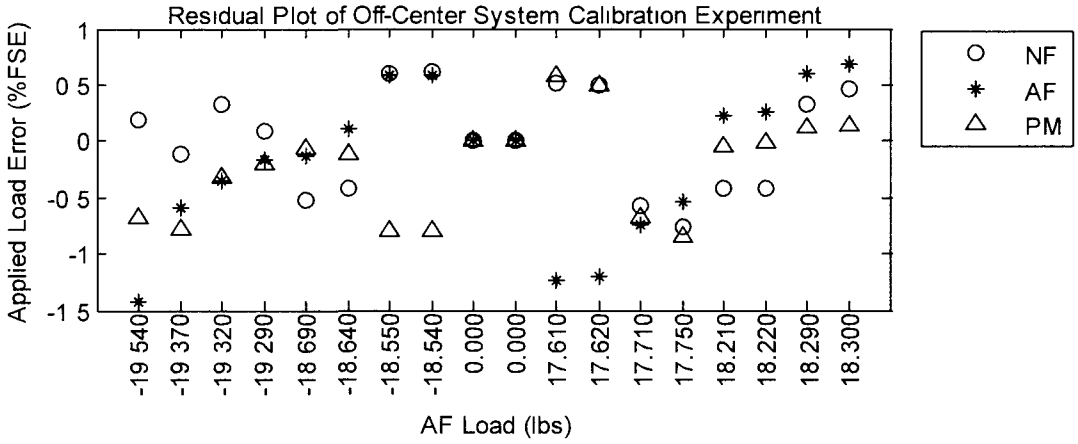

Figure 87. Off-Center System Axial Force vs. Applied Load Error

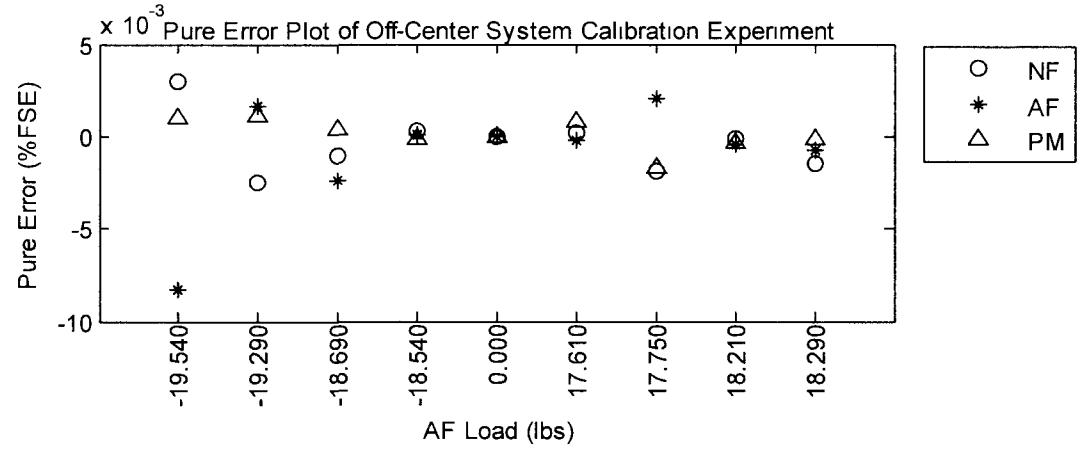

Figure 88. Off-Center System Axial Force vs. Pure Error

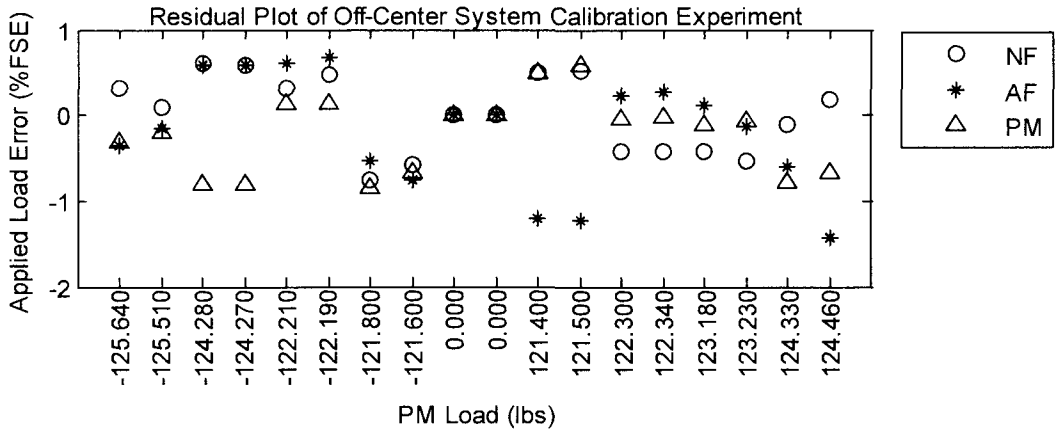

Figure 89. Off-Center System Pitching Moment vs. Applied Load Error

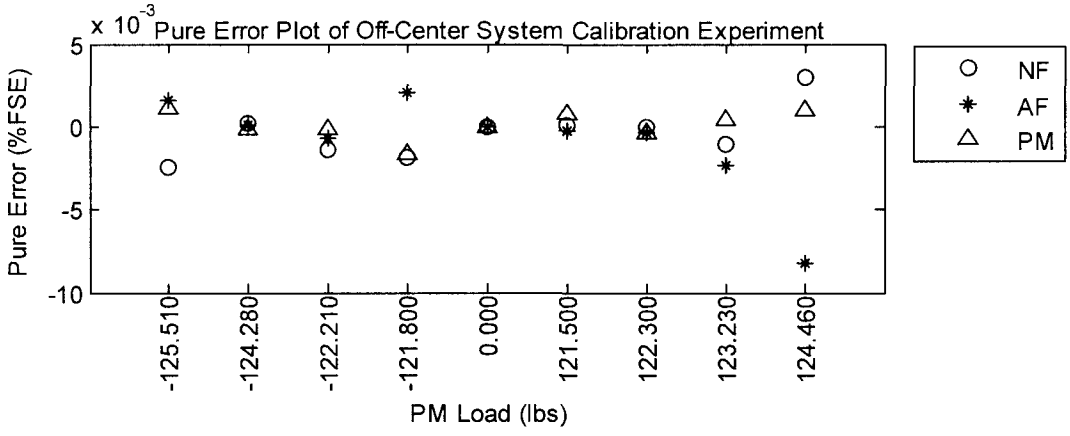

Figure 90. Off-Center System Pitching Moment vs. Pure Error

L. Augmentation of the Calibration Experiment

A higher order model that accommodates quadratic effects can be fit by augmenting the centered system calibration experiment with a second block of runs referred to as "axial" runs. The "axial" block is a set of runs that has one factor set at the maximum or minimum while the other two factors are set at the midpoint. Hence, plotted on a Cartesian system, the three dimensional representation of that run lies along the axes, which is why it is called an "axial run" [7]. An axial block, in combination with a factorial block forms a central composite design [7]. These types of designs are capable of efficiently accommodating the second order calibration model shown in equation (61).

$$R_i = a_i + \sum_{j=1}^{n} b1_{i,j} F_j + \sum_{j=1}^{n} c1_{i,j} F_j^2 + \sum_{j=1}^{n} \sum_{k=j+1}^{n} c3_{i,j,k} F_j F_k \qquad (61)$$

An axial block experiment was carried out using the centered system. The balance recorded loads are shown in table 47 in natural and coded units. The coded units are derived using the combined factorial plus axial experiment.

Table 47. Axial Block Loads for the Centered System

	Natural			Coded		
Std Run#	NF	AF	PM	NF	AF	PM
19	-49.39	10.99	6.72	-1.50	0.00	0.06
20	-49.38	10.99	6.77	-1.50	0.00	0.06
21	49.64	10.93	-5.81	1.50	-0.01	-0.05
22	49.61	10.92	-5.71	1.50	-0.02	-0.05
23	0.01	3.00	0.09	0.00	-1.60	0.00
24	0.02	3.00	0.27	0.00	-1.60	0.00
25	0.03	18.96	0.30	0.00	1.59	0.00
26	0.03	18.96	0.30	0.00	1.59	0.00
27	-0.03	11.05	-169.87	0.00	0.01	-1.48
28	-0.03	11.05	-169.72	0.00	0.01	-1.48
29	0.25	10.92	170.25	0.01	-0.02	1.48
30	0.24	10.92	170.23	0.01	-0.02	1.48
31	0.02	10.98	0.16	0.00	0.00	0.00
32	0.02	10.98	0.23	0.00	0.00	0.00

Similar to before, the prediction uncertainty, pure error and calibration uncertainty were calculated and combined into a total uncertainty for each run in the axial block experiment. The applied load error is plotted with the total uncertainty intervals for the axial block calibration experiment, as shown in figure 91. Contrary to the centered system factorial block, all runs within the axial block lie within the total uncertainty intervals, as shown in figure 91. This can be explained by the fact that only one force component is loaded per run, resulting in more controlled conditions than observed in the factorial block.

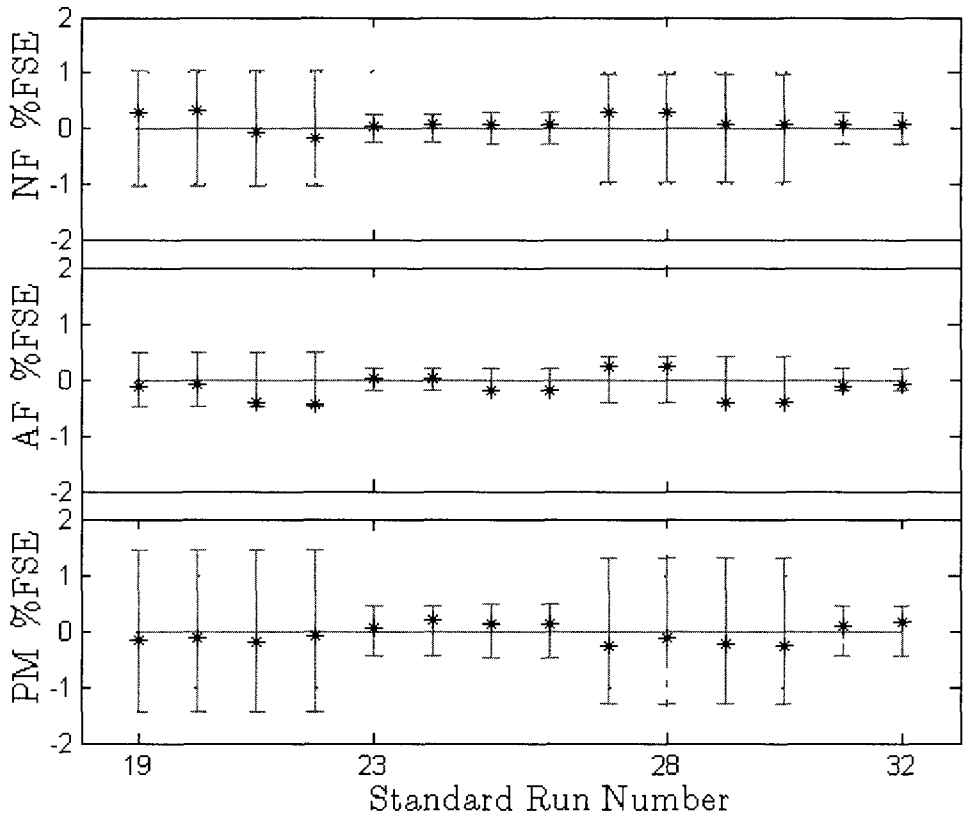

Figure 91. Center System Applied Load Error with Total Uncertainty Intervals (Axial Block)

An axial block experiment could not be demonstrated using the off-center system due to limited resources. More specifically, fabrication of two additional angle wedges was needed to properly orient the balance for the additional runs. Future systems, however, could use continuously variable wedges, as opposed to the monolithic parts used in this research.

VITA

Thomas H. Johnson
250 W. York St.
Norfolk VA, 23510
(203)246-1647

EDUCATION

B.S. Aerospace Engineering, Boston University, Boston MA, Summer 2006
M.S. Aerospace Engineering, Old Dominion University, Norfolk VA, Summer 2008
Ph.D. Aerospace Engineering, Old Dominion University, Norfolk VA, Summer 2011

WORK EXPERIENCE

TITLE	DESCRIPTION	DATE
NASA Co-op Research Intern	70% of work was devoted to Ph.D. research, while 30% involved various projects within NASA LaRC Aerospace Systems Engineering branch.	03/01/2010 – 08/10/11
NASA GSRP Research Engineer	This Graduate Student Research Program (GSRP) grant was renewed for a second year. 25 hrs/wk spent at NASA LaRC.	01/05/2008 - 03/01/2010
Wind Tunnel Research Assistant	Awarded $17k stipend for aerospace research at the Langley Full Scale Tunnel (LFST) on the Langley Air Force Base.	01/05/2007 - 01/05/2008

PUBLICATIONS

Johnson, T. H., Parker, P.A., Landman, D., "Calibration Modeling of Nonmonolithic Wind-Tunnel Force Balances," AIAA Journal of Aircraft, Vol. 47, No. 6, Nov-Dec 2010., pp. 1860-1866, DOI: 10.2514/1.46356, AIAA-46356-110.

"A Multi-Component Force Transducer Design From an Existing Rocket Payload Attachment Fitting," Johnson, T.; Landman, D. et al. AIAA Technical paper 2009-1716, Presented at the AIAA USAF T and E Days 2009, Albuquerque, NM, February 10-12, 2009.

"Calibration Designs for Non-Monolithic Force Transducers," Johnson, T.; Parker, P. et al. Conference Paper, The 7th International Symposium on Strain-Gauge Balances, sponsored by NASA Langley Research Center, 10–13 May 2010.

"Thermal and Pressure Characterization of a Wind Tunnel Force Balance using the Single Vector System," Lynn, C.; Johnson, T. et al. AIAA Technical paper, accepted for presentation at the 49th AIAA ASM Conf, Orlando FL, January 4-7, 2011.